Pulse Metrology Tool and Burst-Mode Laser Amplifier for the Free-Electron Laser in Hamburg

Dissertation
ZUR ERLANGUNG DES DOKTORGRADES

an der Fakultät für Mathematik, Informatik und Naturwissenschaften
FACHBEREICH PHYSIK
DER UNIVERSITÄT HAMBURG

vorgelegt von
HERRN DIPL.-PHYS. ROBERT RIEDEL

Hamburg, 2013

Erstgutachter:	Prof. Dr. Markus Drescher
Zweitgutachter:	Prof. Dr. Franz X. Kärtner
Tag der Dissertation:	02.12.2013
Gutachter der Disputation:	Prof. Dr. Dieter Horns
	Prof. Dr. Markus Drescher
	Prof. Dr. Franz X. Kärtner
	PD Dr. Tim Laarmann
	Prof. Dr. Peter Schmelcher

Abstract

The full scientific potential of high repetition rate free-electron lasers is still not exploited. The attainable resolution of time-resolved experiments is limited by fluctuating temporal pulse properties due to the self-amplified spontaneous emission process. To overcome this limitation, the temporal characterization of free-electron laser pulses was improved by the development of a single-shot temporal pulse metrology tool, based on a solid-state cross-correlation technique. The method is based on probing the optical transmission change of a transparent solid material pumped by a free-electron laser pulse. A comprehensive theoretical model allows the reconstruction of the free-electron laser pulse structure. Pulse duration measurements were performed at the Free-Electron Laser in Hamburg, FLASH, yielding 184 fs at 41.5 nm wavelength and sub-40 fs at 5.5 nm. Online measurements during a running experiment are possible with a residual soft-X-ray transmission of 10–45%. A resolution of sub-10 fs can be attained, provided that sufficiently short optical probe pulses are available.

Achieving the full performance of high repetition rate free-electron lasers, such as FLASH, requires also optical laser systems with a high repetition rate. A novel burst-mode optical parametric chirped-pulse amplifier is being developed for high-resolution pump-probe experiments and seeding of FLASH at its full repetition rate of 100 kHz–1 MHz. In this work, a first prototype was tested, delivering 1.4 mJ pulse energy and a spectral bandwidth supporting sub-7 fs pulse duration at 27.5 kHz intra-burst repetition rate. A passive pump-to-signal synchronization method was developed for long-term stability with sub-7 fs root mean square jitter between pump and signal pulses. The developed amplifier technology is scalable to high average powers for the future generation of kilowatt-pumped ultrashort laser amplifiers.

Kurzfassung in deutscher Sprache

Das Potential moderner Freie-Elektronenlaser im Röntgenbereich ist noch nicht voll ausgeschöpft, da starke Schwankungen der zeitlichen Pulseigenschaften die erreichbare Auflösung in zeitaufgelösten Experimenten limitieren. Um die Auflösung zu verbessern, wurde eine Einzelschuss-Röntgenpulsdiagnostik entwickelt, basierend auf dem Prinzip eines Plasmaschalters. Durch Abtasten der optischen Transmission einer mit dem Röntgenpuls angeregten Probe wurde eine Kreuzkorrelation zwischen einem optischen Laserpuls und dem Röntgenpuls gemessen. Ein theoretisches Modell zur Beschreibung der Ionisationsdynamik und der damit verbundenen optischen Transmissionseigenschaften wurde entwickelt und zur Rekonstruktion des Röntgenpulses verwendet. Pulsdauermessungen, welche am Freie-Elektronen-Laser in Hamburg, FLASH, durchgeführt wurden, ergaben eine Pulsdauer von 184 fs bei einer Wellenlänge von 41.5 nm sowie < 40 fs bei 5.5 nm. Da bei sehr dünnen Proben eine Resttransmission weicher Röntgenstrahlung von 10–45% zu erwarten ist, ist eine gleichzeitige Pulsdiagnostik während eines laufenden Experimentes möglich. Die theoretisch erreichbare Auflösung des Messverfahrens beträgt < 10 fs, wenn ein vergleichbar kurzer optischer Laserpuls zur Abtastung verwendet wird.

Freie-Elektronenlaser mit hohen Repetitionsraten profitieren in besonderem Maße von optischen Lasern mit hohen Repetitionsraten, da bei zeitaufgelösten Anregungs-Abfrage-Experimenten für jeden Röntgenpuls ein optischer Puls zur Verfügung stehen muss. Ein entsprechender Hochleistungslaser wird für FLASH entwickelt, basierend auf optisch-parametrischer Breitbandverstärkung. Dieser soll sowohl für die Femtosekundenspektroskopie in der Experimentierhalle, als auch für das Seeding bei Repetitionsraten von 100 kHz–1 MHz eingesetzt werden. In der vorliegenden Arbeit wurde ein erster Prototyp aufgebaut und getestet. Dieser lieferte 1.4 mJ Pulsenergie bei einer spektralen Bandbreite, welche Pulsdauern < 7 fs unterstützt. Die Repetitionsrate innerhalb eines Pulszuges betrug 27.5 kHz. Für die Verbesserung der Langzeitstabilität wurde ein passives Synchronisationskonzept für Pump- und Signalpulse entwickelt. Dabei wurde ein Synchronisationsjitter < 7 fs im quadratischen Mittel erreicht. Diese zukunftsweisende Verstärkertechnologie ist theoretisch auf hohe mittlere Ausgangsleistungen von mehreren einhundert Watt skalierbar.

Dedicated
to
my beautiful wife

List of publications: peer-reviewed journals

R. Riedel, M. Schulz, M. J. Prandolini, A. Hage, H. Höppner, T. Gottschall, J. Limpert, M. Drescher and F. Tavella. Long-term stabilization of high power optical parametric chirped-pulse amplifiers. *Optics Express* accepted (2013)

R. Riedel, A. Al-Shemmary, M. Gensch, T. Golz, M. Harmand, N. Medvedev, M. J. Prandolini, K. Sokolowski-Tinten, S. Toleikis, U. Wegner, B. Ziaja, N. Stojanovic and F. Tavella. Single-shot pulse duration monitor for extreme ultraviolet and X-ray free-electron lasers. *Nature Communications* **4**:1731 (2013)

A. Willner, A. Hage, **R. Riedel**, I. Grguras, A. Simoncig, M. Schulz, T. Dzelzainis, H. Höppner, S. Huber, M. J. Prandolini, B. Dromey, M. Zepf, A. L. Cavalieri, F. Tavella. Coherent spectral enhancement of carrier-envelope-phase stable continua with dual-gas high harmonic generation. *Optics Letters* **37**:3672–3674 (2012)

M. Schulz, **R. Riedel**, A. Willner, S. Düsterer, M. J. Prandolini, J. Feldhaus, B. Faatz, J. Rossbach, M. Drescher and F. Tavella. Pulsed operation of a high average power Yb:YAG thin-disk multipass amplifier. *Optics Express* **20**:5038–5043 (2012)

A. Willner, F. Tavella, M. Yeung, T. Dzelzainis, C. Kamperidis, M. Bakarezos, D. Adams, M. Schulz, **R. Riedel**, M. C. Hoffmann, W. Hu, J. Rossbach, M. Drescher, N. A. Papadogiannis, M. Tatarakis, B. Dromey and M. Zepf. Coherent Control of High Harmonic Generation via Dual-Gas Multijet Arrays. *Physical Review Letters* **107**:175002 (2011)

M. Schulz, **R. Riedel**, A. Willner, T. Mans, C. Schnitzler, P. Russbueldt, J. Dolkemeyer, E. Seise, T. Gottschall, S. Hädrich, S. Düsterer, H. Schlarb, J. Feldhaus, J. Limpert, B. Faatz, A. Tünnermann, J. Rossbach, M. Drescher and F. Tavella. Yb:YAG Innoslab amplifier: efficient high repetition rate subpicosecond pumping system for optical parametric chirped pulse amplification. *Optics Letters* **36**:2456–2458 (2011)

A. Willner, F. Tavella, M. Yeung, T. Dzelzainis, C. Kamperidis, M. Bakarezos, D. Adams, M. Schulz, **R. Riedel**, M. C. Hoffmann, W. Hu, J. Rossbach, M. Drescher, V. S. Yakovlev, N. A. Papadogiannis, M. Tatarakis, B. Dromey and M. Zepf. Efficient control of quantum paths via dual-gas high harmonic generation. *New Journal of Physics* **13**:113001 (2011)

List of publications: contributions to conference proceedings

S. Banerjee, M. Baudisch, J. Biegert, A. Borot, A. Borzsonyi, D. Charalambidis, T. Ditmire, Z. Diveki, P. Dombi, K. Ertel, M. Galimberti, J. Fulop, E. Gaul, C. L. Haefner, M. Hemmer, C. Hernandez-Gomez, M. Kalashnikov, D. Kandula, A. Kovacs, R. Lopez-Martens, P. D. Mason, I. Marton, I. Musgrave, K. Osvay, M. Prandolini, E. Racz, P. Racz, **R. Riedel**, I. Ross, J. Rosseau, M. Schulz, F. Tavella, A. Thai and I. Will. Conceptual Design of the Laser Systems for the Attosecond Light Pulse Source. *Conference on Lasers and Electro-Optics (CLEO)* **CTu2D**.6 (June 9–14 2013, San José, California USA)

F. Tavella, **R. Riedel**, A. Willner, M. Schulz, M. J. Prandolini, S. Düsterer, J. Feldhaus, M. Drescher and B. Faatz. Optical Parametric Chirped Pulse Amplification at High Repetition Rate Free Electron Laser Facility. *Frontiers in Optics (FiO) conference 2012* **FTu5B**.2 invited (October 14–18 2012, Rochester, New York USA)

M. Schulz, A. Willner, **R. Riedel**, M. J. Prandolini, S. Düsterer, J. Feldhaus, B. Faatz, M. Drescher and F. Tavella. Kilowatt level burst-mode OPCPA pump amplifier concepts. *Frontiers in Optics (FiO) conference 2012* **FM4G**.1 invited (October 14–18 2012, Rochester, New York USA)

M. Schulz, A. Willner, **R. Riedel**, M. J. Prandolini, S. Duesterer, J. Feldhaus, B. Faatz, J. Rossbach, M. Drescher and F. Tavella. Kilowatt level Yb:YAG thindisk pump laser amplifier system for seeding FLASH2. *Conference on Lasers and Electro-Optics (CLEO)* **CM1D**.1 (May 6–11 2012, San José, California USA)

K. Honkavaara *et al.* Status of the FLASH II Project. *Proceedings of the Free-Electron Laser Conference (FEL)* **WEPD**.07 (August 22–26 2011, Shanghai, China)

A. Willner, M. Schulz, **R. Riedel**, M. Yeung, T. Dzelzainis, C. Kamperidis, M. Bakarezos, D. Adams, V. Yakovlev, J. Rönsch-Schulenburg, B. Dromey, N. Papadogiannis, M. Tatarakis, S. Düsterer, S. Schreiber, B. Faatz, M. Drescher, J. Rossbach, M. Zepf and F. Tavella. A new XUV-source for seeding a FEL at high repetition rates. *SPIE Proceedings* **8075**:80750L (April 18 2011, Prague, Czech Republic)

M. Först, M. Gensch, **R. Riedel**, F. Tavella, E. A. Schneidmiller, N. Stojanovic, M. V. Yurkov. Optical Afterburner for SASE FEL: First Results from FLASH. *Proceedings of the International Particle Accelerator Conference (IPAC)* **THPC**.084 (September 4–9 2011, San Sebastián, Spain)

F. Tavella *et al.* High Repetition Rate mJ-level Few- Cycle Pulse Laser Amplifier for XUV-FEL seeding. *High Intensity Lasers and High Field Phenomena (HILAS) conference* **HThD**.1 (February 16–18 2011, Istanbul, Turkey)

List of Figures

List of Tables

Contents

Chapter 1

Introduction

The full potential of fourth-generation extreme-ultraviolet (XUV) and X-ray free-electron lasers (FELs) is still not accessible. Time-resolved experiments in this wavelength region show the most promising applications, enabling outstanding insight into ultrafast processes on the nanoscale with a huge impact on a broad scientific community. The Free-Electron Laser in Hamburg, *FLASH*, is to date the only light source generating intense ultrashort pulses in the XUV and soft X-ray spectral region at a high repetition rate [1]. This unique property benefits the qualitative and quantitative scientific output from a single experimental beam time. However, such excellent performance is still not accessible for the great majority of time-resolved experiments. This is, on one hand, due to the lack of FEL pulse metrology tools, and, on the other hand, due to the limited performance of the applied optical laser systems.

This doctoral thesis treats the development of novel techniques, improving the performance of time-resolved experiments at state-of-the-art and future XUV and X-ray free-electron lasers. Foremost, a precise and versatile metrology tool for the temporal properties of single FEL pulses was developed at FLASH [2]. Furthermore, a new high repetition rate optical parametric chirped-pulse amplifier (OPCPA) is being developed [3] for the application as pump-probe laser and seeding laser. This will allow increased experimental statistics and improved temporal resolution at pump-probe experiments performed at FLASH. In addition, the temporal and spectral pulse stability as well as the synchronization can be improved by future seeding of the FEL at a high repetition rate. The achieved laser parameters are worldwide unique and will consolidate the position of FLASH at the forefront of FEL science. The aim of this work is to contribute to an enhanced performance of future experiments that involve the powerful combination of ultrashort XUV and X-ray FELs and optical lasers.

1.1 Problems and challenges

Today, FELs are operated as user facilities, relying on large-scale linear electron accelerators (LINACs) and state-of-the-art precision undulator technology [1, 4–7]. Pulse durations in the 10 fs range at gigawatts of optical power are achieved with a high degree of spatial and temporal coherence compared to conventional synchrotron sources. However, despite the unique scientific capabilities of FELs, the main handicap is insufficient characterization of the statistically fluctuating temporal pulse properties, limiting the resolution of time-resolved experiments at FELs.

One of the scientific goals of XUV and X-ray free-electron laser science is the time-resolved investigation of structural dynamics of matter with atomic resolution [8]. Foremost, *instantaneous* coherent diffractive imaging of a single biomolecule in its functional environment is traded as *the* outstanding FEL application [9–12]. The investigation of inner-shell photoexcitation [13–16] and nonlinear processes in atoms, molecules and clusters [17–19] on ultrafast time scales reveals groundbreaking understanding of the microscopic world. Collective charge transfer [20, 21] and spin dynamics in condensed matter has been spotlighted to push the frontiers of solid-state physics and information technology [22, 23]. In addition, the generation of tailored high-density states of matter and their temporal evolution has become accessible [24–27] to study astronomic phenomena in the laboratory and to improve laser-induced inertial fusion [28]. Major improvements are expected by solving the following problems and challenges at current FELs addressed in this thesis:

- **FEL arrival time jitter:** A versatile temporal diagnostic method for FEL pulses was developed. Despite possible FEL and optical laser pulse durations in the 10 fs regime, the temporal resolution is limited by the statistical deviations of the arrival time delay, Δt, between the optical laser and the FEL, which is on the order of 100 fs root mean square (rms) [29–31]. This jitter is introduced by the electronic locking between optical laser and FEL, by the self-amplified spontaneous emission (SASE) process, by drifts in the accelerator modules, and by environmental influence on the whole facility, such as temperature, humidity and vibration. Optical synchronization [32] and external seeding [33] are possible solutions to reduce the jitter to sub-30 fs rms. But still, in order to approach the possible resolution limit, the arrival time delay needs to be measured on a single-shot basis. The developed pulse metrology tool developed in this work is capable to achieve sub-10 fs resolution [2].

- **FEL pulse duration:** The temporal pulse properties of SASE FELs underlie strong fluctuations. Precise knowledge of the FEL electric field is required, especially for the investigation of nonlinear processes in the XUV [34] or X-ray regime [35]. The available pulse metrology techniques are complex and time consuming. Therefore, the temporal diagnostic method was extended to pulse duration measurements, relying on a single-shot cross-correlation. The method can be operated simultaneously to an experiment [2].

- **FEL seeding:** Present SASE FELs suffer from fluctuations of many pulse parameters, such as beam profile, pulse energy, pulse duration, spectrum, coherence and arrival time. Fully coherent FEL pulses with stable pulse parameters can be achieved via direct seeding of the FEL process by a defined external laser pulse [7, 36–39]. For the new FEL FLASH2, the seeding with high gain harmonic generation (HGHG [7]) is planned at the full intra-burst repetition rate of 100 kHz to 1 MHz. Therefore, a high repetition rate seeding laser is being developed (see next point). Even though the FEL seeding itself is not treated in this thesis, the developed temporal diagnostic method is an essential technology for the characterization and optimization of the seeding process.

- **High repetition rate laser development:** A high repetition rate burst mode OPCPA is being developed for the application as seeding laser and as pump-probe laser. FLASH is operated in a 10 Hz burst mode with an intra-burst repetition rate of up to 1 MHz, corresponding to 8000 pulses per second. Many experiments suffer from a very low light-matter interaction cross-section. The high repetition rate is beneficial for reducing the integration time, yielding an increased data rate, and hence, an increased scientific output from a single beam time. Therefore, the burst operation mode should be also provided by the seeding laser and the optical pump-probe laser. The current burst mode laser at FLASH delivers only 4000 pulses per second with pulse energies of 10 µJ, which is not sufficient for seeding. The alternative 10 Hz system delivers single pulses with 10 mJ. The bottleneck is the laser amplifier technology. The planned OPCPA aims for intra-burst repetition rates from 100 kHz to 1 MHz for seeding and pump-probe experiments. The developed system is capable to generate shortest optical pulses down to the sub-10 fs regime with about 1 mJ pulse energy. This enables high temporal resolution in pump-probe experiments and sufficient energy for FEL seeding.

1.2 Jitter limitations at FELs

The common method for time-resolved experiments is the *pump-probe* technique. At least two ultrashort pulses are used, a *pump*-pulse and a *probe*-pulse. The pump-pulse triggers an event, for instance an excitation to a non-equilibrium state. The probe pulse is used to investigate the excited state after a certain time delay, Δt, with respect to the pump pulse. The parameter to be probed, $f(t)$, must reflect the state of the investigated system, often described by a dedicated theoretical framework. The parameter $f(t)$ may describe, for example, the optical transmission change due to electronic population dynamics after an optical excitation. By repeating the measurement for different delays, a stroboscopic recording of the system's evolution from the non-equilibrium state to a new equilibrium state can be performed. Because the detection system is slow compared to the duration of the pulses, the measured signal is the convolution,

$$S(\Delta t) = \int_{-\infty}^{+\infty} f(t) G(t - \Delta t) \mathrm{d}t, \tag{1.1}$$

with a gating function, $G(t)$, that is directly related to the probe laser intensity (via the corresponding light-target interaction). If the probe pulse is short compared to the ultrafast process, it can be regarded as a DIRAC δ function and the measured signal is directly proportional to the parameter to be measured, $S(\Delta t) \propto f(\Delta t)$. If the process is comparable to the gating pulse duration, the parameter $f(t)$ is obtained via a deconvolution. As a signal deconvolution is not always possible without considerable errors, the shortest possible probe pulse duration is desired for the highest possible temporal resolution.

Temporal pulse metrology of ultrashort pulses in the XUV and X-ray regime is challenging. Various techniques for direct [40–46] and indirect [47–51] measurements exist. For autocorrelation and cross-correlation methods [42–44, 52] certain limitations exist concerning the photon energies and the range of measurable pulse durations. The main disadvantage is that these methods average over many pulses and are thus no single-pulse diagnostics. Light-field streaking measurements [40, 41, 45, 53] yield information about the single-shot pulse duration, the linear frequency chirp and the FEL arrival time, but require either a dedicated terahertz undulator in the FEL beamline [54, 55] or a laser-driven terahertz source [56, 57].

In particular at pump-probe experiments comprising an optical pump and an FEL probe pulse, or *vice versa*, the temporal resolution is not only determined by the pulse durations. It is also limited by the jitter of the delay, Δt, due to the fluctuations arising from the SASE process and various influences in the accelerator environment. Even with direct seeding or optical synchronization methods, a residual jitter is expected. A solution is to measure Δt directly at the experimental station and simultaneously to the experiment.

A straightforward way to measure Δt is implementing a single-shot cross-correlation method that uses the ultrafast optical transmission change of a solid-state target pumped by an FEL pulse. This technique was first tested at FLASH [31, 45, 58–65] for online arrival time measurements directly behind the experiment. The optical probe laser was partially absorbed if both pulses temporally overlapped, similar to a cross-correlation. The delay was determined by measuring the reflected optical laser intensity with a spatially encoded non-collinear setup. In Fig. 1.1a (from [31]), the dark shading represents the reduced reflectivity measured for different delays, Δt, between FEL and optical probe laser. The position of the boundary of reflectivity change on the spatially encoded time axis, $t \mapsto x$, represents the delay (see Chapter 3 for details). Tagging the determined delay to a simultaneously acquired experimental data point allows for appropriate re-sorting of the measured data points. The challenge for the present work was to extend this method to extract the FEL pulse duration and to develop a semi-transparent solution for online measurements directly in front of the experiment.

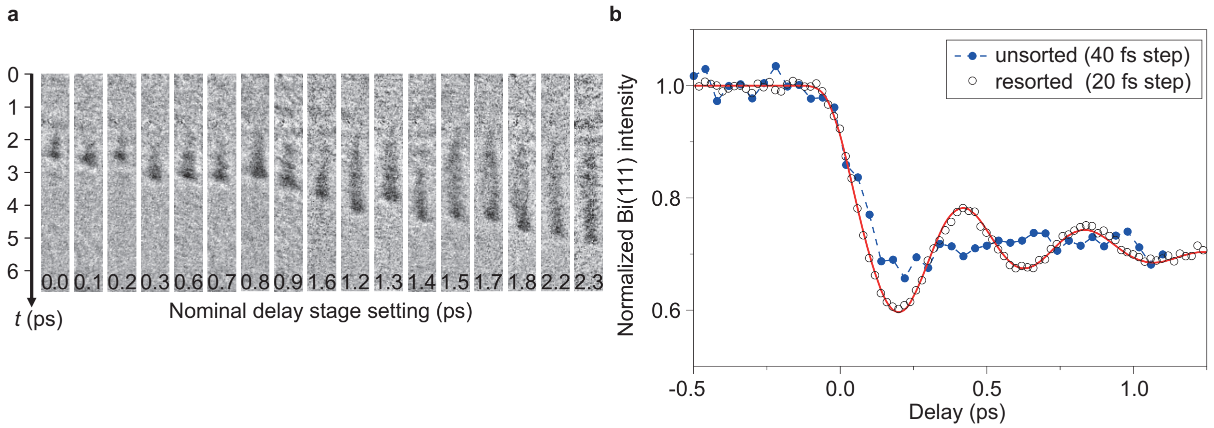

Figure 1.1 Delay jitter in pump-probe experiments with optical lasers and FEL pulses. (**a**) FEL arrival time delay measurement using a solid-state XUV/optical cross-correlation method at FLASH (Figure from [31]). In this series of measurements, the dark shading represents the optical reflection change of a GaAs target pumped by the FEL. Owing to the spatially encoded non-collinear setup, the time axis is mapped to the spatial axis, $t \mapsto x$. The position of the onset of the shading depends on the delay (solid line) between optical pulse and FEL pulse. (**b**) Enhanced resolution during a pump-probe experiment using an optical pump and an X-ray probe. The optical pulse pumps a phonon in a bismuth (Bi) crystal. The X-ray pulse probes the lattice distance at the time Δt after the excitation by measuring the BRAGG-diffracted intensity. Simultaneously, the arrival time was measured using an X-ray/optical cross-correlation method similar to (a). The resolution of the blue curve is limited by the jitter, whereas the white dots resolve the phonon oscillations by sorting the data according to the measured delay (red curve: theory). Figure from [65].

An improvement of temporal resolution was recently demonstrated at the Linac Coherent Light Source X-ray FEL (LCLS, Stanford, USA) using a similar delay tagging method [65]. An optical pump pulse with the central wavelength $\lambda_L = 800\,\mathrm{nm}$ excited an optical phonon in a solid bismuth target [66, 67]. The X-ray FEL pulse at 7.1 keV photon energy probed the excited crystal volume by BRAGG-diffraction after a time delay, Δt. Due to the optical excitation the Bi atoms were displaced from their initial equilibrium position, d_1, and performed a damped oscillation around a new perturbed equilibrium position, d_2. The X-ray diffraction intensity is a probe of the inter-atomic distance of Bi(111) lattice planes. Simultaneous to the experiment, the temporal delay between optical pump and X-ray probe laser was measured by a cross-correlation on a solid-state target, as explained before. The measurement is shown in Fig. 1.1b. The first measurement was performed without simultaneous delay measurement (blue dotted curve). Although the transition between the equilibrium positions was traced, the oscillations were not resolved, because the temporal resolution was limited by the large delay jitter. In comparison, the white-dotted curve was achieved by simultaneously measuring the X-ray/optical cross-correlation and sorting the data points according to their respective delay. The temporal resolution could be increased to the sub-10 fs range [65], demonstrating the potential of this cross-correlation method. However, in the X-ray regime, the implementation benefits from the low target absorption. In comparison, such a simultaneous cross-correlation measurement suffers from the strong target absorption in the XUV regime. In the present work, the feasibility for such simultaneous measurements was demonstrated at FLASH using ultra-thin silicon nitride membranes pumped at an FEL wavelength of 5.5 nm.

1.3 Present and future scenario for FLASH

In the present scenario, most XUV and X-ray FELs are operated in SASE mode. A typical SASE FEL layout is shown in Fig. 1.2a. Because the FEL pulses are amplified from a statistical shot noise in the undulator section, the pulse properties vary from shot to shot. This affects not only the pulse energy and spatial beam properties, but in particular also the spectral and temporal properties of the pulse. In addition, due to the amplification of multiple longitudinal modes, the resulting pulse structure of SASE FELs can be very complicated [41]. As a consequence, the intensity envelope may consist of multiple sub-pulses that fluctuate from shot to shot. In Fig. 1.2c, a theoretical simulation of the temporal profile is shown (from [1]) to demonstrate the shot-to-shot fluctuations in SASE mode. Here, three different single-shot profiles were obtained (thin lines), each featuring three longitudinal modes. The mean pulse duration (solid line) is 10 fs and yields $P = 3\,\text{GW}$ of optical power. The most intense single pulse has a pulse duration of less than 5 fs and a power exceeding 10 GW.

Due to the shot-to-shot fluctuations of SASE FELs, a single-shot temporal diagnostic method at the experimental station is indispensable. In Fig. 1.2b, a possible scenario is described on how a high repetition rate XUV FEL, such as FLASH, may look in the future. The general schematic is similar to the SASE FEL (Fig. 1.2a). At the experimental station, before or behind the experiment, the single-shot cross-correlator developed in this work may be implemented as an online diagnostic tool. The arrival time and the pulse duration of each FEL pulse in the burst can be measured with a fraction of the burst-mode optical parametric chirped-pulse amplifier (OPCPA), which is also part of this work, and tagged to the corresponding experimental data point. The burst-mode OPCPA pump-probe laser in the experimental hall provides the experiment with mJ-level optical pulses with pulse durations down to sub-10 fs. The combination of cross-correlator and OPCPA allows for time-resolved studies with unprecedented resolution. The temporal synchronization of the laser systems can be realized electronically using optical fiber links locked to a master laser oscillator [32]. This type of synchronization is currently being installed at FLASH. In this future scenario, the FEL is externally seeded via HGHG [7, 68] at high burst repetition rate with intense ultraviolet (UV) pulses from the seeding OPCPA. This allows the generation of fully coherent XUV pulses, improving the temporal and spectral stability for FEL experiments. Furthermore, the direct synchronization to the pump-probe OPCPA may be possible using a fraction of the seeding laser. The HGHG seeding scheme has been successfully implemented for user operation at the low repetition rate XUV FEL FERMI@Elettra

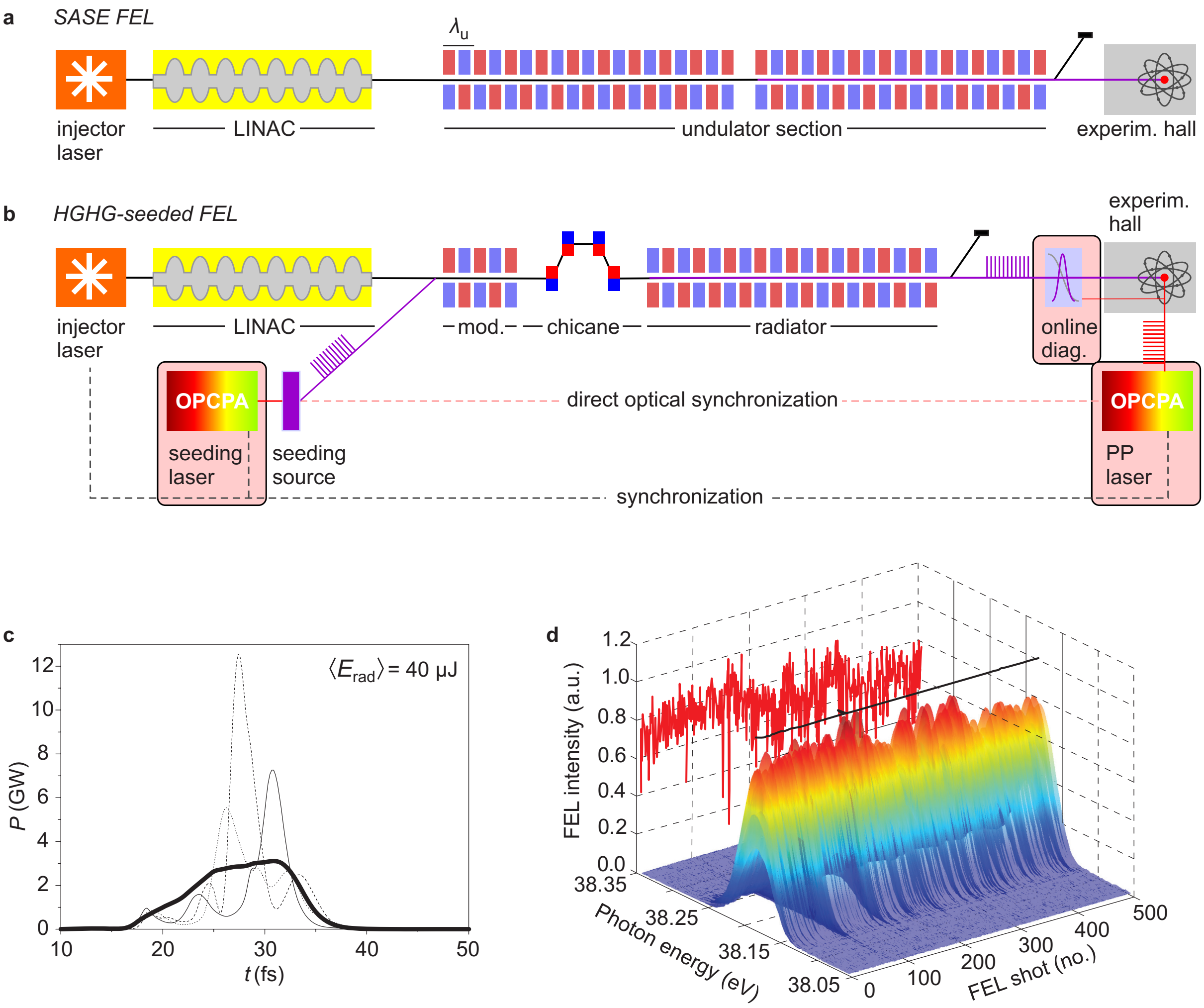

Figure 1.2 Present and future status of extreme-ultraviolet (XUV) free-electron lasers (FELs). (**a**) Present status: schematic of a self-amplified spontaneous emission (SASE) FEL. Injector laser: generation of ultrashort electron bunches on a photocathode. LINAC: linear electron accelerator. Undulator section: alternating magnetic field with period λ_u for emission of radiation. Experimental hall: Beam transportation, beam diagnostics, pump-probe laser, experimental setups. (**b**) Future scenario: high gain harmonic generation (HGHG) seeding of the FEL [7, 68] at the full repetition rate, using a burst-mode optical parametric chirped-pulse amplifier (OPCPA) as seeding laser (highlighted). The generated ultraviolet (UV) pulses (seeding source) are coupled into the modulator for HGHG seeding. The temporal pulse properties are monitored with an online XUV/optical cross-correlator (online diag., highlighted). In the experimental hall, a burst-mode OPCPA provides sub-10 fs pump-probe pulses with mJ pulse energies. The pump-probe laser (highlighted) could be directly synchronized with a fraction of the seeding laser. Commonly, the synchronization is achieved by electronic locking of all lasers. (**c**) Theoretical simulation of single-shot SASE pulses (thin lines). The temporal evolution of the optical power, P, is plotted. The averaged profile (thick line) features a pulse duration of 10 fs. From [1]. (**d**) Series of single-shot spectra measured at the HGHG-seeded FEL FERMI@Elettra. From [7].

in Trieste, Italy [7]. The measurement in Fig. 1.2d shows 500 stable single-shot spectra of the seeded FERMI FEL lasing at the 7^{th} harmonic at 38.2 nm [7]. Due to the lack of adequate single-shot temporal diagnostic methods at current free-electron lasers, the temporal shape of the seeded pulses is still not measurable.

In summary, the improvements will enable pump-probe experiments with increased temporal resolution and high pulse repetition rate at FLASH and future FELs. With the seeding and the temporal diagnostics, intense XUV and X-ray pulses with full control over the temporal pulse properties will be possible.

1.4 Thesis outline

The contribution of this thesis to the outlined problems and possible improvements in FEL science comprises the development of an XUV and X-ray single-shot temporal diagnostic method and a prototype of a high-power laser amplifier for future application as seeding laser and pump-probe laser at FLASH. The thesis is subdivided in three main chapters, addressing these points separately:

- **Chapter 2: Theoretical Background.** A brief overview about the principle of free-electron lasers and different seeding schemes is given. The theoretical background for ultrashort pulse propagation and nonlinear phenomena is treated. In particular, the broadband optical parametric amplification with non-collinear phase-matching is discussed as the method of choice for the development of the high-power laser amplifiers. In order to provide the theoretical fundamentals for the FEL pulse duration measurement technique, the ionization dynamics in solids irradiated with XUV and X-ray pulses are explained in detail. An overview about optical pulse duration measurement techniques, such as cross-correlation and autocorrelation, is given at the end of the chapter.

- **Chapter 3: Single-shot pulse duration measurements at XUV and X-ray free-electron lasers.** In the main chapter, an overview about existing pulse duration measurement methods is given. Subsequently, the key results of this work are presented: a method for FEL pulse duration measurement was further developed, based on a single-shot cross-correlation between the FEL and the optical laser pulse on a solid-state target [2, 31, 45, 60–65]. With this method, the FEL pulse duration and the arrival time can be determined within a single shot. Furthermore, the possible application as an online tool is shown. Afterwards, a theoretical evaluation of the resolution limit is performed, including the influence of the signal-to-noise ratio. For increasing the temporal resolution of the cross-correlation method, a dedicated ultrashort laser amplifier is presented.

- **Chapter 4: Development of a high repetition rate laser amplifier.** For the applications as high-repetition rate pump-probe laser and seeding laser at FLASH, the development of a burst-mode, mJ-class, broadband optical parametric chirped-pulse amplifier (OPCPA) is required. In this chapter, the demands on the laser systems are defined in detail and the concepts of chirped-pulse amplification and OPCPA are reviewed. Experimental results on a first burst-mode OPCPA prototype system are presented. To ensure reliable long-term stability of such high-power OPCPAs, a novel passive pump-to-signal synchronization technique for OPCPA was developed. The method relies on white-light supercontinuum generation. In the end of the chapter, the scaling prospects for kilowatt-pumped high-power OPCPAs are theoretically investigated.

Chapter 2

Theoretical background

2.1 Principle of free-electron lasers

Extreme ultraviolet (XUV) and X-ray free-electron lasers (FELs) are operated as single-pass, high-gain FELs, mostly in self-amplified spontaneous emission (SASE) mode [69, 70]. The basic principle of a SASE FEL, such as FLASH, is illustrated in Fig. 1.2a on p. 8. Initially, an ultrashort pulse of electrons, hereafter referred to as an electron bunch, is generated by focusing an ultrashort laser pulse on a photocathode[1] (injector laser) [71]. This electron bunch is injected to a microwave-driven LINAC and accelerated to relativistic kinetic energies in the GeV regime. In order to keep the bunch short, temporal compression is introduced by magnetic chicanes. The radiation emission is achieved in the undulator, a periodic structure of transverse magnetic fields with alternating poles. The emission wavelength is given by the resonance condition [69, 70],

$$\lambda_{\mathrm{FEL}} = \frac{\lambda_{\mathrm{u}}}{2\gamma^2}\left(1+\frac{K^2}{2}+\gamma^2\Theta^2\right), \tag{2.1}$$

where λ_{u} is the undulator period, $\gamma = (E_{\mathrm{kin}} + m_{\mathrm{e}}c^2)/(m_{\mathrm{e}}c^2)$ represents the kinetic energy of the relativistic electron, c is the vacuum speed of light, m_{e} is the rest mass of the electron and Θ is the divergence angle in the laboratory frame. Characteristic parameters are the undulator period, λ_{u}, and the undulator parameter,

$$K = \frac{eB_0\lambda_{\mathrm{u}}}{2\pi m_{\mathrm{e}}c}, \tag{2.2}$$

where e is the elementary charge and B_0 is the maximum magnetic field strength. In this initial phase of SASE, the spontaneously emitted electric field (shot noise) couples to the electron bunch, which leads to a periodic longitudinal density modulation with a period of λ_{FEL}, called *micro-bunching*[2] [69, 70]. Electron micro-bunches separated by λ_{FEL} radiate in phase. This modulation effect increases quadratically over the propagation distance. The larger fraction of the electron bunch coherently emits a short pulse [69, 70]. As the shot noise is emitted spontaneously, the final pulse properties vary from shot to shot. This affects not only the pulse energy and spatial beam properties, but in particular also the spectral and temporal properties of

---

[1] At FLASH, a highly efficient Cs_2Te photocathode is placed at the back plane of a radio-frequency acceleration cavity

[2] More precisely, micro-bunching is a result of energy dispersion in the undulator. The electric field imprints an energy modulation on the bunch, depending on the relative phase between electrons and electric field. Owing to energy dispersion in the undulator, this energy modulation is converted into a density modulation.

the pulse. In general, a multitude of micro-bunched regions is generated, depending on the ratio between λ_{FEL} and the electron bunch length. This leads to the radiation of multiple longitudinal modes, spatially and spectrally separated, with no defined phase relation between them. Due to this limited longitudinal coherence, the resulting pulse structure of SASE FELs can be very complicated. The intensity envelope may consist of multiple sub-pulses that fluctuate from shot to shot.

Seeding of the FEL enables the generation of controllable, temporally coherent pulses with enhanced pulse-to-pulse stability. The modulation of the electron bunch is achieved by an external laser pulse in the undulator, rather than by the stochastic shot noise. This can be realized using several schemes. In the *direct seeding* scheme, the FEL is seeded directly at its emission wavelength, $\lambda_{\mathrm{seed}} = \lambda_{\mathrm{FEL}}$ [72, 73]. The same undulator section as in SASE operation can be used. The FEL can be viewed as an amplifier for the seeding pulse, which is generated by higher-harmonic generation (HHG) using ultrashort laser pulses. The attainable FEL wavelength range is limited by the available seed laser sources and seed power in the required wavelength regime. At FLASH, an efficient HHG dual gas target was developed to achieve intense XUV pulses in the $\lambda_{\mathrm{seed}} = 60\ldots10\,\mathrm{nm}$ wavelength range [74–76].

In the *high-gain harmonic generation* (HGHG) scheme, the FEL is seeded at higher wavelengths in the ultraviolet (UV), where more optical power can be obtained [7, 68]. The seed wavelength is a sub-harmonic of the FEL wavelength, $\lambda_{\mathrm{seed}} = q \cdot \lambda_{\mathrm{FEL}}$. The undulator section is different compared to the SASE undulators (compare Fig. 1.2a). For HGHG seeding at XUV FELs, UV laser pulses are first coupled in a modulator (a short undulator) for energy modulation of the electron bunch. The modulated electron bunch is sent through a magnetic dispersive chicane. The energy modulation is projected into a density modulation with the period λ_{seed}. Finally, the density-modulated bunch passes the radiator (a long undulator), which is tuned to the higher harmonic of the seeding wavelength, $\lambda_{\mathrm{FEL}} = \lambda_{\mathrm{seed}}/q$, where $q \approx 4\ldots15$ is the harmonic number. This scheme can be cascaded for reaching even shorter wavelengths down to the soft-X-ray region. An alternative approach, to circumvent multiple HGHG cascades, is the *echo-enabled harmonic generation* (EEHG) scheme [77]. The EEHG scheme requires an additional modulator, a second seed laser pulse and a second dispersive chicane, after the first modulator and the first chicane, and before the radiator. After the second modulator and chicane, a very efficient density modulation at the higher harmonic can be achieved, $\lambda_{\mathrm{FEL}} = \lambda_{\mathrm{seed}}/q$.

In a passive seeding approach, the FEL is seeded by SASE radiation. After SASE in a first undulator section, the electron bunch passes a magnetic chicane, whilst the SASE pulse is spectrally filtered in a single-crystal diamond monochromator. The filtered pulse seeds the bunch in a second undulator section. This seeding scheme, referred to as *self-seeding*, is favorable for X-ray FELs, where no external seeding sources are available. Self-seeding increases the longitudinal coherence and reduces the spectral bandwidth, leading to improved spectral brightness and spectral stability. The implementation of self-seeding for XUV FELs is more difficult, because the long beam path in the complex grating monochromator needs to be compensated by a large magnetic chicane.

2.2 Propagation of ultrashort pulses

In classical electrodynamics, the propagation of light is described by the coupling of electric and magnetic fields, E and H, respectively. James Clerk MAXWELL formulated the according system of differential equations, the MAXWELL-equations [78]. In this system, the light-matter interaction is treated purely phenomenologically in terms of polarization and magnetization of the medium, P and M, respectively, and under the presence of external charges and currents. In this context, ultrashort light pulses are described as electric field wave packets that represent solutions to a proper wave equation, obtained from the coupled system of MAXWELLs equations [79]. In the case of non-magnetic isotropic media (and under absence of external charges and currents) with a linearly polarized electric field propagating as plane wave along the propagation axis, z, the one-dimensional scalar wave equation is obtained:

$$\left(\frac{\partial^2}{\partial z^2} - \frac{1}{c^2}\frac{\partial^2}{\partial t^2}\right) E(z,t) = \mu_0 \frac{\partial^2}{\partial t^2} P(z,t), \tag{2.3}$$

where $c = 2.99 \cdot 10^8\,\mathrm{ms}^{-1}$ is the vacuum speed of light, and $\mu_0 = 4\pi \cdot 10^{-7}\,\mathrm{VsA}^{-1}\mathrm{m}^{-1}$ is the vacuum permeability. On the right-hand side, the polarization, $P(z,t)$ acts as a source term for radiation and describes the response of the medium under presence of an electric field. In general, this response has a finite duration, which has consequences on the absorption and dispersion properties of the medium. In the frequency domain, the polarization is expressed as

$$P(\omega,z) = \varepsilon_0 \left[\chi^{(1)}(\omega) \cdot E(\omega,z) + P^{\mathrm{NL}}(\chi^{(n)}(\omega) E^n(\omega,z))\right] \tag{2.4}$$

where $\varepsilon_0 = 8.854 \cdot 10^{-12}\,\mathrm{Fm}^{-1}$ is the vacuum permittivity, and $\chi^{(1)}(\omega)$ is the linear susceptibility, which is the linear response of the medium. The nonlinear response is summarized in the nonlinear polarization term $P^{\mathrm{NL}}(\chi^{(n)}(\omega)E^n(\omega,z))$. While the nonlinear polarization is treated in Section 2.4.1, it is neglected here to point out the effect of linear optical elements on the propagation of ultrashort light pulses. The linear part of the polarization is

$$P^{\mathrm{L}}(\omega,z) = \varepsilon_0 \left[\varepsilon(\omega) - 1\right] E(\omega,z), \tag{2.5}$$

with the frequency-dependent relative permittivity of the medium,

$$\varepsilon(\omega) = \left[1 + \chi^{(1)}(\omega)\right]. \tag{2.6}$$

The linear propagation of ultrashort pulses is commonly described in the frequency domain. Hence, the corresponding wave equation is obtained by Fourier-transformation of Eq. (2.3). Making use of the relation $\partial/\partial t \to i\omega$ and Eq. (2.5) yields:

$$\left[\frac{\partial^2}{\partial z^2} + \mu_0 \omega^2 \varepsilon(\omega)\right] E(\omega,z) = 0. \tag{2.7}$$

The general solution to Eq. (2.7) is

$$E(\omega,z) = |E(\omega,0)|\, e^{i(\omega t - k(\omega)z)}, \tag{2.8}$$

where $|E(\omega,0)|$ is the spectral amplitude, and $k(\omega)$ is the propagation constant with the dispersion relation

$$k^2(\omega) = \omega^2 \varepsilon(\omega) \mu_0 = \frac{\omega^2}{c^2} \varepsilon(\omega). \tag{2.9}$$

A one-dimensional ultrashort optical pulse, $E(t,z)$, is represented as a wave packet, i.e. a coherent superposition of plane waves of different frequencies, ω. In the frequency domain an ultrashort pulse is completely described by its spectral amplitude, $|E(\omega,0)|$, and its spectral phase,

$$\varphi(\omega) = \omega t - k(\omega) z. \tag{2.10}$$

The temporal representation of the wave packet is obtained by FOURIER-transformation,

$$E(t,z) = \frac{1}{\pi}\int_{-\infty}^{+\infty} |E(\omega,0)|\, e^{i(\omega t - k(\omega)z)} \mathrm{d}\omega. \tag{2.11}$$

A linear phase, $\varphi(\omega) = \omega t$, leads to a constructive superposition of all spectral components in the time domain. This yields the shortest possible wave packet, commonly referred to the FOURIER-*limited* (FL) pulse, oscillating at a frequency, ω_c, referred to as the carrier frequency. A defined phase relation between the spectral components is essential. A random phase yields only a random electric field in the time domain, rather than a confined pulse. In contrast, a quadratic phase,

$$\varphi(\omega) = \frac{\beta_2}{2}(\omega - \omega_\mathrm{c})^2, \tag{2.12}$$

leads to a confined pulse in the temporal domain, which is temporally stretched, as compared to the FL pulse. Further, this leads to a time-dependent variation of the instantaneous frequency, $\omega = \omega(t)$, a so-called *chirp*. Here, β_2 is the group-delay dispersion (GDD), expressed in $\left[\mathrm{fs}^2\right]$. The GDD is a common figure-of-merit to quantify the chirp of an ultrashort pulse. Its physical meaning clarifies considering the pulse propagation through an optical material (see Section 2.3). In analogy, around the carrier frequency, ω_c, higher-order phase coefficients are defined by expanding the phase,

$$\varphi(\omega)|_{\omega_\mathrm{c}} = \varphi(\omega_\mathrm{c}) + \sum_{n=1}^{N} \frac{\beta_n}{n!}(\omega - \omega_\mathrm{c})^n, \tag{2.13}$$

with

$$\beta_n = \mathrm{d}^{(n)}\varphi(\omega)/\mathrm{d}\varphi(\omega)^{(n)}\Big|_{\omega_\mathrm{c}}. \tag{2.14}$$

In order to study the influence of quadratic and cubic phase terms on the temporal pulse shape, a FOURIER-transformation was carried out (Eq. (2.11)) using a GAUSSIAN spectrum (Fig. 2.1a, grey) and the corresponding phase (dashed lines). The constant phase (black dashed) yields the FOURIER-limited (FL) pulse shape with a pulse duration of 9.2 fs full width at half maximum (FWHM), as shown in Fig. 2.1b for the intensity (black) and the electric field (red). The quadratic phase (blue dashed) with a GDD of $\beta_2 = 40\,\mathrm{fs}^2$ introduces broadening and chirp (Fig. 2.1c), whereas the cubic phase with a third-order dispersion coefficient (TOD) of $\beta_3 = 720\,\mathrm{fs}^2$ leads to an asymmetric pulse broadening with multiple satellite pulses (Fig. 2.1d).

The optical pulse in the time domain is described by an envelope function for the amplitude, $A(t,z)$, and an oscillation term, $e^{i(\omega t - k(\omega)z)}$, according to

$$E(t,z) = \frac{1}{2}A(t,z)e^{i(\omega t - k(\omega)z)} + \text{c.c.}. \tag{2.15}$$

In order to obtain a first-order propagation equation from the second-order wave-equation (Eq. 2.3), the *slowly-varying envelope approximation* (SVEA) is applied, which is valid, if

$$\left|\frac{\mathrm{d}^2}{\mathrm{d}z^2}A(t,z)\right| \ll \left|k(\omega_\mathrm{c})\frac{\mathrm{d}}{\mathrm{d}z}A(t,z)\right| \text{ and } \left|\frac{\mathrm{d}^2}{\mathrm{d}t^2}A(t,z)\right| \ll \left|\omega_\mathrm{c}\frac{\mathrm{d}}{\mathrm{d}t}A(t,z)\right| \tag{2.16}$$

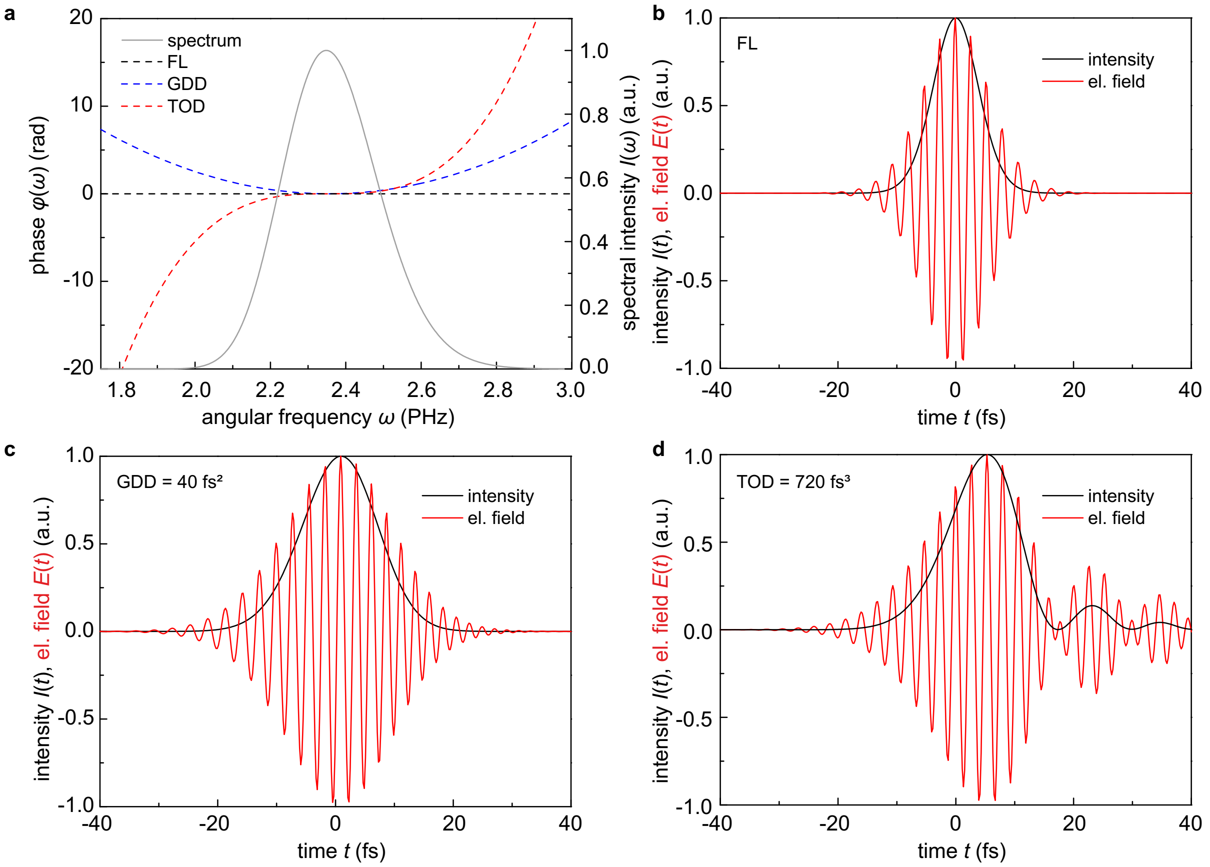

Figure 2.1 Influence of the higher-order dispersion on the pulse shape of a 9.2 fs pulse. (**a**) Spectral intensity (grey), spectral phase of a FOURIER-limited pulse (FL, black), quadratic spectral phase, $\beta_2 = 40\,\mathrm{fs}^2$ (GDD, blue), cubic spectral phase, $\beta_3 = 720\,\mathrm{fs}^3$ (third-order dispersion, TOD, red). (**b**)-(**d**) Corresponding calculated temporal intensities (black) and electric fields (red), see legends. The quadratic phase leads to a pulse broadening and a linear frequency chirp (a). The cubic phase introduces asymmetric broadening and satellite pulses (d).

The envelope is considered to change only very slowly compared to the carrier frequency during the propagation. Thus, the slowly evolving pulse envelope, $A(t,z)$, is split from the rapid oscillation. In vacuum, the SVEA yields

$$\left[k(\omega_c)\frac{\partial}{\partial z}+\mu_0\omega_c\varepsilon(\omega_c)\frac{\partial}{\partial t}\right]A(t,z)=0. \tag{2.17}$$

Even though it is mathematically correct to describe a pulse with only a few optical cycles using the SVEA, it should be carefully checked for the particular problem whether the approximation describes the correct propagation behavior during light-matter interaction.

2.3 Dispersion

During the propagation over a distance, $z = l$ through a material, the pulse properties change in the temporal domain, as the spectral phase accumulates according to $\Delta\varphi(\omega) = k(\omega)\cdot l$. The amount of accumulated phase is different for different spectral components. In the dispersion relation, $k(\omega)$ (Eq. (2.9)), the relative permittivity, $\varepsilon(\omega)$, is frequency-dependent. The physical meaning of the phase change becomes clear by developing the propagation constant in a TAYLOR-series around the carrier frequency,

$$k(\omega)|_{\omega_c}=k(\omega_c)+\left.\frac{\mathrm{d}k}{\mathrm{d}\omega}\right|_{\omega_c}(\omega-\omega_c)+\frac{1}{2}\left.\frac{\mathrm{d}^2k}{\mathrm{d}\omega^2}\right|_{\omega_c}(\omega-\omega_c)^2+\dots \tag{2.18}$$

The first term is related to the phase velocity, v_{ph}, at ω_c within the material:

$$\frac{1}{v_{\mathrm{ph}}}=\frac{k(\omega_c)}{\omega_c} \tag{2.19}$$

The first-order derivative describes the group velocity, v_G, i.e. the speed of the wave packet within the material,

$$\frac{1}{v_G}=\left.\frac{\mathrm{d}k}{\mathrm{d}\omega}\right|_{\omega_c}. \tag{2.20}$$

From the group velocity, we can calculate the temporal shift of the pulse, thus the group delay (GD). It corresponds to the first derivative of the phase,

$$\begin{aligned}T_G&=t-\frac{z}{v_G}\\&=t-\frac{\mathrm{d}k}{\mathrm{d}\omega}\cdot z\\&=\frac{\mathrm{d}\varphi(\omega)}{\mathrm{d}\omega}.\end{aligned} \tag{2.21}$$

The second-order term is related to the group velocity dispersion (GVD). Multiplied by the propagation distance, z, the group delay dispersion (GDD)is obtained, which was introduced in Section 2.2. It equals the second derivative of the optical phase,

$$\begin{aligned}\frac{\mathrm{d}k}{\mathrm{d}\omega}\cdot z&=\frac{\mathrm{d}T_G}{\mathrm{d}\omega}\\&=\frac{\mathrm{d}^2\varphi(\omega)}{\mathrm{d}\omega^2}\\&=\beta_2.\end{aligned} \tag{2.22}$$

If a pulse propagates through a dispersive medium with $\beta_2 \neq 0$, different frequency components will propagate with different group velocities. In the temporal domain, this leads to a chirp, as described in Section 2.2. The GDD is a common figure-of-merit to quantify the chirp of an ultrashort pulse. In analogy, the higher-order phase terms are defined according to Eq. 2.14. In particular for ultrashort pulses in a complex optical system, such as a laser amplifier, the dispersion introduced by each optical element needs to be carefully taken into account in order to achieve a proper pulse compression as close to the FL as possible.

2.4 Nonlinear optical phenomena

High peak intensities can be reached with ultrashort pulses. The response of matter to the corresponding strong electric field can become nonlinear. The field of nonlinear optics includes a great variety of phenomena, governed either by electronic responses or by phononic responses, i.e. response of the crystal lattice. Electronic responses that do not change the quantum mechanical state of the material are referred to as parametric processes. Classically, the electrons are perturbed within the atomic potential by the driving force of the electric field. This induces a polarization, P, which acts as a source term for radiation in the wave equation (see Eq. (2.7)), resulting for example in frequency mixing and self-phase modulation. However, electronic effects exist that change the quantum mechanical state of matter, such as saturable absorption, multiphoton absorption or above-threshold ionization. In this section, first the second-order processes are introduced by means of the optical parametric amplification (OPA) and the noncollinear phase-matching for broadband OPA is described. Further, the basic third-order processes, self-focusing and self-phase-modulation are explained, followed by white-light supercontinuum generation, which includes also nonlinear ionization phenomena.

Parametric processes are treated as *instantaneous*, which means that the response time is much shorter one optical cycle of the electric field. If the electric field strength is on the order of the characteristic atomic electric field strength, $E_{\mathrm{at}} \approx 5 \cdot 10^{11}\,\mathrm{Vm}^{-1}$, the higher-order contributions in the general description of the polarization (Eq. 2.4) are no longer negligible [80],

$$P^{\mathrm{NL}}(\omega,z) = \varepsilon_0 \left[\chi^{(2)} E^2(\omega,z) + \chi^{(3)} E^3(\omega,z) + \cdots\right], \tag{2.23}$$

where $\chi^{(2)}$ and $\chi^{(3)}$ denote the second- and third-order susceptibilities. Generally, E and P are treated as vectors. The susceptibilities, $\chi^{(n)}$, appear as $(n+1)$-th rank tensors.

2.4.1 Optical parametric amplification

Optical parametric amplification (OPA) is a second-order mixing processes, where two light waves interact in a medium with non-vanishing $\chi^{(2)}$. Let us consider the interaction of two light waves,

$$E_m = E_{m,0} e^{i\omega_{\mathrm{P}} t - k(\omega_{\mathrm{P}})z} + E_{m,0} e^{i\omega_{\mathrm{s}} t - k(\omega_{\mathrm{s}})z}, \tag{2.24}$$

with different carrier frequencies, ω_{p} and ω_{s}. The nonlinear coupling of the vector components of the electric field, E_m, to the vector components of the nonlinear polarization, P_l, is described by[3]

$$P_l^{(2)} = \varepsilon_0 \sum_{m=1}^{3} \sum_{n=1}^{3} \chi_{lmn}^{(2)} E_m E_n, \tag{2.25}$$

where $\chi_{lmn}^{(2)}$ is the second-order susceptibility tensor element. The interaction of two light waves leads to the generation of new frequency components in the second-order polarization. This modulated polarization is the source of new electro-magnetic waves oscillating at the sum-frequency, $\omega_{\mathrm{p}} + \omega_{\mathrm{s}}$ (SFG), and the difference-frequency, $\omega_{\mathrm{p}} - \omega_{\mathrm{s}}$ (DFG). Further, a constant term occurs, referred to as optical rectification with $\omega = 0$.

---

[3] provided that KLEINMAN's-symmetry is valid, which is typically the case for optical frequencies that are smaller than the resonance frequency of the material [80].

Optical parametric amplification (OPA) is a special case of DFG, where an idler wave at ω_{id} is generated by mixing a pump wave and a signal wave, resulting in $\omega_{\text{id}} = \omega_{\text{p}} - \omega_{\text{s}}$. Once the idler wave is present in the medium, it again mixes with the pump field to generate a signal wave, $\omega_{\text{s}} = \omega_{\text{p}} - \omega_{\text{id}}$. The mixing continues as idler and signal generate a pump wave. All frequencies generated in this interaction obey the energy conservation law, $\omega_{\text{p}} = \omega_{\text{id}} + \omega_{\text{s}}$. In OPA, the signal and idler waves are amplified by transferring energy from the pump wave to the signal and idler. For a coherent buildup of the signal and idler amplitudes, the phase velocities of all involved waves have to be matched, according to momentum conservation. This means that the wave vectors fulfill the *phase-matching* condition,

$$\mathbf{k}_{\text{p}} = \mathbf{k}_{\text{s}} + \mathbf{k}_{\text{id}}. \tag{2.26}$$

Accordingly, the phase-mismatch is defined as $\Delta\mathbf{k} = \mathbf{k}_{\text{p}} - \mathbf{k}_{\text{s}} - \mathbf{k}_{\text{id}}$. During the propagation, the amplitudes are enhanced until the accumulated phase of the waves reaches $|\Delta\mathbf{k}| \cdot z = \Delta k \cdot z = \pi$. Then, the energy flow reverses back to the pump.

For a certain phase-matching condition, for example for linear polarization of the electric field, and at a particular interaction geometry, the tensor-description can be reduced to a scalar description. Owing to a certain symmetry of the nonlinear crystal, an effective nonlinear optical coefficient, d_{eff}, can be defined. For example, in β-barium borate (BBO) with *type I* phase matching condition (parallel polarizations of the signal and idler waves), it can be expressed as

$$d_{\text{eff}} = d_{31} \sin\theta - d_{22} \cos\theta \sin(3\phi), \tag{2.27}$$

where $d_{lp} = \frac{1}{2}\chi^{(2)}_{lmn}$ is a reduced notation for the nonlinear coefficient[4] [80]. If signal and idler waves have orthogonal polarization (*type II* phase matching condition), the expression gives

$$d_{\text{eff}} = d_{22} \cos^2\theta \cos(3\phi), \tag{2.28}$$

The angle θ denotes the angle between the wave-vector and the crystal's optical axis, the angle ϕ denotes the azimuthal angle between the electric field vector (polarization direction) and the principal plane spanned by the wave-vector and the optical axis of the crystal.

With these symmetry considerations and the SVEA (Eq. 2.16), the energy transfer between the three waves in OPA can be described by the nonlinear coupled equations [81, 82],

$$\begin{aligned}
\frac{\mathrm{d}A_{\text{s}}}{\mathrm{d}z} &= i\frac{\omega_{\text{s}} d_{\text{eff}}}{n(\omega_{\text{s}})c} A_{\text{id}}^* A_{\text{p}} e^{i\Delta kz}, \\
\frac{\mathrm{d}A_{\text{id}}}{\mathrm{d}z} &= i\frac{\omega_{\text{id}} d_{\text{eff}}}{n(\omega_{\text{id}})c} A_{\text{s}}^* A_{\text{p}} e^{i\Delta kz}, \\
\frac{\mathrm{d}A_{\text{p}}}{\mathrm{d}z} &= i\frac{\omega_{\text{p}} d_{\text{eff}}}{n(\omega_{\text{p}})c} A_{\text{s}} A_{\text{id}} e^{-i\Delta kz},
\end{aligned} \tag{2.29}$$

where A_{s}, A_{id} and A_{p} are the complex amplitudes of the signal, idler and pump wave, and $n(\omega)$ denotes the refractive index. This coupled system of one-dimensional first-order differential equations is derived by solving the wave equation (Eq. (2.1)) using the SVEA The analytical solution is given by JACOBI elliptic functions [83], neglecting dispersion and higher-order nonlinear effects. Alternatively, it can be calculated by numerical methods.

---

[4] KLEINMAN's symmetry with $mn \to p$ prescription [80]

For a more descriptive analysis, commonly the *undepleted pump approximation* is used, where the system of equations is reduced to a homogeneous second-order differential equation by assuming $\mathrm{d}A_\mathrm{p}/\mathrm{d}z = 0$. In the nomenclature of laser physics, this corresponds to the small signal gain regime. The parametric intensity gain after an interaction length L within the nonlinear crystal yields

$$G_\mathrm{s}(L) = 1 + \frac{\Gamma^2}{g^2}\sinh^2(gL), \tag{2.30}$$

for the signal and

$$G_\mathrm{id}(L) = \frac{\omega_\mathrm{id}}{\omega_\mathrm{s}}\frac{\Gamma^2}{g^2}\sinh^2(gL), \tag{2.31}$$

for the idler, with

$$g = \sqrt{\Gamma^2 - \left(\frac{\Delta k}{2}\right)^2}, \tag{2.32}$$

and

$$\Gamma^2 = d_\mathrm{eff}^2 \frac{\omega_\mathrm{s}\omega_\mathrm{id}\left|A_\mathrm{p}\right|^2}{n(\omega_\mathrm{s})n(\omega_\mathrm{id})c^2}. \tag{2.33}$$

The signal intensity evolves according to

$$I_\mathrm{s}(L) = 2\varepsilon_0 c n_\mathrm{s}|A_\mathrm{s}(z=0)|^2 G_\mathrm{s}(L), \tag{2.34}$$

the idler intensity evolves according to

$$I_\mathrm{id}(L) = 2\varepsilon_0 c n_\mathrm{id}|A_\mathrm{s}(z=0)|^2 G_\mathrm{id}(L), \tag{2.35}$$

if zero initial idler intensity is assumed, $I_\mathrm{id}(z=0) = 0$.

The evolution of the phases of signal, idler and pump is of particular interest, especially in the case of ultrashort pulses. The expressions for the phases are obtained by solving the imaginary parts of Eqs. (2.29), as described in [84]:

$$\begin{aligned}
\varphi_\mathrm{s}(z) &= \varphi_\mathrm{s}(0) - \frac{\Delta k z}{2} + \frac{\Delta k \gamma_\mathrm{s}^2}{2}\int \frac{\mathrm{d}z}{f+\gamma_\mathrm{s}^2}, \\
\varphi_\mathrm{id}(z) &= \varphi_\mathrm{p}(0) - \varphi_\mathrm{s}(z=0) - \frac{\pi}{2} - \frac{\Delta k z}{2}, \\
\varphi_\mathrm{p}(z) &= \varphi_\mathrm{p}(0) - \frac{\Delta k}{2}\int \frac{f\mathrm{d}z}{1-f}.
\end{aligned} \tag{2.36}$$

Here, γ_s is the input photon intensity ratio for the signal and f is the fractional depletion of the pump,

$$\gamma_\mathrm{s}^2 = \frac{\omega_\mathrm{p}}{\omega_\mathrm{s}}\frac{I_\mathrm{s}(0)}{I_\mathrm{p}(0)} \text{ and } f = 1 - \frac{I_\mathrm{p}(z)}{I_\mathrm{p}(0)}. \tag{2.37}$$

From these equations, important statements for OPA are derived: First, the signal phase is independent from the pump phase. As a consequence, spatial phase aberrations of the pump wavefront are not transferred to the signal wavefront and thus do not affect the spatial beam quality of the amplified beam. Furthermore, also the temporal phase is not transferred to the signal, and a temporally chirped pump beam can be used. Second, parametric phase changes occur only if a phase mismatch is present, $\Delta k \neq 0$. The amount of phase change is larger for large fractional pump depletion, $0 < f \leq 1$. Third, the idler phase depends only on the initial signal and pump phase and the phase mismatch. The best conversion efficiency corresponds to a phase relationship, $\Theta = \varphi_\mathrm{p} - \varphi_\mathrm{id} - \varphi_\mathrm{s} = -\pi/2$. The initial idler phase self-adjusts to $\varphi_\mathrm{id} = \varphi_\mathrm{p}(0) - \varphi_\mathrm{s}(0) + \pi/2$. After a certain propagation distance and at a certain degree of pump depletion, no more energy can be transferred to the signal and idler, $\Theta = 0$. The energy flows from signal and idler back to the pump for $\Theta > 0$. The corresponding characteristic propagation length is the *coherence length*,

$$l_\mathrm{c} = \frac{\pi}{\Delta k}. \tag{2.38}$$

2.4.2 Phase-matching in nonlinear optical crystals

In order to fulfill the phase-matching condition (Eq. (2.26)) of interacting waves in a nonlinear crystal, several techniques have been developed. The quasi phase matching (QPM) technique relies on periodic modulation of d_eff along the propagation axis to keep the phase mismatch $\Delta k < \pi$. This can be achieved for example by periodic poling of ferroelectric crystals, such as lithium niobate (PPLN: periodically poled lithium niobate) [85]. Birefringent phase-matching techniques make use of the matching of the refractive-index ellipsoids for different interacting frequencies at different polarizations. An overview about the different types of birefringence of nonlinear crystals can be found in [86]. For example, for type-I phase-matching in a negative uniaxial crystal, the extraordinary refractive index of the pump wave can be matched to the ordinary refractive index of the signal and idler waves, $n_\mathrm{p}(\theta) = n_\mathrm{s,id}$ by tuning the phase-matching angle θ. The refractive indices are related by

$$\frac{1}{n_\mathrm{e}(\theta)^2} = \frac{\sin^2\theta}{n_\mathrm{e}^2} + \frac{\cos^2\theta}{n_\mathrm{o}^2} \tag{2.39}$$

Alternatively, non-critical phase matching can be achieved by utilizing thermally induced refractive index changes.

In the present work, a high spectral gain bandwidth is pursued that supports pulse durations shorter than 10 fs. In general, broadband phase matching can be expressed by expanding the phase mismatch in a TAYLOR-series around a spectrally varying signal frequency, $\Delta\omega = \omega - \omega_\mathrm{c}$,

$$\Delta k|_{\omega_\mathrm{c}} = \Delta k(\omega_\mathrm{c}) + \left.\frac{\partial \Delta k}{\partial \omega}\right|_{\omega_\mathrm{c}} \Delta\omega + \frac{1}{2}\left.\frac{\partial^2 \Delta k}{\partial \omega^2}\right|_{\omega_\mathrm{c}} (\Delta\omega)^2 + O\left[(\Delta\omega)^3\right]. \tag{2.40}$$

In order to achieve amplification for the maximum spectral bandwidth, all terms in Eq. (2.40) must vanish. The term $\Delta k(\omega_\mathrm{c}) = |\Delta\mathbf{k}|$ refers to a matching of the phase-velocities, as described in Eq. (2.26). The first-order derivative corresponds to a matching of the group velocities of idler and signal, as will be shown below. Higher-order terms, $O\left[(\Delta\omega)^2\right]$, require a higher degree of freedom in the phase-matching configuration, such as using angularly dispersed beam geometries [84, 87]. The required group velocity matching can be achieved by introducing a non-collinear angle, α, between the pump and the signal wave vector. In Fig. 2.2, the wave vector diagram for non-collinear type I phase-matching is shown. In order to fulfill the phase-matching condition for different signal wave vectors, $k_\mathrm{s} + \mathrm{d}k_\mathrm{s}$, the idler and the signal form the angle Ω. The relation between the phase-matching angle, θ, and the non-collinear angle, α, is obtained by applying the cosine rule,

$$k_\mathrm{p}^2 = k_\mathrm{s}^2 + k_\mathrm{id}^2 - 2k_\mathrm{s}k_\mathrm{id}\cos\alpha, \tag{2.41}$$

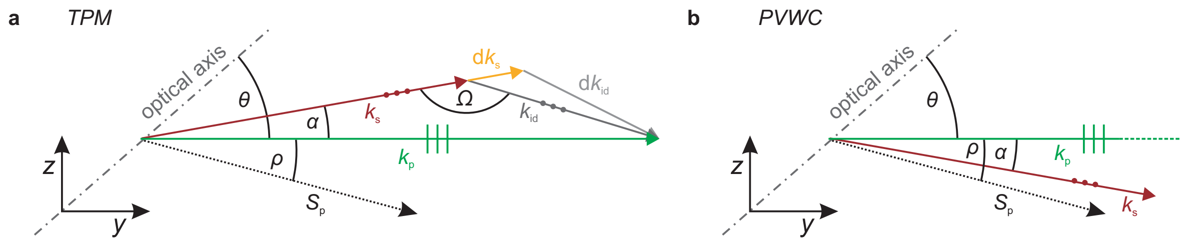

Figure 2.2 Non-collinear phase-matching geometry for broadband OPA. (**a**) In the chosen interaction plane within a negative uniaxial crystal (e.g. the xy-plane), the extraordinarily polarized pump wave vector, k_{p} (green), forms the phase-matching angle, θ, with respect to the optical axis. Owing to the birefringence, the pump wave vector is adjustable by rotating the crystal, $k_{\mathrm{p}} = k_{\mathrm{p}}(\theta)$. The ordinarily polarized signal wave vector, k_{s}, forms the non-collinear angle, α, with respect to the pump wave vector. For a broadband signal with $k_{\mathrm{s}} + \mathrm{d}k_{\mathrm{s}}$, the idler wave vectors, $k_{\mathrm{id}} + \mathrm{d}k_{\mathrm{id}}$, self-adjust in order to fulfill the momentum conservation condition and form the angle Ω. Thus, the generated idler beam is spatially dispersed. The pump wave vector forms the POYNTING-vector walk-off angle, ρ, with respect to the POYNTING-vector, S_{P}, indicating the direction of the energy flow. The presented geometry, with a signal angle of $\theta - \alpha$ with respect to the optical axis, is referred to as tangential phase-matching (TPM), (**b**) POYNTING-vector walk-off compensation (PVWC) scheme with $\theta + \alpha$. The idler wave-vector is not shown.

with the extraordinarily polarized pump, $k_{\mathrm{p}} = \frac{\omega_{\mathrm{p}}}{c} n_{\mathrm{p}}(\theta)$ (Eq. 2.39). The variation of the signal wave vector is addressed by the derivative

$$\begin{aligned} \frac{\partial}{\partial k_{\mathrm{s}}} \left[2k_{\mathrm{p}}k_{\mathrm{s}}(1-\cos\alpha) \right. &= \left. k_{\mathrm{id}}^2 - (k_{\mathrm{p}} - k_{\mathrm{s}})^2 \right], \\ 2k_{\mathrm{p}}(1-\cos\alpha) &= 2k_{\mathrm{id}} \frac{\partial k_{\mathrm{id}}}{\partial k_{\mathrm{s}}} + 2(k_{\mathrm{p}} - k_{\mathrm{s}})(\frac{\partial k_{\mathrm{p}}}{\partial k_{\mathrm{s}}} - 1). \end{aligned} \tag{2.42}$$

From the energy conservation, we obtain $\partial\omega_{\mathrm{id}}/\partial\omega_{\mathrm{s}} = -1$. Thus, the term,

$$\frac{\partial k_{\mathrm{id}}}{\partial k_{\mathrm{s}}} = -\frac{\partial k_{\mathrm{id}}}{\partial \omega_{\mathrm{id}}} \left(\frac{\partial k_{\mathrm{s}}}{\partial \omega_{\mathrm{s}}} \right)^{-1} = -\frac{v_{\mathrm{G,i}}}{v_{\mathrm{G,s}}}, \tag{2.43}$$

expresses the group velocities of the signal and the idler. Combining Eqs. (2.41) and (2.42) yields the group velocity matching in non-collinear geometry [88]:

$$v_{\mathrm{G,s}} = v_{\mathrm{G,i}} \cos\Omega. \tag{2.44}$$

For a fixed geometry of the signal and the pump, the idler wave vector will be angularly dispersed. Equation (2.44) can be equally expressed as [89]

$$\Omega = \sin^{-1}\left(\frac{k_{\mathrm{p}}}{k_{\mathrm{id}}} \cos\alpha \right). \tag{2.45}$$

Non-collinear OPA can be implemented in two geometries: Tangential phase-matching (TPM) and POYNTING-vector walk-off compensation scheme (PVWC). TPM is achieved if the signal travels with an angle $\theta - \alpha$ (with respect to the optical axis), the different directions of the POYNTING-vectors of the pump and the signal wave will lead to a spatial walk-off effect, i.e. the different directions of the energy flows will loose their spatial overlap after a certain propagation distance (see Fig. 2.2a). For PVWC, the signal angle is chosen $\theta + \alpha$ relative to the optical axis. The walk-off is partly compensated (see Fig. 2.2b). Generally, the PVWC leads to a higher pump-to-signal conversion efficiency and a better beam quality, compared to the TPM. However, the choice of the signal direction depends on the applied nonlinear crystal. For example, in β-barium borate (BBO) the PVWC direction covers also the phase-matching angles of the second-harmonic (SH) of signal wavelengths between 800 nm and 1200 nm. The corresponding parasitic SH also limits the pump-to-signal conversion efficiency [90].

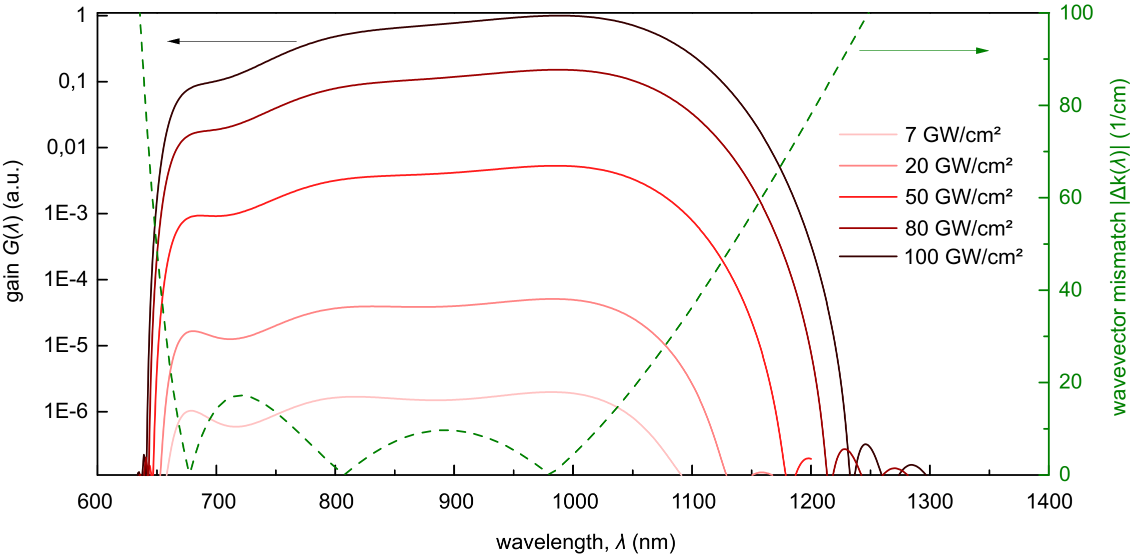

Figure 2.3 Calculated gain, $G(\lambda)$ (red solid line), and wave-vector mismatch, $|\Delta k(\lambda)|$ (green dashed line), in dependence on the signal wavelength for type-I non-collinear phase-matching in a 2 mm BBO. The gain is calculated for different intensities ranging from 7 GW/cm^2 to 100 GW/cm^2 (see legend), using the undepleted pump approximation. Phase-matching angle: $\theta = 24.17°$, non-collinear angle: $\alpha = 2.2°$.

An example for broadband OPA with non-collinear type-I phase-matching in a 2 mm long BBO is presented in Fig. 2.3. Here, first the wave-vectors were calculated, $k = n(\omega) \cdot \omega / c$, for signal, idler, and pump. The refractive indices were obtained from the SELLMEIER-equations (see Appendix A). The extraordinary refractive index of the pump was calculated according to Eq. (2.39), with $\theta = 24.17°$. Finally, the wave vector mismatch was calculated according to

$$|\Delta k| = \left| k_{\mathrm{p}} - k_{\mathrm{s}} \cos(\alpha) - k_{\mathrm{id}} \cos(\pi - \Omega - \alpha) \right|, \tag{2.46}$$

with $\alpha = 2.2°$. In the figure, the wave-vector mismatch (green dashed) is plotted in dependence on the signal wavelength. Correspondingly, the signal gain, $G(\lambda)$, was calculated according to eq (2.30) for different pump intensities (red solid, see legend). The nonlinear coefficient, d_{eff}, is listed in table 4.1 on p. 69. The wave vector mismatch is kept small for a signal wavelength range of about 650–1200 nm. For an intensity of 7 GW cm^{-2}, the gain is reduced for the regions with $\Delta k \neq 0$, leading to clear modulations. With increasing intensity, these modulations become less pronounced and the spectral gain bandwidth increases. This can be explained by looking at the square-root on the right-hand side in Eq. (2.32). For a given Δk, the spectral bandwidth can be increased by increasing the pump amplitude in the left term and by decreasing the interaction length, z, which reduces the influence of the right term. The weaker gain due to a shorter crystal can be compensated by a higher pump intensity. The intensity limit is given by the damage threshold of the nonlinear crystal, which scales approximately with $1/\sqrt{t_\mathrm{P}}$, where t_P is the pulse duration [91]. In conclusion, for an efficient amplification of a broad spectral range, ultrashort pump pulses are required to reach the required high pump intensities. More details about the experimental implementation of OPA are discussed in Chapter 4.

2.4.3 Third-order processes

In most transparent media that are of relevance in optics, the third-order nonlinear polarization term in Eq. (2.23) can be written as [79]

$$P^{(3)} = \varepsilon_0 \chi^{(3)} E^3 = \varepsilon_0 \chi^{(3)} \left(\frac{3}{8} |A|^2 A e^{i\omega_\mathrm{c} t} + \frac{1}{8} A^3 e^{i \cdot 3\omega_\mathrm{c} t} \right) + \text{c.c.} \tag{2.47}$$

This equation is valid for a one-dimensional linearly polarized pulse and the SVEA (see Section 2.2). The $3\omega_\mathrm{c}$ term describes the generation of a third-harmonic wave (THG). If the THG is not phase-matched and sufficiently weak not to affect the fundamental wave, the first term describes the evolution of a nonlinear refractive index,

$$n_2 = \frac{3\chi^{(3)}}{4\varepsilon_0 n_0^2 c}. \tag{2.48}$$

This coefficient is often also referred to as KERR-nonlinearity. The corresponding nonlinear KERR-effect changes the material's refractive index locally in time and space, traveling with the intensity envelope of the laser pulse,

$$n(t,z) = n_0 + n_2 I(t,z), \tag{2.49}$$

where n_0 is the linear refractive index. For non-resonant electronic third-order nonlinearities, the nonlinear refractive index is on the order of $10^{-19}\,\mathrm{cm^2W^{-1}}$ (gases) to $10^{-15}\,\mathrm{cm^2W^{-1}}$ (transparent glasses). The presence of a nonlinear refractive index change is the origin of a variety of nonlinear effects, such as self-focusing (SF, or KERR-lensing), self-phase-modulation, cross-phase modulation, the formation of solitons and self-steepening [79].

Self-focusing occurs for a spatially inhomogeneous intensity profile. The resulting refractive index profile affects the wavefront curvature and acts like a lens. For a GAUSSIAN beam profile, a critical optical power can be defined for the onset of self-focusing[92],

$$P_\mathrm{cr} \approx \frac{0.15\lambda_\mathrm{c}^2}{n_0 n_2}. \tag{2.50}$$

The established GAUSSIAN lens focuses the optical beam (if $n_2 > 0$). Owing to the related increase of intensity, the focusing becomes gradually stronger and may even lead to a beam collapse. Counteracting mechanisms are the linear diffraction of the beam or plasma-defocusing due to multiphoton absorption.

Self-phase-modulation (SPM) means that also the spectral phase of the pulse is modulated by the KERR-nonlinearity. Using the SVEA, the instantaneous frequency, $\omega(t)$, is written as the derivative of the phase,

$$\omega(t) = \frac{\partial \varphi}{\partial t} = \omega_\mathrm{c} - \frac{\omega_\mathrm{c}}{c} \frac{\partial n(t)}{\partial t} z, \tag{2.51}$$

resulting in

$$\omega(t) - \omega_c = \delta\omega(t) = -\frac{\omega_c n_2}{c} z \frac{\partial I(t)}{\partial t}. \tag{2.52}$$

Corresponding to the phase modulation, new optical frequencies are created, which results in a spectral broadening of the laser pulse. In Fig. 2.4a, the intensity of a GAUSSIAN pulse (black) and the instantaneous frequency change, $\delta\omega(t)$ (red), induced in a medium with positive KERR-nonlinearity are calculated in the time domain. Accordingly, in Fig. 2.4b the FOURIER-transformation was calculated to demonstrate the spectral broadening after the characteristic nonlinear interaction length $z = L \cdot c/(\omega_c n_2 I_0)$ for $L = 1, 4, 8, 12, 16$. In this calculation, self-focusing is not included, i.e. the intensity is constant. This is valid for short propagation distances neglecting dispersive effects [79].

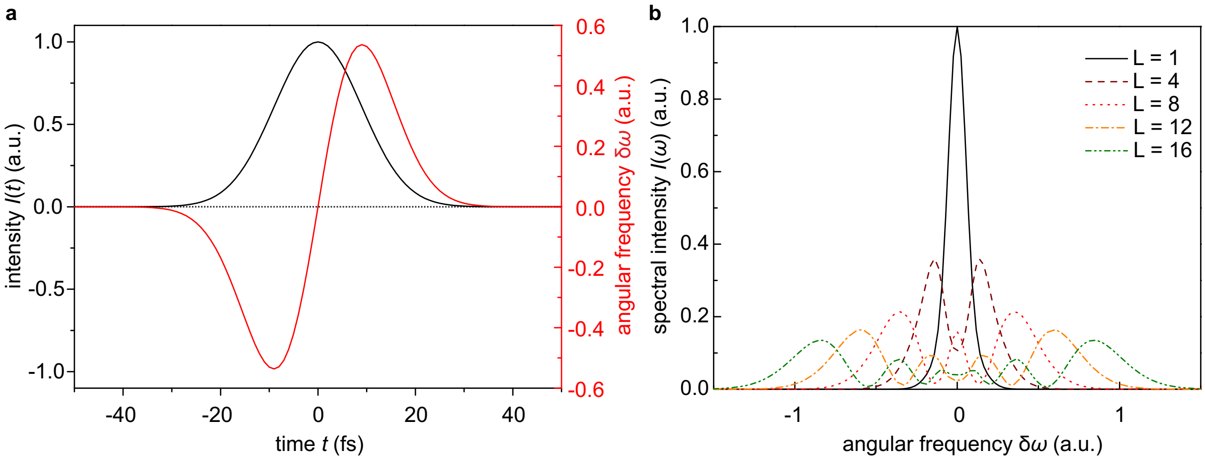

Figure 2.4 Self-phase-modulation (SPM) of a GAUSSIAN pulse. (**a**) The GAUSSIAN intensity envelope (black) induces a phase modulation, $\varphi(t)$, resulting in a frequency modulation, $\delta\omega = \partial\varphi/\partial t - \omega_c$ (red), after a nonlinear interaction length $z = L \cdot c/(\omega_c n_2 I_0)$ $(L = 8)$. (**b**) Corresponding spectral broadening, calculated for different nonlinear interaction lengths with $L = 1, 4, 8, 12, 16$ (see legend).

2.4.4 Filamentation and supercontinuum generation in solids

By focusing an intense ultrashort laser pulse in an optically transparent solid, liquid or gas, a free-electron filament can develop under certain circumstances [92–95]. Filamentation is an interplay of spatial and temporal nonlinear phenomena that lead to a self-guiding and thus a quasi-diffractionless propagation of an ultrashort pulse over a certain distance. The filament itself appears as a light emitting, glowing streak with a diameter of tens to hundreds of µm and a length ranging from a few mm (in solids and liquids) to a few hundreds of meters (in gases) [96]. During propagation, the light pulse experiences a strong nonlinear phase modulation, which leads to supercontinuum generation (white-light generation, WLG), a superbroadening of the optical spectrum. The supercontinuum spectra can cover more than one octave of optical frequencies, which finds many applications not only in the field of ultrafast spectroscopy, but also in the generation of shortest light pulses [92, 97]. A typical WLG spectrum is presented in Fig. 2.5a (blue line), generated in a 10 mm long YAG crystal by focusing 350 fs pulses with a

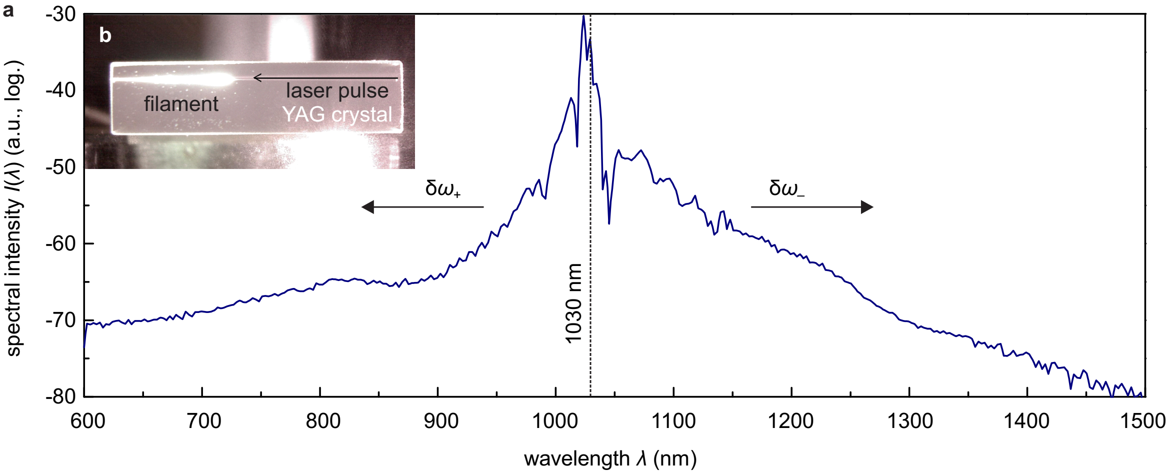

Figure 2.5 White-light supercontinuum generation (WLG). (**a**) Measured WLG spectral intensity (blue line), pumped at the central wavelength $\lambda_c = 1030\,\text{nm}$ (dotted line). Around the pump wavelength, strong modulations are observed, whereas the red-shifted part ($\delta\omega_-$) and the blue-shifted part ($\delta\omega_+$) are very smooth. The blue-shifted part has a cut-off at about 470 nm (not measured here). (**b**) Inset: Image of the polished side-surface of a 10 mm long YAG crystal. The laser pulse is incident perpendicular to this plane on the right side (black arrow). The glowing free-electron filament is clearly visible at the left side.

central wavelength of $\lambda_c = 1030\,\text{nm}$ (dotted line) and a pulse energy of about $1.8\,\mu\text{J}$. The red-shifted part, $\delta\omega_-$, is extended to wavelengths $> 1400\,\text{nm}$. The blue-shifted part has a cut-off at 470 nm (not within the measured range). The wavelength limit for the pump laser is reported not to be less than than $1/3E_{\text{gap}}$ [98]. This limits also the variety of materials that can be used for WLG.

The associated physical mechanisms are complex and also different, depending on whether the processes happen in solids or gases. In this work, the description will focus on WLG in transparent solids. However, the triggering mechanism for WLG is the same for both cases: self-focusing of an ultrashort pulse that exceeds the critical power, P_{crit}. Spatially, the beam undergoes a catastrophic collapse, in which it can reach a very small size. The collapse is stopped by linear diffraction and by plasma-defocusing due to ionization of the material. The plasma refractive index change is induced by the free electrons that are generated by multi-photon ionization (MPI) or avalanche ionization due to the high intensity reached during the collapse. If the numerical aperture is larger than $NA > 0.02$, these counteracting processes will diverge the beam, preventing the formation of a free-electron filament. For weaker focusing, with $NA < 0.02$, the RAYLEIGH-length of the collapsing beam is longer, so that the plasma-defocusing and the self-focusing are in a competing regime. In this filamentation regime, the negative refractive index of the free electrons in the filament, $-\Delta n(n_e)$, and the positive KERR-index, $n_2 I^2$, cancel each other out,

$$n_2 I^2 = -\Delta n(n_e), \tag{2.53}$$

leading to competitive focusing-defocusing cycles and hence the formation of a free-electron filament. The negative plasma refractive index change, $\Delta n(n_e)$, is obtained from Eq. (2.70) in Section 2.5.5. The evolution of the electron density, n_e, depends on the intensity of the pulse and can be calculated according to [93–95, 99]

$$\frac{\mathrm{d}n_\mathrm{e}(t)}{\mathrm{d}t} = \frac{\sigma_K}{K\hbar\omega_\mathrm{c}}\left|E(t)\right|^{2K} + \frac{\sigma_\mathrm{av}}{n^2 E_\mathrm{g}} n_\mathrm{e}(t)\left|E(t)\right|^2 - \frac{n_\mathrm{e}(t)}{\tau_\mathrm{r}}. \tag{2.54}$$

The first term describes the MPI, with the order of the absorption process, K (K-photon absorption), and the MPI cross-section, σ_K. The second term describes the avalanche ionization, i.e. the secondary impact ionization rate with the cross-section for inverse bremsstrahlung, σ_av, the material refractive index, n, and the material electronic band gap, E_g. The third term accounts for the electron decay time, τ_r, which lasts in most cases longer than the laser pulse duration.

For describing the WLG during the filamentation, the SPM theory alone is not sufficient. It has been proposed that a strong SPM enhancement by the fast generation of electrons is the origin of the spectral superbroadening [98]. In particular, the blue shifted components exhibit a strong spectral expansion, according to

$$\delta\omega_+ = \left(-\frac{\partial\varphi}{\partial t}\right)_\mathrm{max}, \tag{2.55}$$

the maximum rate of decrease of the nonlinear phase (see Eq. 2.51). This ionization-enhanced SPM occurs close to the beam collapse, in the onset of filamentation. The temporally trailing part of the pulse experiences a sudden change in phase, originating from the increasing electron density triggered by the leading part of the pulse.

For generating a white-light continuum, the fast MPI contribution plays a key role in WLG using ultrashort pulses. As can be seen from Eq. (2.54), the avalanche ionization term requires a seed electron density within the conduction band. With the typical impurity concentration in transparent solids of $n_\mathrm{imp} \approx 10^8\,\mathrm{cm}^{-3}$ [99], only very low electron densities can be reached ($n_\mathrm{e} < 10^{13}\,\mathrm{cm}^{-3}$ at an intensity of $1.9\,\mathrm{GW\,cm}^{-2}$). Moreover, the avalanche ionization is very slow, so the maximum of the electron density is established only after the pulse. However, in MPI-assisted avalanche ionization, the electrons from the fast MPI process seed the avalanche ionization, leading to an efficient generation of free electrons within the conduction band. This is shown in Fig. 2.6, where the MPI-assisted avalanche ionization is calculated for two different materials, sapphire and yttrium-aluminum-garnet (YAG), during an 850 fs GAUSSIAN pulse with an optical peak power of 5.8 MW. Assuming a filament diameter of 10 µm, the peak intensity is $1.9\,\mathrm{GW\,cm}^{-2}$. Owing to the different band-gap (sapphire: $E_\mathrm{gap} = 8.2\,\mathrm{eV}$, YAG: $E_\mathrm{gap} = 5.9\,\mathrm{eV}$), a 7-photon process is required in sapphire, whereas only a 5-photon process is required in YAG. This difference results in a lower MPI rate in sapphire (Fig. 2.6a, red line), compared to YAG (Fig. 2.6b, red line). Because in sapphire the avalanche contribution is dominant, the increase of the electron density is much slower and a major part is gained only at the falling edge of the intensity envelope. In contrast, in YAG the MPI contribution dominates, leading to a fast increase of the electron density during the rising edge. In addition, the refractive index difference between the nonlinear refractive index and the negative plasma refractive index, $n_2 I - |\Delta n(n_\mathrm{e})|$, was calculated. In sapphire, the index change is dominated by the nonlinear index (Fig. 2.6) and will not lead to filamentation, whereas in YAG, a fast and strong contribution from the plasma index takes place within the FWHM of the falling edge (Fig. 2.6). This effect would be even more pronounced, taking into account also the self-steepening of the falling edge due to the self-phase modulation during the beam collapse [95]. Numerical calculations with the nonlinear SCHRÖDINGER-equation predict that the spatial and temporal interplay between the nonlinear processes are even more complex and the ultrashort pulse is drastically

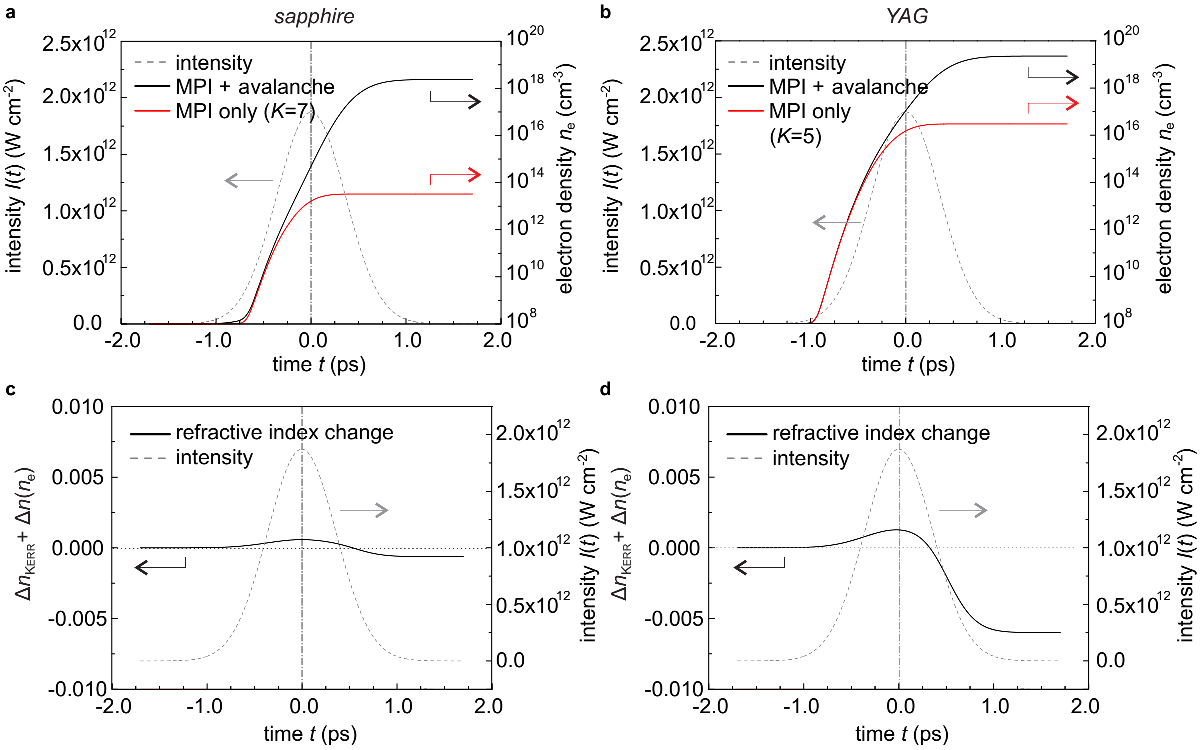

Figure 2.6 MPI-assisted avalanche ionization dynamics and KERR-nonlinearity during an intense laser pulse at a central wavelength of $\lambda_c = 1030\,\mathrm{nm}$ (photon energy $\hbar\omega_c = 1.2\,\mathrm{eV}$). The GAUSSIAN intensity envelope (grey dashed) has a pulse duration of 850 fs FWHM. (**a**) Temporal evolution of the electron density (black) in sapphire. The contribution of multiphoton ionization (MPI, red) is more than 4 orders of magnitudes smaller compared to the slower MPI assisted avalanche ionization, because a 7-photon process is required ($K = 7$). (**b**) Temporal evolution of the electron density in yttrium-aluminum-garnet (YAG). Here, the MPI contribution is dominant, because only 5-photons are required to overcome the electronic band-gap. Thus, the electron density increases much faster and reaches $n_e = 10^{17}\mathrm{cm}^{-3}$ before the intensity maximum of the laser pulse. (**c**) Corresponding difference between the nonlinear refractive index, $\Delta n_{\mathrm{Kerr}} = n_2 I$, and the plasma refractive index, Δn_e, in sapphire (black). (**d**) Corresponding refractive index difference in YAG (black).

reshaped in space and time [93, 95, 100]. Dispersive effects lead, for example, to a complex temporal splitting and self-compression of the pulses.

In general, sapphire is a highly suitable and commonly used material for stable WLG from sub-100 fs pump pulses at a center wavelength of $\lambda_c = 800\,\text{nm}$. In this case the MPI rate is increased, because only a 6-photon process is required to overcome the band gap and higher intensities are reached in a shorter time.

The beam divergence of the spectrally broadened components (hereafter referred to as *WLG pulse*) is comparable to that of the pump pulse, even though the pump pulses suffered strong self-focusing. It is assumed, that self-guiding is the key mechanism to explain that unexpected behavior. The WLG pulse propagates along with the pump pulse and is guided by the competing focusing-defocusing cycles of the pump. At the end of the filament, the WLG pulse is coupled out, comparable to a guided mode out of an optical fiber. The associated beam profile is very smooth and has a GAUSSIAN intensity envelope, surrounded by a halo. Spatial filtering of the halo by an aperture yields a GAUSSIAN beam [92].

Concerning the coherence properties, it has been shown that the red-shifted components as well as the blue-shifted components have a defined phase relationship [92]. It has also been demonstrated that the broadband WLG pulses can be temporally compressed close to the FOURIER-limit of a selected spectral range [97]. The amount of dispersion that has to be compensated corresponds approximately to the amount of crystal material. Correspondingly, it was observed that the WLG components are created very early, during the onset of the filamentation process [98]. This observation also agrees with the theory of SPM enhancement of free-electron generation described above. In conclusion, filamentation and WLG in transparent solid materials is a promising method to achieve broadband, compressible pulses with a good beam quality for versatile scientific and technical applications. In this work, WLG in YAG (Section 4.4) and in sapphire crystals (Section 3.7) play a particularly important role for providing broadband signal seed pulses for the optical parametric amplification of ultrashort light pulses.

2.5 Ionization dynamics in insulators and semiconductors

The physical interaction between XUV or X-ray pulses with solid-state materials can be investigated on an ultrafast timescale using free-electron lasers or table-top sources. Pulse durations in the femtosecond-regime allow to observe fundamental electronic processes, such as electron-electron interactions or electron-lattice collisions. Electronic processes are much faster owing to the large mass ratio of about 10^{-4} compared to the lattice ions. This allows to separately investigate the dynamics within the electronic subsystem during the irradiation with ultrashort pulses. If the photon energy is larger than the band gap of the material, $\hbar\omega > E_\mathrm{g}$, direct photoionization occurs from bound states of deep atomic shells and the valence band to high-energy states of the conduction band.

2.5.1 Excitation processes

Direct photoionization

In Fig. 2.7 the partial density of states (DOS) is shown for the valence band and the conduction band formed by the 3s and 3p-states of solid silicon at room temperature [101, 102]. The DOS represents the number of quantum mechanical states per energy interval that can be occupied by an electron. The L-edges and the K-edge (100 eV, 148 eV, 1.8 keV, respectively) can be considered as delta-functions. In the room temperature thermal equilibrium, mainly the valence band states are occupied and the conduction band states are almost empty. An XUV or X-ray photon can excite the system by transferring its energy and momentum to an electron with a probability corresponding to the DOS. Depending on the photon energy, $\hbar\omega_\mathrm{FEL}$, and the initial state of the bound electron with an ionization potential, I_P, it is lifted to a high energy state with the initial energy:

$$E_\mathrm{e} = \hbar\omega_\mathrm{FEL} - I_\mathrm{P}. \tag{2.56}$$

Correspondingly, after each electron excitation a hole remains within the valence band or a deeper shell with an energy of $E_\mathrm{h} = -I_\mathrm{P}$. The energies are measured with respect to the lowest energy state within the conduction band.

Secondary processes

After the primary ionization, the electron is treated as an energetic free electron. If the energy of this primary electron is sufficiently high, it will most likely transfer its energy to other electrons, triggering secondary ionization cascades. Either impact ionizations or AUGER-like decays may occur. As shown in the schematic band diagram of silicon in Fig. 2.7b (black arrows), a primary electron, e_1, can ionize a second electron, e_2, by collision if its energy exceeds a threshold energy, $E_\mathrm{e}^\mathrm{min} \approx E_\mathrm{g} \approx 1.2$ eV, which is approximately as high as the indirect band gap, E_g [103].

For an AUGER-like decay, a hole, h, with sufficient high energy deep in the valence band or in a deep shell recombines with an electron in the upper valence band or in an upper shell. The excess energy is sufficient to ionize another electron from the upper valence band, e_A, as also shown in Fig. 2.7b (blue arrows). The threshold energy in this case is $E_\mathrm{h}^\mathrm{min} = -3$ eV, measured with respect to the bottom of the conduction band. Below these thresholds, the primary electrons will not be able to trigger further secondary ionizations.

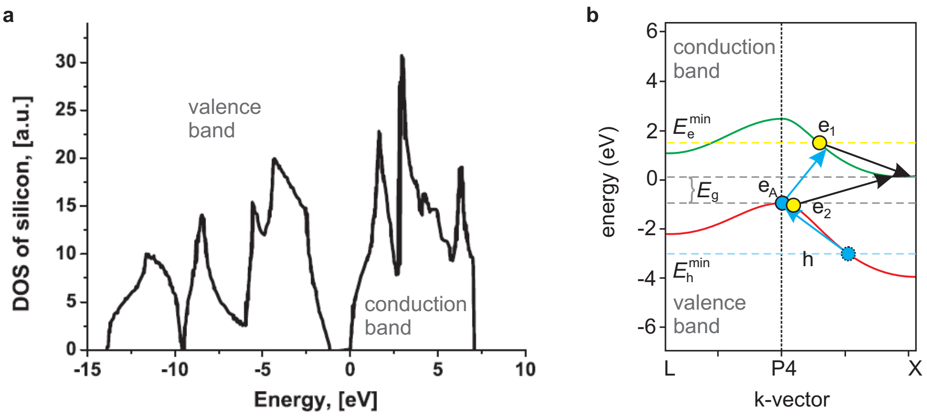

Figure 2.7 Electronic properties of silicon. (**a**) Density of States (DOS) within the valence band and the conduction band [101]. The deeper shells are not plotted. (**b**) Impact ionization (yellow circles, black arrows) and AUGER decay (blue circles, blue arrows) in the schematic band diagram of silicon according to ref. [101]. Impact ionization may occur if the primary photoelectron, e_1, transfers its sufficient energy of E_e^{min} to a second electron, e_2, in the valence band by collision in order to allow that secondary electron to overcome the indirect band gap, E_g. An AUGER-like decay may occur if the remaining hole, h, after the primary photoionization transfers its sufficient energy, E_h^{min}, to an AUGER-electron in the valence band. From [101].

2.5.2 Numerical Methods

The temporal evolution of the ionization dynamics within solid-state materials can be numerically studied [104–106]. Using a classical particle approach, the complex stochastic many-particle system can be solved efficiently with a dedicated Monte Carlo method [101, 104, 107–109]. The method is based on tracing individual particles event-by-event. In each time step the equations of motion for all involved particles (e.g. photons, electrons, holes) are solved in a deterministic way. Probabilities for impact ionizations, elastic scattering and AUGER-like events are estimated with statistical cross-sections, σ, taken from quantum mechanics.

The simulation scheme is as follows [101]: First, the absorption of the XUV or X-ray photons into the material is simulated, taking into account the attenuation length $1/\alpha_{\text{FEL}}$. For example, the attenuation length within different materials is plotted in Fig. 2.8 for photon energies ranging from 30 eV to 8 keV [110]. If the photon lies within the simulation box, its energy is transferred to a randomly chosen bound or free electron. The probability of which energy state the photoabsorption occurs is calculated from the corresponding attenuation lengths.

For modeling the cascading of secondary processes, first, all possible path lengths are determined corresponding to all possible collision events, taking into account the scattering cross-sections, σ. The shortest obtained length determines the choice of the bound electron to be ionized. The energy transferred to the bound electron in the simplest case can be calculated as follows:

$$\Delta E_e = E_e \left[1 + \left(\frac{b}{a_0} \right)^2 \left(\frac{E_e}{2\text{R}} \right)^2 \right], \tag{2.57}$$

where E_e is the kinetic energy of the primary free electron, b is the impact parameter between free electron and bound electron, which is randomly chosen, $a_0 = 0.53$Å is the Bohr radius,

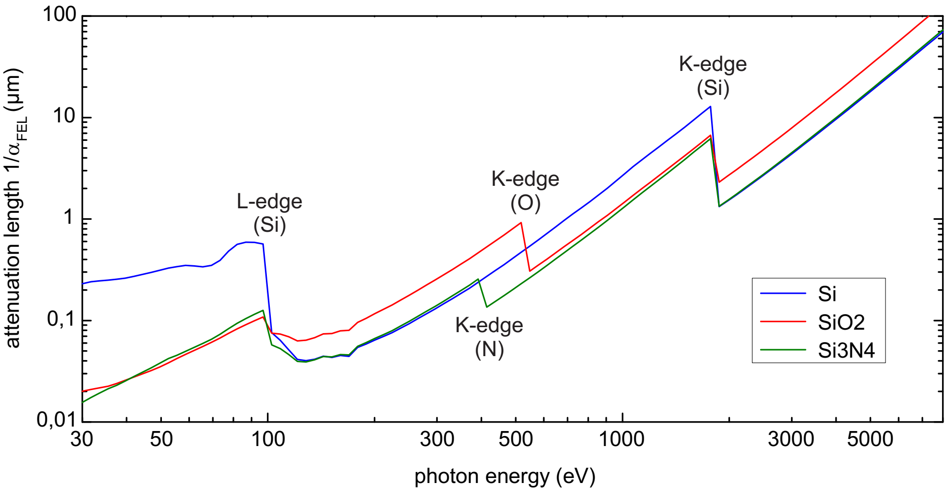

Figure 2.8 Attenuation length of Si (blue), fused silica (red) and Si_3N_4 (green) as a function of the photon energy. Data provided by [110].

and R = 13.6 eV is the RYDBERG constant. If the energy of the photo-excited electrons is still above the threshold for impact ionization (see Section 2.5.1), the process is considered again. In this way the dynamics of all cascades are obtained. For the AUGER-like processes the decay of holes is treated purely stochastically. A decay-time of a hole is sampled according to the POISSON process (exponential decay) [111], with the mean decay time set as the time of the AUGER-decay for the particular atom. Then, the both electrons participating in the AUGER-decay are chosen randomly: one within the valence band fills the hole, the other one gains the excess energy and gets ionized.

The electron correlation effects that result from the band structure of the material [112] and PAULI's principle for photo-excited electrons within the conduction band are also taken into account. To account for PAULI's principle a factor $w \propto f_v\,(1 - f_c)$ is multiplied to the scattering cross-sections. Here, f_v and f_c represent the electron distribution within the valence band and the conduction band, respectively. If there is no free state to be occupied by an electron, the factor and the corresponding cross-section is zero and the particular event is not possible.

2.5.3 Effective energy gap

The total number of electrons, N_e, that are created by a single photon can be expressed in terms of an effective energy gap, E_{eg} [2, 101, 113]:

$$N_e = \frac{\hbar\omega_{FEL}}{E_{eg}}, \tag{2.58}$$

with the photon energy of the free-electron laser pulse, ω_{FEL}. The effective band gap was introduced because secondary processes are restricted to energy and momentum conservation. Furthermore, the electrons are ionized from more than just the highest state of the valence band and can occupy more than just the lowest state of the conduction band. As a consequence, on femtosecond timescales less electrons are produced than predicted by the ratio between photon energy and the indirect band-gap of the material. The effective energy gap can be estimated as:

	E_{gap} (eV)	$E_{\text{e}}^{\text{min}}$ (eV)	$\left\|E_{\text{h}}^{\text{min}}\right\|$ (eV)	E_{eg} (eV)
Si	1.15	1.2	3	2.26
SiO_2	8.9	13.5	12.5	17
Si_3N_4[a]	4.5	4.5	9	9

[a] estimated from [114]

Table 2.1 The band gap energy, E_{gap}, the threshold energy for impact ionization, $E_{\text{e}}^{\text{min}}$, the threshold for AUGER-like processes, $\left|E_{\text{h}}^{\text{min}}\right|$, and the corresponding effective energy gap, E_{eg}, for different materials. Data provided by [113].

$$E_{\text{eg}} = \frac{1}{2}\left(E_{\text{gap}} + E_{\text{e}}^{\text{min}} + \left|E_{\text{h}}^{\text{min}}\right|\right). \tag{2.59}$$

In Table 2.1, the band gap energy, E_{gap}, the threshold energy for impact ionization, $E_{\text{e}}^{\text{min}}$, the threshold for AUGER-like processes, $\left|E_{\text{h}}^{\text{min}}\right|$, and the corresponding effective energy gap, E_{eg}, are listed for different materials. The values for Si and SiO_2 are taken from [101]. The values for Si_3N_4 are estimated from its electronic band structure [114].

2.5.4 Electron dynamics within fused silica

For photon energies that are larger than the E_{eg}, secondary electron production starts to govern the increase of the free-electron density during the irradiation with an ultrashort XUV or X-ray pulse. The temporal dynamics of this dependence was studied using the Monte Carlo simulation described in Section 2.5.2 [109]. Calculations of the time-dependent free-electron density were carried out on the timescale of 200 fs. The irradiation of a fused silica sample by a GAUSSIAN FEL pulse with a pulse duration of 1 fs FWHM was simulated with varying photon energy ranging from 20 eV to 10 keV (Fig. 2.9). For a photon energy of 20 eV (red solid), the rise time of the electron density is approximately as fast as the rise time of the FEL fluence. With increased photon energy up to 1 keV (green dashed), the rise time is on the order of a few femtoseconds. With further increased photon energy up to 10 keV (black dashed), the rise time is on the order of tens of femtoseconds, which is very slow compared to the FEL pulse duration. This can be explained by the high energy that a single photoelectron receives. As mostly only a little fraction of the energy is lost in a single collision, multiple cascades of secondary processes are required to release this high energy. Thus, the density of lower-energy photoelectrons increases due to the secondary ionizations, lasting for tens of femtoseconds in the high energy case. For example, a photoelectron with $E_{\text{e}} = 7$ keV needs about 40 fs to release its energy by cascading secondary ionization processes. In contrast, a single photoionization event is expected to happen on the attosecond timescale [115].

Depending on the band structure of a particular material, additional loss channels may contribute to an ultrafast relaxation on the femtosecond scale [104, 116–118]. In fused silica, an ultrafast decay of the electron density was observed with a time constant of $\tau \approx 150$ fs scale (see Fig. 2.9) [65, 119, 120]. This decay is attributed to the formation of excitons, which are stable electron-hole pairs formed closely below the conduction band with a binding energy of up to 1 eV [121–123]. If no such ultrafast relaxation channels are present, the photoelectrons can be considered to remain stable in the conduction band on the femtosecond timescale. Thus, during the irradiation with an XUV or X-ray pulse the density of free electrons within the material will increase, and, after the pulse, the electrons will remain within the high energy states for time scales of picoseconds to nanoseconds, if no additional ultrafast relaxation mechanisms are available.

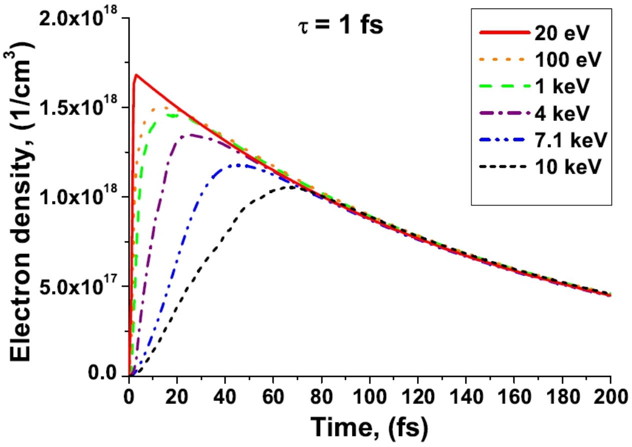

Figure 2.9 Temporal dynamics of the electron density within fused silica during the irradiation with a 1 fs FEL pulse of different photon energy ranging from 20 eV (red solid) to 10 keV (black dashed). The absorbed fluence is kept constant. With increasing photon energy the rise time of the electron density increases, because the sequence secondary processes takes longer. Figure from [109].

2.5.5 Optical properties of a free-electron plasma

DRUDE model

The optical properties of the photo-excited material are changing dramatically owing to the presence of the high density of free electrons, n_e. The relative permittivity is derived by treating these electrons as a free-electron plasma, considering a uniformly distributed charge $q_\mathrm{e} = -n_\mathrm{e} e$ within an arrangement of positively-charged static lattice ions. Here, e is the elementary charge. If an electric field, E, is applied to this system, the electrons are displaced by a distance x with respect to the lattice, resulting in a polarization density,

$$p = -n_\mathrm{e} e x, \tag{2.60}$$

and a restoring electric field,

$$E_\mathrm{r} = \frac{n_\mathrm{e} e x}{\varepsilon_0}. \tag{2.61}$$

The motion of the electrons within the electric field is described by the restoring force,

$$m_\mathrm{e} \frac{\mathrm{d}^2 x}{\mathrm{d}t^2} = e E_\mathrm{r}. \tag{2.62}$$

An important property of plasmas, the rapid plasma oscillation, can be obtained by solving Eq. (2.62). Substituting E on the right-hand side by Eq. (2.61) yields a harmonic-oscillator equation. Its solution describes an oscillatoric electron motion with the frequency

$$\omega_\mathrm{p}^2 = \frac{n_\mathrm{e} e^2}{\varepsilon_0 m_\mathrm{e}} \tag{2.63}$$

For electrons with low kinetic energy, this oscillation is an inherent property of the plasma and its frequency, ω_{P}, only depends on the electron density. In the next paragraph it will be shown how this affects the optical properties of the plasma.

We now let the electric field oscillate at an optical frequency, ω, resulting in $E_{\mathrm{r}} = E(\omega) = E_0 e^{-i\omega t}$. The polarization density will also oscillate, $p = p(\omega) = p_0 e^{-i\omega t}$. From Eqs. 2.60 and 2.62 we derive

$$m_{\mathrm{e}}\frac{\mathrm{d}^2 x}{\mathrm{d}t^2} = \frac{m_{\mathrm{e}}\omega^2}{n_{\mathrm{e}}} p_0 e^{-i\omega t} = eE_0 e^{-i\omega t}, \tag{2.64}$$

and obtain the relation

$$p(\omega) = -\frac{n_{\mathrm{e}}e^2}{m_{\mathrm{e}}\omega^2} E(\omega) \tag{2.65}$$

According to Eq. (2.5) and (2.65), the relative dielectric permittivity is expressed as

$$\varepsilon(\omega) = 1 + \frac{p(\omega)}{\varepsilon_0 E(\omega)} = 1 - \frac{n_{\mathrm{e}}e^2}{m_{\mathrm{e}}\omega^2}. \tag{2.66}$$

By use of the relation in Eq. (2.63) we obtain the relative permittivity as a function of the optical frequency and the plasma frequency:

$$\varepsilon(\omega) = 1 - \frac{\omega_{\mathrm{P}}^2}{\omega^2} \tag{2.67}$$

For optical frequencies that are higher than the plasma frequency, $\omega > \omega_{\mathrm{P}}$, the plasma is transparent as the dielectric function becomes positive. For smaller frequencies, $\omega < \omega_{\mathrm{P}}$, the plasma becomes optically opaque. We can thus define a critical electron density,

$$n_{\mathrm{c}} = \frac{\varepsilon_0 m_{\mathrm{e}}}{e^2}\omega^2, \tag{2.68}$$

for the resonance case $\omega = \omega_{\mathrm{P}}$.

The model of Spitzer and Shkarofsky

Depending on the atomic structure of the material as well as on the energy and density of the electrons, scattering at the lattice ions will affect the dielectric response. From the statistically averaged Coulomb collisions, a mean collision time, $\tau_{\mathrm{el-ion}}$, and a corresponding mean collision frequency, $\omega_{\mathrm{el-ion}} = 2\pi/\tau_{\mathrm{el-ion}}$, can be defined [124–126],

$$\omega_{\mathrm{el-ion}} = \frac{4\sqrt{2\pi}e^4}{(4\pi\varepsilon_0)^2}\frac{n_{\mathrm{e}}Z_{\mathrm{eff}}}{T_{\mathrm{e}}^{3/2}}\ln(\Lambda), \tag{2.69}$$

taking into account the average degree of ionization, Z_{eff}, the electron temperature, T_{e}, and the Coulomb-logarithm, $\ln(\Lambda)$, which represents a geometric impact parameter. The relative permittivity with electron-ion collisions included is then expressed as:

$$\varepsilon(\omega) = 1 - \frac{\omega_{\mathrm{P}}^2}{\omega^2}\left(\frac{1}{1+f^2} + i\frac{f}{1+f^2}\right), \tag{2.70}$$

with the damping factor, $f = \omega_{\mathrm{el-ion}}/\omega$.

Refractive index

The optical properties of the relative permittivity functions obtained from Eqs. (2.67) and (2.70) are evaluated in Fig. 2.10 for an electron density of $n_\mathrm{e} = 1.7 \cdot 10^{27}\ \mathrm{m}^{-3}$. The complex refractive index,

$$\tilde{n}(\omega) = \sqrt{\varepsilon(\omega)}, \tag{2.71}$$

is calculated for the case without electron-lattice collisions (dashed lines) and for the case with electron-lattice collisions included (solid lines). The real part, $\Re(\tilde{n})$, corresponds to the refraction (usual refractive index), whereas the imaginary part, $\Im(\tilde{n})$, is related to the absorption coefficient. Without collisions, a sharp resonance occurs at the plasma frequency, $\omega_\mathrm{P} = 2.32$ THz. In contrast, with collisions included, the resonance is damped and refraction and absorption occur simultaneously.

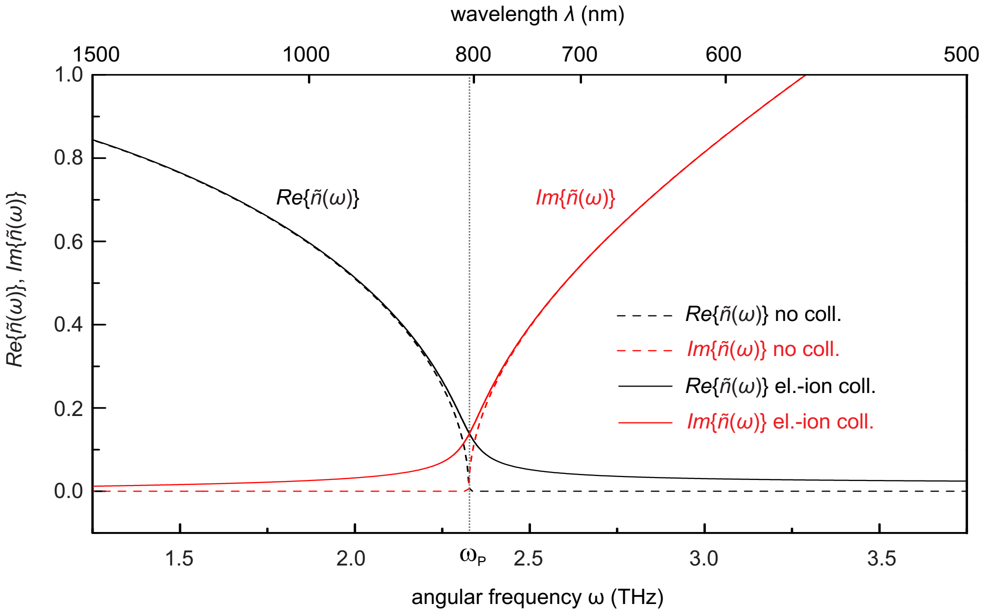

Figure 2.10 Complex refractive index, $\tilde{n} = \sqrt{\varepsilon(\omega)}$, of a free-electron plasma. Real part (black) and imaginary part (red) for an electron density of $n_\mathrm{e} = 1.7 \cdot 10^{27}\ \mathrm{m}^{-3}$. It is calculated for the case of a free-electron plasma without electron-ion collisions (dashed line) and the free-electron plasma with electron-ion collisions included (solid line), according to Eqs. 2.67 and 2.70, respectively. In the latter case, $\ln(\Lambda) = 3$, is assumed [124]. The electron temperature is $T_\mathrm{e} = 10\,\mathrm{eV}$, according to theoretical simulations. With the absence of collisions, a sharp resonance occurs at the plasma frequency, $\omega_\mathrm{P} = 2.32$ THz. With collisions included, the resonance is damped and both contributions, $\Re[\tilde{n}(\omega)]$ and $\Im[\tilde{n}(\omega)]$ are present on each side.

2.6 Temporal characterization of ultrashort pulses

Ultrashort laser pulses are the shortest signals artificially generated by mankind. Hence, ultrashort pulse metrology must rely on ultrafast optical processes, such as nonlinear parametric processes. The duration of a few-femtosecond pulse is orders of magnitudes shorter than the detector response time of a photodiode or electronic oscilloscopes ($> 10\,\mathrm{ps}$ at bandwidth $< 100\,\mathrm{GHz}$). For that reason, the detector will always integrate over a temporal window that is very large compared to the signal to be measured. This requires optical gating of one pulse against another for different time delays, Δt. In this section, an intensity cross-correlation and a spectral interferometric method will be highlighted, as these are important optical pulse duration measurement techniques used in this work. Of course, many concepts and various experimental implementations exist, that cannot be discussed within the scope of this work. A basic review can be found in [127].

2.6.1 Intensity cross-correlation and autocorrelation

In the situation where a well-defined ultrashort reference pulse is already available, the unknown optical pulse can be sampled with this signal. From the intensity cross-correlation function,

$$S(\Delta t) = \int_{-\infty}^{+\infty} I_1(t) I_2(t-\Delta t)\mathrm{d}t, \tag{2.72}$$

between the intensity of the unknown laser pulse, $I_1(t)$ with the unknown pulse duration τ_1, and the reference pulse, $I_2(t)$ with the known pulse duration τ_2, one can extract the intensity $I_1(t)$ by deconvolution. For GAUSSIAN pulses, the cross-correlation function yields also a GAUSSIAN function with a pulse duration of $\tau_S^2 = \tau_1^2 + \tau_2^2$. The duration of the unknown pulse is obtained by

$$\tau_1 = \sqrt{\tau_S^2 - \tau_2^2}. \tag{2.73}$$

In the ideal case, the reference pulse is much shorter than the unknown pulse and can be considered as a delta-function ($\tau_S = 0$). For reference pulses that approach the pulse duration of the unknown pulse or are even longer, the error becomes very large.

In most situations, no well characterized reference pulse is available and the unknown pulse itself is used as the reference pulse, $I_2(t) = I_1(t)$. This case corresponds to an intensity autocorrelation. However, because an infinite number of pulse shapes leads to similar symmetric autocorrelations, only rough information about the pulse shape and the actual pulse duration can be extracted. But owing to its relatively simple experimental implementation, intensity-autocorrelation is a widely used method for the characterization of ultrashort pulses. In practical situations, basic properties about the pulse shape can be assumed and allow for determining the pulse duration. For example, from Eq. (2.73) the pulse duration of a GAUSSIAN pulse is determined from its autocorrelation width, $\tau_{\mathrm{AC}} = \tau_S$, according to

$$\tau_1 = \frac{1}{\sqrt{2}}\tau_{\mathrm{AC}}. \tag{2.74}$$

Experimentally, an intensity auto- or cross-correlation is obtained by overlapping the two pulses (or two replicas) in a second-order nonlinear medium to obtain an intensity-dependent signal. Most commonly used is the sum-frequency generation (SFG) with type-I phase matching, as

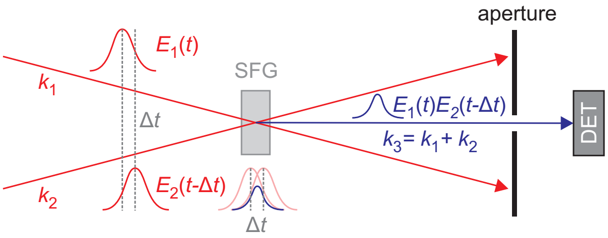

Figure 2.11 Schematic setup of an intensity cross-correlator, relying on sum-frequency generation with type-I phase-matching. The two pulses, $E_1(t)$, with wave vector k_1 and $E_2(t-\Delta t)$ with wave vector k_2 and delay Δt (with respect to E_1), are overlapped in a nonlinear crystal. The generated sum-frequency is proportional to $E_1(t)E_2(t-\Delta t)$ and its wave-vector is directed according to the phase-matching condition, $k_3 = k_1 + k_2$. The background contributions are spatially separated and blocked by the aperture. The detector (DET) signal yields the intensity cross-correlation.

shown in Fig. 2.11. The delay, Δt, is introduced by an optical delay stage. The sum-frequency signal is generated by the overlapping electric field of both pulses, $[E_1(t) + E_2(t-\Delta t)]^2$. With a non-collinear setup, the fields of the fundamental frequency and their respective second-harmonic fields are spatially separated by an aperture. Because of momentum conservation, $k_3 = k_1 + k_2$ (the wave vectors), only the contribution proportional to $E_1(t)E_2(t-\Delta t)$, which is generated between k_1 and k_2 passes the aperture and reaches the detector, yielding

$$S(\Delta t) \propto \int_{-\infty}^{+\infty} |E_1(t)E_2(t-\Delta t)|^2 \,\mathrm{d}t \propto \int_{-\infty}^{+\infty} I_1(t)I_2(t-\Delta t)\mathrm{d}t, \tag{2.75}$$

because the slow detector integrates the optical intensity over the time. In order not to distort the measurement, the dispersion of all involved optical elements must be carefully taken into account (or avoided). For the SFG, the phase-matching bandwidth must be larger than the bandwidth of the measured pulses, which requires a short coherence length, l_c (Eq. 2.38).

2.6.2 Phase-sensitive methods

In general, autocorrelation measurements are afflicted with ambiguities. Even higher-order autocorrelations, $S(\Delta t) = \int_{-\infty}^{+\infty} I(t)I^n(t-\Delta t)\mathrm{d}t$, with $n > 1$, only yield the intensity envelope[5]. However, for many applications it is of importance to know the exact evolution of the electric field. Thus, methods are developed that also allow for the unambiguous retrieval of the phase. One of such methods is the *spectral interferometry for direct electric field reconstruction* (SPIDER) [128]. This technique makes use of measuring a single-shot spectral interferogram and applying a linear phase retrieval procedure. The interferogram results from the interference of two pulse replicas, described by their complex electric fields in the frequency domain, $E_1(\omega_c)$ and $E_2(\omega_c + \Omega)$, respectively (i.e. the inverse FOURIER-transformation of Eq. (2.15). The two pulses are spectrally sheared, i.e. the carrier frequency of the second pulse is shifted by Ω with respect to the first pulse. Fig. 2.12 displays a schematic experimental implementation. First, the pulse is split by a beam splitting device (BS), whereupon one fraction is temporally stretched and strongly chirped in a dispersive element (stretcher). The other fraction passes a MICHELSON-interferometer (M), where the two replicas, E_1 and E_2, are generated with a temporal delay,

---

[5] This is a consequence of the one-dimensional phase-retrieval problem. However, with additional measurements, for example the spectrum, one can iteratively calculate the spectral phase with reasonable accuracy [79]

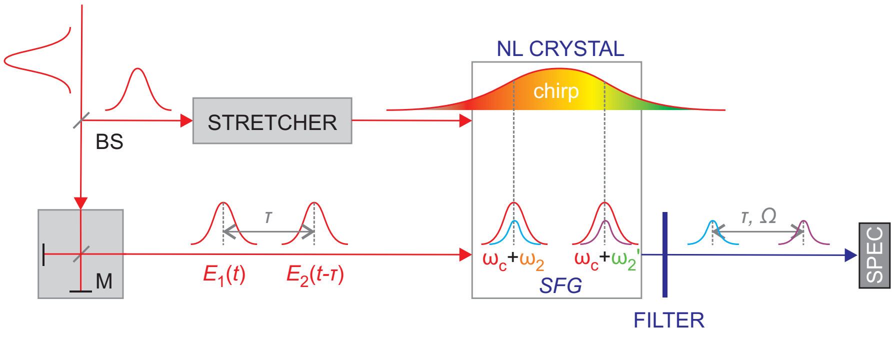

Figure 2.12 Schematic of the spectral interference for direct electric field reconstruction (SPIDER) technique. An ultrashort pulse passes a beam-splitting device (BS). One fraction is strongly chirped in a dispersive stretcher to obtain a strong time-dependence of its instantaneous frequency. The other fraction passes a MICHELSON-interferometer (M) where two replicas are generated with the electric field representations, $E_1(t)$ and $E_2(t-\tau)$ and a temporal delay, τ, with respect to each other. The two replicas are overlapped with the chirped pulse in a nonlinear crystal for sum-frequency generation. Because of the chirp, the two replicas mix with different frequencies, resulting in the sum-frequencies $\omega_c+\omega_2$ and $\omega_c+\omega_2'$, respectively. After passing a high-pass filter (SFG pass), the spectral interferogram is measured with a spectrometer. The SPIDER interferogram contains full information about the spectral phase, obtained from a single-shot measurement.

τ, with respect to each other. Then, in order to achieve the spectral shear, the two replicas are overlapped with the stretched part in a nonlinear crystal for sum-frequency generation (SFG, type-II). Because of the strong temporal frequency dependence of the chirped pulse, each of the two replicas mixes with a different frequency, ω_2 and ω_2', respectively. Thus, two new replicas are created, identical to the two input replicas, but with a spectral shift, Ω, with respect to each other. After high-pass spectral filtering the SFG interferogram is measured with a spectrometer (spec). The measured signal corresponds to [128]

$$S(\omega_\mathrm{c}) = |E_1(\omega_\mathrm{c})|^2 + |E_2(\omega_\mathrm{c}+\Omega)|^2 + 2\,|E_1(\omega_\mathrm{c})E_2(\omega_\mathrm{c}+\Omega)|\cos(\Delta\varphi)\,, \tag{2.76}$$

with

$$\Delta\varphi = \varphi(\omega_\mathrm{c}+\Omega) - \varphi(\omega_\mathrm{c}) + \omega_\mathrm{c}\tau. \tag{2.77}$$

The first two terms on the right-hand side of Eq. (2.76) correspond to the spectral densities of the individual replicas, E_1 and E_2, respectively. The third term contains the information about the spectral phase difference, $\varphi(\omega_\mathrm{c}+\Omega)-\varphi(\omega_\mathrm{c})$, between spectral components shifted by Ω. Because of the $\omega_\mathrm{c}\tau$ contribution in the cosine-term, the SPIDER-interferogram is modulated with a period of about τ^{-1}.

The phase-retrieval algorithm consists of a sequence of linear transformations [128]. First, the interferogram is FOURIER-transformed, yielding three distributions in the time-domain, corresponding to the three right-hand side terms in Eq. (2.76), and centered around $-\tau$, 0, and $+\tau$, respectively. Then, the contribution around $+\tau$ is selected by a spectral filter function. After applying the inverse FOURIER-transformation, only the third term is left, containing the phase difference and the $\omega_\mathrm{c}\tau$ contribution. Next, the $\omega_\mathrm{c}\tau$ contribution has to be removed from the cosine-argument. The delay, τ, can be determined by measuring the interferogram of the two replicas, E_1 and E_2, separately (with the chirped pulse blocked). Removing this term yields

$$\Delta\varphi - \omega_\mathrm{c}\tau = \varphi(\omega_\mathrm{c}+\Omega) - \varphi(\omega_\mathrm{c}), \tag{2.78}$$

the phase-difference between the frequency intervals separated by Ω, which is proportional to the group delay,

$$\Delta\varphi = \Omega\frac{\mathrm{d}\varphi}{\mathrm{d}\omega}. \tag{2.79}$$

The spectral phase is obtained by integration

$$\varphi(\omega) = -\frac{1}{\Omega}\int_0^{\omega}\Delta\varphi(\omega')\mathrm{d}\omega'. \tag{2.80}$$

Finally, the spectral and temporal pulse properties are fully characterized by separately measuring the fundamental pulse spectrum, $|E_1(\omega)|^2$. The temporal representation is obtained by FOURIER-transformation. According to the NYQUIST sampling limit, the pulse is reconstructed exactly if the spectral shear is smaller than $\Omega < 2\pi/\tau_N$, with τ_N being the temporal window over which the pulse has a non-zero finite energy. Also using the SPIDER technique, the phase-matching bandwidth of the non-linear crystal must be larger than the spectral bandwidth of the pulse to be characterized. Another common technique is the frequency-resolved optical gating (FROG). Using this technique, a two-dimensional spectrogram is recorded,

$$S(\omega,\Delta t) = \left|\int_{-\infty}^{+\infty} E(t)G(t-\Delta t)e^{-i\omega t}\mathrm{d}t\right|^2, \tag{2.81}$$

with a gating function, $G(t-\Delta t)$, provided by an ultrafast nonlinear process, mostly involving a second-order nonlinearity or a KERR-nonlinearity triggered by a replica of the pulse to be measured. As the measured spectrogram corresponds to a two-dimensional phase retrieval problem with an unambiguous solution, an iterative algorithm is applied. The experimental setup and the retrieval algorithm is described in detail in [129, 130].

Chapter 3

Single-shot pulse duration measurements at XUV and X-ray free-electron lasers

The performance of time-resolved experiments at XUV and X-ray free-electron lasers can be strongly improved by reliable characterization of the temporal FEL pulse properties. Knowledge of the temporal characteristics of laser pulses and FEL pulses is of crucial importance for most time-resolved experiments. Foremost, pulse-duration sensitive experiments, such as nonlinear light-matter interactions, require detailed knowledge about the FEL intensity envelope, $I_{\mathrm{FEL}}(t)$. But also for FEL scientists it is important to access temporal photon pulse properties in order to study the influence of machine parameters on the amplification process and to gain control over the FEL pulse properties. Time-resolved studies of ultrafast processes in pump-probe experiments using an optical pump and an XUV/X-ray probe pulse (or *vice versa*) are resolution-limited not only by the pulse durations, but also by pulse arrival time jitter.

SASE FELs suffer from pulse-to-pulse fluctuations. This affects also the temporal pulse properties. As explained in Section 1.3, SASE FEL pulses consist of multiple longitudinal modes, i.e. the temporal structure may feature a number of intensity maxima, depending on the number of modes. This number of modes as well as the individual mode intensity vary from shot to shot. If a pump-probe experiment is carried out using an optical laser pulse and an FEL pulse, also the synchronization between both pulses fluctuates statistically. This fluctuation of the time delay has various origins at an FEL, with its overall dimension of hundreds of meters. For example, the electron bunch arrival jitters due to the jitter of the radio-frequency drivers of the acceleration modules. The statistical SASE process itself introduces jitter, as well as the electronic synchronization between the optical master clock and the pump-probe laser. Optical path length drifts in the pump-probe amplifier and of the photon beam lines due to environmental changes (temperature, humidity, pressure) cause additional drift. At FLASH, the synchronization jitter at the experimental hall is typically about 100 fs [29–31] and can be reduced to sub-30 fs rms by optical synchronization or external seeding [32, 33].

Single-shot diagnostic methods are required to characterize the temporal structure and the arrival time of single FEL pulses. In this work, a technique for the FEL pulse duration and arrival time measurement [31, 45, 60–65] was developed further. The method provides high flexibility compared to other methods developed so far [40–44, 46–51] and offers the potential for high-resolution measurements of complex FEL pulse shapes for a broad range of wavelengths. Furthermore, promising measurements on ultra-thin samples show the capability for single-shot online measurements during an experiment.

3.1 Measuring the FEL pulse duration: an overview

Measuring the duration of ultrashort pulses in the XUV and X-ray regime is challenging. Direct optical correlation methods or phase-sensitive techniques that are common in the visible regime cannot be easily adapted. The availability of required optics and optical materials is limited and by far not comparable to the visible regime. Experiments in the XUV must be realized under vacuum conditions, due to the strong absorption cross-sections of air. Pulse duration measurements are thus a topic of active research and various direct [40–46] and indirect [47–51] methods exist. However, most of those experimental implementations are highly invasive and cannot be performed simultaneously with other pump-probe experiments.

The direct techniques are complex experiments on their own. For autocorrelation measurements [42, 43], multi-photon ionization of atomic transition levels in gaseous targets are used as nonlinear process. The correlation signal is measured by detecting the electron current with a time-of-flight spectrometer. The two pulse replicas are generated using specially designed split-and-delay optics. For cross-correlating XUV pulses with optical laser pulses the same method is applied [44, 52]. Owing to the discrete atomic transition levels, certain limitations exist concerning the photon energies and the range of measurable pulse durations. A further disadvantage is that these methods average over many pulses and are thus no single-pulse diagnostics.

A very promising single-pulse method is the light-field streaking [40, 41, 45, 53]. Photoelectrons are detected, generated by XUV/X-ray absorption of the single FEL pulse. The vector potential of a strong terahertz-field is used to accelerate the photoelectrons, which leads to a streaking of the measured time-of-flight spectra. The spectral broadening contains information about the intensity and the frequency chirp of the FEL pulse. However, generating strong terahertz field amplitudes requires either a dedicated terahertz undulator in the FEL beamline [54, 55] or an external source, based on parametric conversion of an optical laser pulse [56, 57].

3.2 Single-shot cross-correlator

Several methods exist for the arrival time measurement. One category of diagnostics is designed only to measure the arrival time of the electron bunches with respect to the pump-probe laser [131–133]. But in this case, the jitter within the optical beamlines is omitted, because the spatial distance between the undulator section and actual experiment is too large. Another category of diagnostics is to directly measure the timing of the XUV pulses at the experimental station [31, 45, 58, 60–65, 134]. In this work, the concept of a temporal diagnostic, based on a solid-state cross-correlation [31, 45, 60–65], is further developed. The method was first tested at FLASH using GaAs targets for single-shot arrival time measurements and for determining an upper limit for the FEL pulse duration [31, 58, 60]. The novelty of this work is to show the possibility to extract the FEL intensity envelope and thus the actual pulse duration. The measurements were performed using fused silica glass and Si_3N_4 samples. A corresponding theoretical model of the ionization process is presented, supported by a numerical Monte-Carlo model. It is shown that the measured signal is similar to an optical-to-XUV cross-correlation in the sense that a signal related to the FEL intensity envelope is sampled with an ultrashort optical probe pulse. The method works for a wide range of XUV and X-ray wavelengths and for pulse durations ranging from few femtoseconds to hundreds of femtoseconds. The experiment was carried out at the XUV free-electron laser FLASH.

The experimental setup is shown in Fig. 3.1a. The spatial encoding principle is shown in

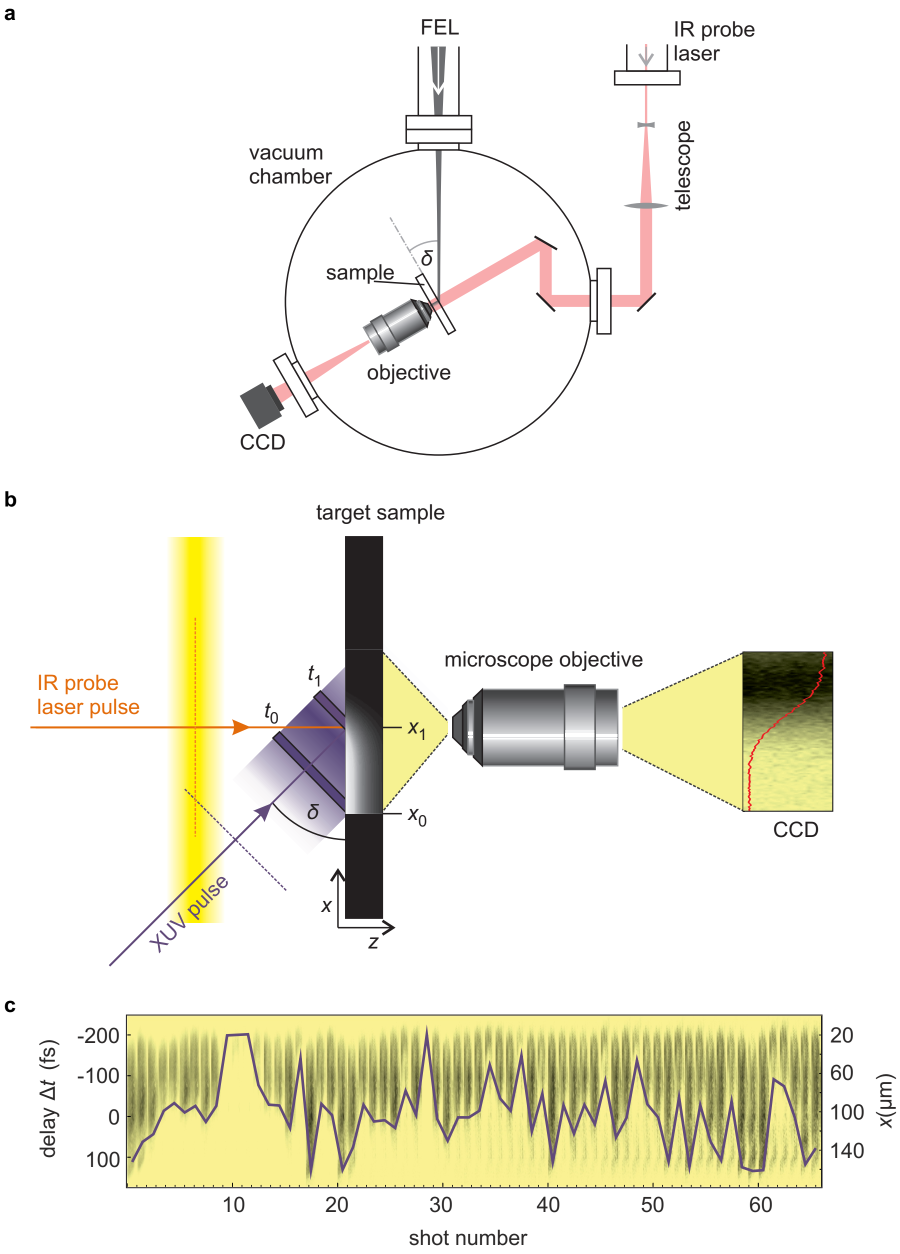

Figure 3.1 Setup and principle of the single-shot cross-correlator. (**a**) Schematic experimental setup. The sample (fused silica, Si$_3$N$_4$, mounted on a motorized 3-dimensional translation stage) is placed in the focus of the FEL beam, which is incident under the angle δ with respect to the sample surface. The FEL intensity is about $I_{\mathrm{FEL}} = 10^{12}\mathrm{Wcm}^{-2}$. The near-infrared probe laser is largely collimated and illuminates the interaction area of FEL and sample surface homogeneously and with low intensity under normal incidence. The sample surface is imaged on a CCD using a microscope objective. (**b**) Principle of the spatial encoding setup. Different transverse positions on the sample, x_0 and x_1, are mapped to different points in time, t_0 and t_1, respectively. The sample is originally transparent for the near-infrared probe laser, but becomes opaque after ionization with the XUV pulse. This change of transparency is probed by the near-infrared laser pulse under normal incidence, propagating along z. The transmitted intensity is imaged onto a camera (CCD). (**c**) Series of 68 single-shot measurements. The the decrease in optical transmission (grey shading) along transversal axis, x, is due to the XUV absorption. The turning point of the absorption occurs at a different position in each shot, depending on the temporal delay, Δt, between the FEL pulse and the near-infrared pulse.

Fig. 3.1b. The FEL XUV pulse is focused on the sample (fused silica glass or Si_3N_4) under a shallow angle, δ, with respect to the sample surface. The FEL intensity is about $I_{FEL} = 10^{12}\mathrm{Wcm}^{-2}$. Due to absorption and photoionization caused by the FEL at the sample surface, the sample transmission is changed. The interaction geometry with the shallow angle projects the absorption of the FEL pulse at different moments in time to different transverse positions on the sample surface. Therefore, the different positions, x_0 and x_1, are mapped to corresponding points in time, t_0 and t_1. The spatio-temporal mapping, $t \mapsto x$, is defined by

$$t = \frac{x}{c_0}\cos(\delta), \tag{3.1}$$

where c_0 is the vacuum speed of light. The observable temporal window, ΔT and the temporal resolution, δt depend on the angle δ and the FEL beam diameter, d_x,

$$\Delta T = \frac{d_\mathrm{x}}{c_0 \tan(\delta)}. \tag{3.2}$$

For example, with an FEL beam diameter of $d_\mathrm{x} = 100\,\mu\mathrm{m}$, the temporal window is 1.3 ps at $\delta = 14.2°$ and 334 fs at $\delta = 45°$.

The temporal resolution, δt, depends on the imaged spatial resolution, δx, according to Eq. (3.1). The sample surface is imaged by a microscope objective[1] onto a progressive scan charge-coupled device camera[2]. The imaging resolution was calibrated using a periodic micrometer mask[3], yielding $\delta x = 3\,\mu\mathrm{m}$. According to Eq. (3.1), the temporal resolution given by the imaging resolution is $\delta t = 10\,\mathrm{fs}$ at $\delta = 14.2°$ and $\delta t = 7\,\mathrm{fs}$ at $\delta = 45°$.

The FEL penetrates the sample surface and causes photoionization. Hence, a high density of energetic free-electrons evolves during the FEL irradiation. The free-electron plasma changes the refractive index for visible frequencies (as explained in Section 2.5.5), changing the sample transmission. This transmission change is probed with an ultrashort optical laser pulse under normal incidence. It is largely collimated (a few millimeters FWHM) to achieve a homogeneous illumination of the ionized region. The laser intensity is must be only sufficient to illuminate the CCD. Because of the spatio-temporal encoding, both, the spatial near-field beam profile of the probe laser and the FEL focus, should be as homogeneous as possible, ideally top-hat, to reduce spatial features. The background correction is described in Section 3.4.1.

The optical pulse will be partly reflected and absorbed, depending on the electron density, $n_\mathrm{e}(t)$, causing a shading of the transmitted light imaged onto the CCD. At FLASH, the pump-probe Ti:sapphire amplifier was used for the experiments (Coherent Hidra), which operates at 10 Hz repetition rate. The pulse duration was measured with a single-shot second-order autocorrelator (Coherent SSA), yielding $\tau_\mathrm{L} = (64 \pm 7)\,\mathrm{fs}$ at the central wavelength of $\lambda_\mathrm{L} = 800\,\mathrm{nm}$. The measured signal after transmission is given by the cross-correlation,

$$S(\Delta t) = \int_{-\infty}^{+\infty} G(t) I_\mathrm{L}(t - \Delta t)\mathrm{d}t. \tag{3.3}$$

where $G(t) \in (0, 1)$ represents the optical transmission function (transmission of the free-electron plasma), $I_\mathrm{L}(t)$ is the intensity envelope of the probe laser pulse, and Δt is the temporal delay between the FEL and the optical laser pulse. With the spatio-temporal encoding setup, Δt is

---

[1] Mitutoyo M Plan APO NIR, numerical aperture $NA = 0.5$

[2] CCD, Basler A311f, 659 × 494 pixels

[3] 18 line-space cycles per millimeter

mapped to the spatial x-axis, allowing for single-shot measurements. Using a sufficiently short optical probe pulse, the transmission function can be obtained via a deconvolution. The evolution of the optical transmission contains information about the temporal evolution of the FEL intensity, $G(t) = G\left[I_{\mathrm{FEL}}(t)\right]$. To extract this information, a detailed study of the photoionization dynamics and its influence on the optical properties was performed, as presented in sections 3.3.1 and 3.3.

The temporal delay, Δt, is directly obtained from the raw measurements for each shot. As an example, in Fig. 3.1c a series of 68 single shots is shown, measured on fused silica. Here, the grey shading indicates the transition from full transmission (yellow) to opacity (grey shaded). The transversal sample position, x, where this transition occurs, represents the time delay, Δt, and can be defined by a transmission threshold. In the presented measurements, the threshold was 20% of the total transmission change, to be clearly distinguished from noise. An error function fitting procedure can also be used [65]. In Fig. 3.1c, some measurement points are out of the temporal window (for example, shot number 10), because the temporal window was only about 330 fs, at the angle $\delta = 45°$ and about 100 µm FEL beam diameter. The application of this solid-state cross-correlation method for arrival time measurements was throughout investigated in several works [31, 45, 60–65]. For example, a resolution improvement to sub-10 fs was attained during an optical/X-ray pump-probe experiment using a similar technique (see also Introduction, Section 1.2) [65]. Because this has been thoroughly investigated, the present work is focused on simultaneous duration measurements.

3.3 Physical model and data evaluation

A comprehensive theoretical model was developed to evaluate the measured cross-correlations, $S(\Delta t)$. In order to understand the relation between the transmission function, $G(t)$, and the FEL intensity envelope, $I_{\mathrm{FEL}}(t)$, first, the relation between FEL absorption and free-electron density was studied using a dedicated Monte-Carlo simulation. In a next step, the plasma refractive index was calculated to model the optical transmission due to reflection and absorption of the optical probe pulse. Finally, theoretical cross-correlations for given FEL and optical laser parameters could be fitted to the experimental data.

3.3.1 Monte-Carlo simulation

A dedicated Monte-Carlo simulation (see Section 2.5.2) was performed by N. MEDVEDEV from the Center for Free-Electron Laser Science (CFEL) in order to study the ionization dynamics within fused silica. The increase of the electron density was simulated during the irradiation with an XUV pulse with 80 fs FWHM pulse duration and at different pulse energies and wavelengths. The result at $\lambda_{\mathrm{FEL}} = 5.5\,\mathrm{nm}$ (photon energy 214.2 eV) is presented in Fig. 3.2a. The intensity is about $I_{\mathrm{FEL}} = 2.45 \cdot 10^{12}\,\mathrm{Wcm}^{-2}$, corresponding to a fluence of $F = 0.21\,\mathrm{Jcm}^{-2}$. The electron density, $n_{\mathrm{e}}(t)$, increases proportionally with the integrated intensity, reaching a final density of $5 \cdot 10^{21}\,\mathrm{cm}^{-3}$. The simulation was also performed at $\lambda_{\mathrm{FEL}} = 13.6\,\mathrm{nm}$ and $\lambda_{\mathrm{FEL}} = 41\,\mathrm{nm}$. In Fig. 3.2b, the electron density, n_{e}, is plotted in dependence on the fluence (the integrated intensity) the different simulated FEL wavelengths and pulse energies: $\lambda_{\mathrm{FEL}} = 5.5\,\mathrm{nm}$ (214.2 eV), $E_{\mathrm{FEL}} = 20\,\mu\mathrm{J}$, $F = 0.21\,\mathrm{Jcm}^{-2}$ (black); $\lambda_{\mathrm{FEL}} = 13.6\,\mathrm{nm}$ (86.6 eV), $E_{\mathrm{FEL}} = 6\,\mu\mathrm{J}$, $F = 0.048\,\mathrm{Jcm}^{-2}$ (dashed blue); $\lambda_{\mathrm{FEL}} = 41\,\mathrm{nm}$ (28 eV), $E_{\mathrm{FEL}} = 40\,\mu\mathrm{J}$, $F = 0.12\,\mathrm{Jcm}^{-2}$ (red). The gray shaded area represents the experimental conditions. As a very important conclusion, linear absorption can be assumed for fluences smaller than $F < 0.05\,\mathrm{Jcm}^{-2}$. At 41 nm, the electron density starts to increase nonlinearly for $F > 0.1\,\mathrm{Jcm}^{-2}$. Nonlinear effects arise from PAULI's principle and the photoabsorption of excited electrons (see Section 2.5.2).

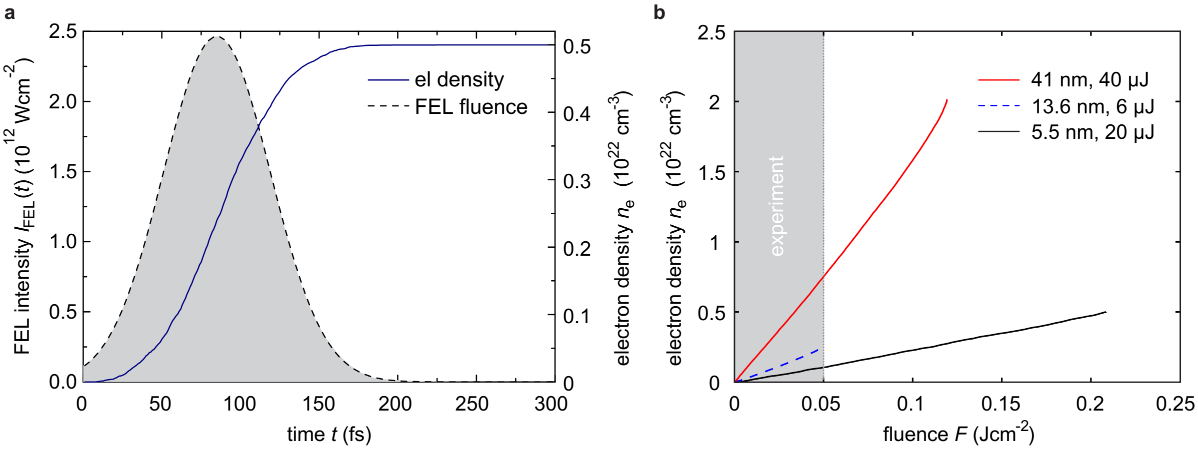

Figure 3.2 Monte-Carlo simulation of the free-electron density, $n_e(t)$, generated by photoionization within fused silica during the irradiation with an ultrashort XUV pulse. (**a**) Temporal evolution of an 80 fs FEL pulse at 5.5 nm (grey shaded) and corresponding electron density (blue line). The electron density is proportional to the integrated FEL pulse. (**b**) Dependence of the electron density on the FEL fluence for different wavelengths: $\lambda_{\mathrm{FEL}} = 5.5\,\mathrm{nm}$, $E_{\mathrm{FEL}} = 20\,\mu\mathrm{J}$ (black); $\lambda_{\mathrm{FEL}} = 13.6\,\mathrm{nm}$, $E_{\mathrm{FEL}} = 6\,\mu\mathrm{J}$ (blue dashed); $\lambda_{\mathrm{FEL}} = 41\,\mathrm{nm}$, $E_{\mathrm{FEL}} = 40\,\mu\mathrm{J}$ (red). The gray shaded area represents the experimentally used FEL pulse fluences $F < 0.05\,\mathrm{Jcm}^{-2}$ where linear absorption can be assumed. Simulation performed by N. MEDVEDEV (CFEL). Published in [2].

3.3.2 Calculation of electron density

According to the findings in section 3.3.1, the electron density grows linearly with the absorbed FEL photon flux,

$$\Phi_{\mathrm{ph}} = \frac{F}{\hbar\omega_{\mathrm{FEL}}}. \tag{3.4}$$

This allows to find an analytical expression to obtain the electron density as a function of the FEL intensity. With a given absorption coefficient, α_{FEL}, the FEL penetrates the sample material by the penetration depth $1/\alpha_{\mathrm{FEL}}$ along the z-axis and absorption takes place according to the BEER-LAMBERT law:

$$I_{\mathrm{FEL}}(t,z) = I_{\mathrm{FEL}}(t) \cdot e^{-\alpha_{\mathrm{FEL}} \cdot z}. \tag{3.5}$$

So, for each point on the time axis, t' (sample x-axis), a certain amount of photons is absorbed. The photon flux within the material is obtained by temporal integration over the pulse,

$$\begin{aligned} \Phi_{\mathrm{ph}}(t,z) &= \frac{1}{\hbar\omega_{\mathrm{FEL}}} \int_{t_0}^{t} I_{\mathrm{FEL}}(t',z)\mathrm{d}t' \\ &= \Phi_{\mathrm{ph}}(t) \cdot e^{-\alpha_{\mathrm{FEL}} \cdot z}. \end{aligned} \tag{3.6}$$

The initial flux is zero, $\Phi_{\mathrm{ph}}(t_0) = 0$. Using Eq. (2.58), the obtained photon distribution within the sample is used to calculate the electron density caused by photoionization:

$$\begin{aligned} n_{\mathrm{e}}(t,z) &= \frac{\hbar\omega_{\mathrm{FEL}}}{E_{\mathrm{eg}}} \left| \frac{\partial \Phi_{\mathrm{ph}}(t,z)}{\partial z} \right| \\ &= \frac{\hbar\omega_{\mathrm{FEL}}}{E_{\mathrm{eg}}} \Phi_{\mathrm{ph}}(t) \cdot \alpha_{\mathrm{FEL}} e^{-\alpha_{\mathrm{FEL}} \cdot z} \end{aligned} \tag{3.7}$$

According to Eq. (3.7), it is assumed that the electron density instantaneously follows the integrated FEL intensity envelope. According to the findings in Section 2.5.4, this assumption is valid for the photon energies used in the experiment ($<$ 1 keV). In Fig. 3.3 the two-dimensional electron distribution, $n_{\mathrm{e}}(t,z)$, is plotted, calculated according to Eq. (3.7) for the irradiation of fused silica with a 50 fs GAUSSIAN FEL pulse at 5.5 nm wavelength. For each point in time, an exponentially decaying electron density profile is obtained. The thickness of this plasma layer is obtained from the penetration depth of the FEL, $1/\alpha_{\mathrm{FEL}} = 144\,\mathrm{nm}$.

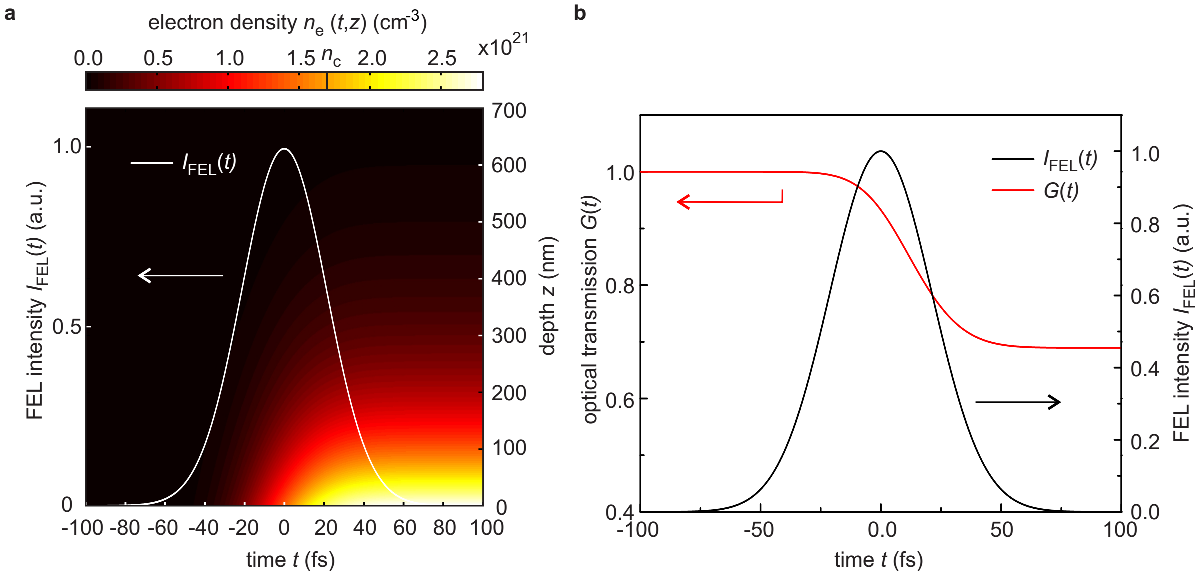

Figure 3.3 Simulation of the transmission function, $G(t)$. (**a**) Two-dimensional electron density profile, $n_{\mathrm{e}}(t,z)$, during the irradiation with a 5.5 nm FEL pulse, represented by its intensity envelope, $I_{\mathrm{FEL}}(t)$ (white line). The critical electron density for an optical probe laser with $\lambda_{\mathrm{L}} = 800\,\mathrm{nm}$ is $n_{\mathrm{c}} = 1.7 \cdot 10^{21}\,\mathrm{cm}^{-3}$. The z-axis denotes the propagation axis of the optical laser and the penetration depth of the FEL. (**b**) Transmission function $G(t)$ (red line) for an optical laser calculated from the electron density in (a). The FEL intensity is also shown (black line).

3.3.3 Optical transmission function

An optical laser probing the transmission of this sample will be partly reflected and absorbed. The sample transmission depends on the evolution of the FEL pulse on the time axis. For $t < 0\,\mathrm{fs}$, the transmission is high, owing to a low electron density. For $t > 0$, the transmission is low, owing to a high electron density. The resulting time-dependent transmission function, $G(t)$, is obtained by calculating the optical properties of the free-electrons. The time axis and the propagation axis are discretized in finite steps, t_m and z_j. For each step, the complex refractive index, $\tilde{n}(t_m, z_j) = \sqrt{\varepsilon(t_m, z_j)}$, is calculated from the corresponding electron density (Eq. 2.70),

$$n^2(t_m, z_j) = 1 - \frac{n_e(t_m, z_j)}{n_c}\left(\frac{1}{1 + f(t_m, z_j)^2} + i\frac{f(t_m, z_j)}{1 + f(t_m, z_j)^2}\right). \tag{3.8}$$

For the single time-steps, the transmission of the optical laser is calculated using the transfer-matrix method [135, 136]. The refractive index gradient is approximated by a sequence of thin layers of thickness $z_{(j+1)} - z_j = 1\,\mathrm{nm}$. Taking into account the FRESNEL reflection, transmission, absorption and interference effects between each z_j and $z_{(j-1)}$, the propagation of the optical prope pulse is described by the transfer matrix, $\tilde{M} = \prod_j \tilde{M}_j$. Here, $\tilde{M}_j$ is the transfer matrix of a single thin layer. The procedure is explained in detail in Appendix B. At each time step, the plasma transmission function, $G(t)$, is obtained, as shown in Fig. 3.3. When the probe pulse arrives earlier than the FEL pulse, i.e. when no free-electrons are present, the transmission function is $G(t \ll 0) = 1$. That means that all light from the optical probe pulse is transmitted. The constant reflection at the sample surfaces is neglected. Correspondingly, in that case we normalize the cross-correlation to $S(\Delta t \ll 0) = 1$. When the probe pulse arrives a few picoseconds after the FEL pulse, it will be partially reflected and absorbed due to the optical properties of the free-electron plasma. The signal will remain on a constant level, $S(\Delta t \gg 0) = \text{const.} < 1$. During the experiments, this constant transmission remained unchanged for a few picoseconds. The plasma can therefore be assumed to be stable. The actual cross-correlation measurement is obtained when both pulses overlap within the temporal window. In that case, the signal undergoes a transition from $S(\Delta t < 0) = 1$ to $S(\Delta t > 0) = \text{const.} < 1$.

3.3.4 Fitting algorithm

A *start-to-end* simulation was developed using the numerical procedure described in Section 3.3 to retrieve the FEL pulse structure from a measured cross-correlation. A schematic chart of the model is displayed in Fig. 3.4. First, an FEL pulse is defined by wavelength, pulse energy, beam size and intensity envelope, $I_{\mathrm{FEL}}(t)$. Second, the electron density profile, $n_e(t, z)$, is calculated according to Eq. (3.7). From the electron density, the refractive index profile, $n(t, z)$, is calculated according to Eq. (3.8). Third, using the transfer matrix method, the optical transmission function, $G(t)$, is obtained for the particular FEL pulse shape. Fourth, the transmission function,$G(t)$, is cross-correlated with the optical laser, $I_L(t)$, according to Eq. (3.3). The calculated cross-correlation, $S_1(\Delta t)$, is fitted to the measured data, $S(\Delta t)$, by optimizing the least-square residual error,

$$[\Delta f(\Delta t)]^2 = [S_1(\Delta t) - S(\Delta t)]^2, \tag{3.9}$$

using a trust-region-reflective algorithm [137]. The fitting parameters are given by the FEL pulse parameters mentioned above. For evaluating the experimental data, a GAUSSIAN FEL pulse is assumed, because the probe pulse duration is too long to resolve detailed pulse structure. The GAUSSIAN pulse represents the temporal distribution obtained by averaging over many pulses that consist of multiple longitudinal SASE modes [41, 47]. Hence, the FWHM pulse duration, τ_{FEL}, is the main fitting parameter to be optimized.

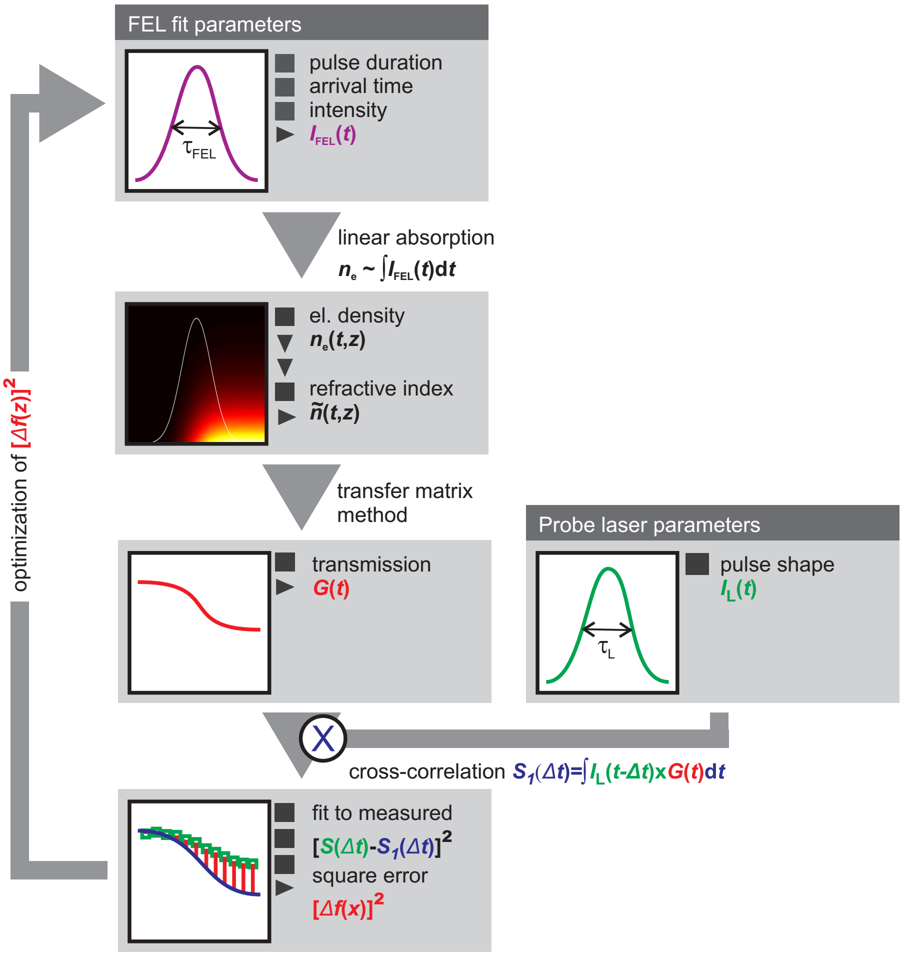

Figure 3.4 Simulation algorithm. Initially, an FEL pulse intensity profile, $I_{\mathrm{FEL}}(t)$, is defined with proper variable parameters. This pulse is used to calculate the electron density, $n_{\mathrm{e}}(t,z)$, and the refractive index, $\tilde{n}(t,z)$, within the sample. The plasma transmission function, $G(t)$, is calculated using the transfer matrix method. This function is cross-correlated with the intensity of the optical laser, I_{L}. The resulting cross-correlation, $S_1(\Delta t)$, is fitted to the measured signal, $S(\Delta t)$, by optimizing the square error, $[\Delta f(x)]^2$, with varying FEL pulse parameters. For the measurements in this work, the FEL pulse was defined as a GAUSSIAN pulse and the fitting parameters were the pulse duration, the pulse energy and the beam diameter.

3.4 Single-shot measurements

In the following, the data processing is explained, i.e. the extraction of the cross-correlation signal from the raw measurement (see Fig. 3.5). Afterwards, single-shot pulse duration measurements are presented. For the optical laser, a GAUSSIAN intensity envelope was assumed. Its pulse duration of $\tau_\mathrm{L} = (64 \pm 7)\,\mathrm{fs}$ was measured using an intensity autocorrelator (Coherent SSA).

3.4.1 Data processing

First, the CCD images are corrected for the probe-laser background (without FEL pulse). Second, the correlation images are corrected for the FEL spatial profile. To this end, a reference image is acquired with the FEL pulse arriving significantly earlier than the probe pulse. The reference image is shown in Fig. 3.5a with inverted colors. Black color corresponds to full optical transmission, yellow corresponds to optical opacity. The opacity distribution is the footprint of the spatial FEL beam profile, representing the stable free-electron density after ionization. Third, the actual images that contain the correlation are acquired at temporal overlap of the FEL and the optical pulse. An example of a correlation signal is shown in Fig. 3.5b. There is a smooth transition between full transmission (black) and opacity (color bar). Before the reference is subtracted from the image, a region of interest (ROI) is chosen, indicated by the grey boxes in Figs. 3.5a and b. By integration over the vertical axis, y, lineouts are calculated, as shown in Fig. 3.5c for the reference (lineout A, grey) and the signal (lineout B, light red). The cross-correlation is extracted by normalization:

$$S(\Delta t) = 1 - \frac{1-B}{1-A} \cdot [1 - \min(B)]\,, \tag{3.10}$$

with the factor $(1-\min(B))$ accounting for the constant transmission level after the FEL pulse. The final cross-correlation is also shown in Fig. 3.5c (red line, blue rectangles). Due to pointing jitter of the FEL on the sample, a spatial alignment of the cross-correlation image with respect to the reference image might be required.

The ultrafast relaxation of the electron density within 150 fs, which has been reported in other studies using fused silica [119, 120], could not be observed. In the present experiments, the transmission remained at a constant level even for a delay of a few picoseconds. In previous works, the relaxation was associated with the formation of self-trapped excitons, leading to a rapid capture of free carriers [138]. In the present work, the photoionization was triggered by linear absorption of an intense XUV pulse. According to the theoretical calculations, the electron density was up to two orders of magnitudes higher compared to the other experiments. Hence, it is postulated that, under the experimental conditions in the present work, a breaking of excitons occurred due to collisions with high energetic electrons within the conduction band [2]. The interpretation is supported by other studies, where it has been shown that excitons, which were formed by low fluence XUV radiation, can be destroyed by multiphoton absorption of a optical pulse [139].

3.4.2 Target material: fused silica

The first measurements were performed using a 1 mm thick fused silica slide as target. The FEL was operated at two distinct wavelengths, λ_FEL. The first measurements were carried

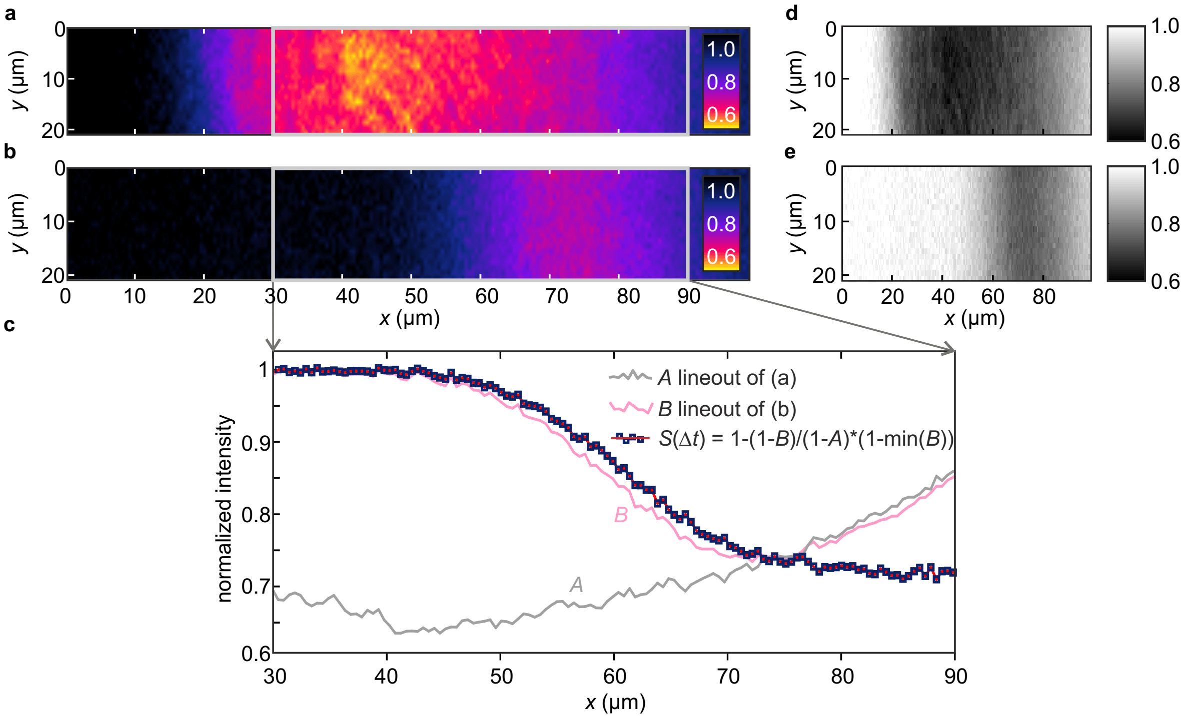

Figure 3.5 Cross-correlation measurement, $S(\Delta t)$. (**a**) and (**b**) CCD images of the probe laser transmission along the transverse coordinate x on the sample for different delays between probe pulse and FEL pulse (notice: inverse color scale). In the top image (a), the probe pulse arrived a few picoseconds after the FEL. Because the plasma was fully evolved and stable within this temporal window, the measurement was used as reference to correct for the spatial FEL profile. In the signal image (b), both pulses arrived simultaneously. Resultingly, the transient change of transmitted intensity during the absorption of the FEL pulse was measured. (**c**) Reconstruction of the cross-correlation $S(\Delta t)$. Within the region of interest (grey boxes in (a) and (b)), lineouts were calculated for the reference (A, red line) and the signal (B, grey line) by integration over the vertical axis, y. The cross-correlation was obtained by inverting the signal lineout by $1-B$ and normalizing it with respect to $1-A$. The multiplication with $1-\min(B)$ accounted for the constant transmission level after the transient edge, which was $\min(B) = 0.7$ in the present case. Published in [2]. (**d**) Reference image in linear greyscale (white: full optical transmission, black: 60% optical transmission). (**e**) Signal image in linear greyscale.

out at $\lambda_{\mathrm{FEL}} = 41.5\,\mathrm{nm}$, the second measurements were carried out at $\lambda_{\mathrm{FEL}} = 5.5\,\mathrm{nm}$. For all measurements, the free-electron laser was operated in a 10 Hz single-pulse mode. The FEL pulse energy was measured with the gas-monitor detector (GMD [140]).

At the FEL wavelength of $\lambda_{\mathrm{FEL}} = 41.5\,\mathrm{nm}$, the electron bunch charge was $Q = 0.5\,\mathrm{nC}$ and the average pulse energy was $E_{\mathrm{FEL}} = (84 \pm 4)\,\mu\mathrm{J}$. The fluence was about $F \approx 0.05\,\mathrm{Jcm}^{-2}$. The FEL was incident with an angle $\delta = 45°$, with respect to the sample surface. A single-shot measurement is presented in Fig. 3.6a (white rectangles). The fitted cross-correlation (blue line) is obtained by optimizing the pulse duration of a GAUSSIAN pulse in the start-to-end simulation (see Section 3.3.4). In this case, the pulse duration is $\tau_{\mathrm{FEL}} = (184 \pm 14)\,\mathrm{fs}$ FWHM. The data scattering originated from FEL pulse energy and beam profile fluctuations between the reference image acquisition and the actual measurement.

At the FEL wavelength of $\lambda_{\mathrm{FEL}} = 5.5\,\mathrm{nm}$, the electron bunch charge was $Q = 0.25\,\mathrm{nC}$ and the average pulse energy was $E_{\mathrm{FEL}} >= (29 \pm 10)\,\mu\mathrm{J}$. The fluence was about $F \approx 0.05\,\mathrm{Jcm}^{-2}$. Because of a smaller beam diameter, the FEL was incident with an angle $\delta = 14.2°$, with respect to the sample surface. A single-shot cross-correlation measurement is displayed in in Fig. 3.6b (white rectangles). The fitted cross-correlation (blue line) corresponds to a GAUSSIAN pulse with $\tau_{\mathrm{FEL}} = (21 \pm 19)\,\mathrm{fs}$. Here, the uncertainty was mainly determined by the long pulse duration of the optical probe laser (see error analysis in Sec. 3.5). Due to the strong absorption of the XUV photons within the target (see Fig. 2.8, p. 32) the total FEL pulse energy was deposited. Consequently, changes in the surface morphology were observed after a few tens of pulses. For online pulse duration measurements, fused silica samples should be placed behind an experiment to simultaneously measure the pulse duration. Furthermore, they should be moved to a new position after a few shots.

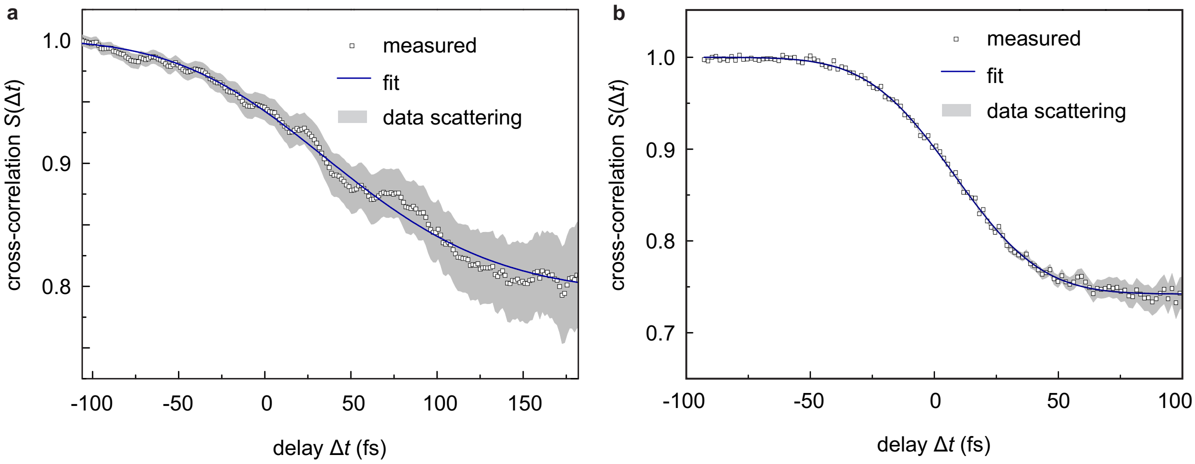

Figure 3.6 Single-shot cross-correlations using fused silica samples. Measured (white rectangles) and fitted (blue line) curves are shown. (**a**) FEL wavelength of 41.5 nm, bunch charge of 0.5 nC. The resulting pulse duration is $\tau_{\mathrm{FEL}} = (184 \pm 14)\,\mathrm{fs}$. (**b**) FEL wavelength of 5.5 nm, bunch charge of 0.25 nC. The resulting pulse duration is $\tau_{\mathrm{FEL}} = (21 \pm 19)\,\mathrm{fs}$. The grey data scattering originates from the FEL beam profile correction (see text). Published in [2].

3.4.3 Target material: silicon nitride membrane

To overcome the limitations of the fused silica samples, ultra-thin silicon nitride (Si_3N_4) membranes were tested[4]. The FEL was tuned to similar parameters, $\lambda_{\mathrm{FEL}} = 5.5\,\mathrm{nm}$, $Q = 0.25\,\mathrm{nC}$ and $E_{\mathrm{FEL}} = 2.5\,\mu\mathrm{J}$. The fluence was about $F < 0.01\,\mathrm{Jcm}^{-2}$. The pulse energy was adjusted using the gas attenuator, which is installed at the photon beamline at FLASH. In Fig. 3.7, a measured single-shot cross-correlation is shown (white rectangles). The fitted curve (blue line) corresponds to a GAUSSIAN pulse with $\tau_{\mathrm{FEL}} = (34 \pm 19)\,\mathrm{fs}$, which is well within the error bars compared to the measurement on fused silica. As the energy deposition was lower within the Si_3N_4 sample, as compared to the fused silica sample, the measurements were non-destructive. No change of the membrane morphology was observed, even after a few thousand absorbed pulses. At the sample thickness of 20 nm and the angle $\delta = 14.2°$, the optical path of the FEL through the membrane is only 98 nm. Hence, the absorption interaction length is considerably reduced. For short wavelengths the calculated XUV transmission through the membrane is about 15% at 20 nm, 45% at 13 nm 8% at 10 nm and 29% at 5.5 nm. The residually transmitted FEL pulse can be reused for a simultaneous XUV/optical pump-probe experiment.

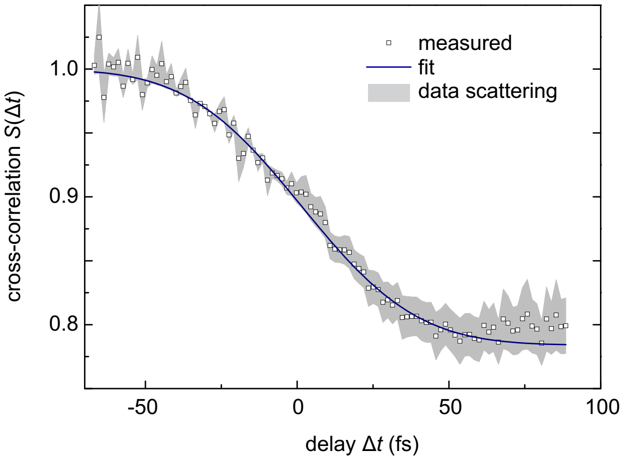

Figure 3.7 Single-shot cross-correlation using the Si_3N_4 membrane. The measured (white rectangles) and fitted (blue line) curves are shown at an FEL wavelength of 5.5 nm, and a bunch charge of 0.25 nC. The resulting pulse duration is $\tau_{\mathrm{FEL}} = (34 \pm 19)\,\mathrm{fs}$ (see Section 3.5 for error analysis). The grey data scattering originates from fluctuations of the FEL beam profile. Published in [2].

3.4.4 Discussion on the measured pulse duration

The measured FEL pulse durations are in agreement with theoretical estimations [141]. With the electron bunch charges used in the experiment, typical pulse durations are 140–200 fs for SASE pulses lasing at $\lambda_{\mathrm{FEL}} = 41.5\,\mathrm{nm}$. Pulse durations at $\lambda_{\mathrm{FEL}} = 5.5\,\mathrm{nm}$ are considerably shorter than 100 fs, but corresponding measurements are not published so far. The correlation between bunch charge and FEL pulse duration is derived from techniques developed earlier, for example, XUV autocorrelation [42, 43], XUV/optical cross-correlation [44, 52], spectral measurements and statistical methods [47–51, 141], light field streaking [40, 41, 45, 53]. These complex techniques were not available on demand for a direct comparison.

---

[4] sample dimensions $200 \times 200 \times 0.02\,\mu\mathrm{m}^3$.

3.5 Error analysis

3.5.1 Resolution and sensitivity

The temporal resolution is ultimately limited by the spatial imaging resolution and the probe laser pulse duration. The imaging resolution is $\delta t = 7\,\mathrm{fs}$ at 45° and $\delta t = 10\,\mathrm{fs}$ at 14.2° using a applied microscope objective with $NA = 0.5$ (see Section 3.2). The overall error of the measurement was evaluated by error propagation,

$$\delta t = \sqrt{\Delta t|_{\mathrm{L}}^2 + \Delta t|_{\mathrm{data}}^2}. \tag{3.11}$$

The error of the laser pulse duration is $\delta\tau_{\mathrm{L}} = \pm 7\,\mathrm{fs}$. This error stems from the resolution of the autocorrelator device (8 fs per pixel) and from the autocorrelation ambiguities due to uncompensated 3^{rd}- and 4^{th}- order dispersion from the grating compressor. The error propagation, $\Delta t|_{\mathrm{L}}$, is obtained by varying $\tau_{\mathrm{L}} \pm \delta\tau_{\mathrm{L}}$ in the correlation integral (Eq. 3.3). This results in $\Delta t|_{\mathrm{L}} = \pm 7\,\mathrm{fs}$ at $\lambda_{\mathrm{FEL}} = 41.5\,\mathrm{nm}$ and $\Delta t|_{\mathrm{L}} = \pm 16\,\mathrm{fs}$ at $\lambda_{\mathrm{FEL}} = 5.5\,\mathrm{nm}$. For the presented measurements, further error contributions arise from spatial fluctuations of the data points (including imaging resolution) and the assumptions in the start-to-end simulation. The latter includes also the model sensitivity on physical parameters, such as the electron-ion coupling factor, f, and variations of the real electron density distribution, $n_{\mathrm{e}}(t,y)$. For example, the algorithm was also carried out for a rectangular electron density distribution. The deviations are estimated to $\Delta t|_{\mathrm{data}} = \pm 12\,\mathrm{fs}$ at $\lambda_{\mathrm{FEL}} = 41.5\,\mathrm{nm}$ and $\Delta t|_{\mathrm{data}} = \pm 10\,\mathrm{fs}$ at $\lambda_{\mathrm{FEL}} = 5.5\,\mathrm{nm}$. In summary, the overall error was $\delta t = \pm 14\,\mathrm{fs}$ at 41.5 nm and $\delta t = \pm 19\,\mathrm{fs}$ at 5.5 nm.

3.5.2 Pointing jitter

The influence of the FEL pointing jitter on the time axis can be neglected for two reasons: First, for pulse duration measurements the images are spatially aligned with respect to a reference measurement to achieve the FEL beam profile correction. Second, the angular deviation of the wavefront is very small. This point becomes clear when we estimate for example the change of the optical path along a $l = 10\,\mathrm{m}$ beamline for a pointing jitter of 100 µm (which is an overestimation). The angular deviation would be $\Theta = \mathrm{atan}(100\,\mu\mathrm{m}/10\,\mathrm{m}) = 10\,\mu\mathrm{rad}$. This results in a path length deviation of

$$\Delta l = 100\,\mu\mathrm{m} \cdot \sin(10\,\mu\mathrm{rad}) = 100\,\mathrm{nm}, \tag{3.12}$$

corresponding to a temporal deviation of $\delta t|_{\Theta} = 0.33\,\mathrm{fs}$.

3.6 Perspectives: reaching the few-fs resolution

In this section, the experimental limits on the temporal resolution of the pulse duration measurement are investigated. The physical limitation is given by the response time of the electronic subsystem during the femtosecond FEL irradiation. In Section 2.5.4, it was concluded that for photon energies lower than 1 keV the response time is in the few-fs regime. Experimentally, the imaging resolution and the laser pulse duration are the main limiting factors.

3.6.1 Imaging resolution

Because of the spatio-temporal encoding, the optical imaging resolution of the sample surface is a crucial factor. Microscopic setups can be used to achieve almost diffraction-limited imaging. For example, with a numerical aperture of $NA = 0.8$ and a laser wavelength of $\lambda_{\mathrm{L}} = 500\,\mathrm{nm}$, an imaging resolution of

$$\delta x = 0.61 \frac{\lambda_{\mathrm{L}}}{NA} = 381\,\mathrm{nm} \tag{3.13}$$

can be attained. According to Eq. (3.1), and an angle of $\delta = 45°$, this corresponds to $\delta t < 1\,\mathrm{fs}$.

3.6.2 Dispersive effect on shortest probe pulses

According to Eq. (3.3), a probe pulse in form of a DIRAC-delta function would directly return the optical transmission function from the measurement. Hence, the probe pulse duration should be as short as possible for a high resolution measurement. Experimentally, an optical pulse duration of 4 fs can be achieved, for example by spectral broadening of a 20 fs femtosecond laser pulse in a gas-filled hollow-core fiber (see Section 4.1). An important question is whether such short pulses are temporally stretched in a free-electron plasma. Assuming the experimental conditions, i.e. $\lambda_{\mathrm{FEL}} = 5.5\,\mathrm{nm}$, the pulse propagates through a 100 nm thin free-electron plasma. The pulse stretching was calculated by FOURIER transformation of an octave-spanning visible spectrum and the accumulated spectral phase within the plasma. Owing to the marginal thickness of the free-electron layer, the pulse will be stretched to 4.1 fs. Thus, the temporal resolution is not limited on the femtosecond-scale.

3.6.3 Spectral investigation of the gating process

At a given free-electron density, the optical properties strongly depend on the ratio between the plasma frequency and the optical frequency, $\omega_{\mathrm{P}}^2/\omega$ (see Eq. 2.70). Thus, the transmission function must be frequency dependent, $G = G(t, \omega)$. This might influence the resolution of the measurement. The question is whether different frequency components are gated earlier or later than others. This is investigated for broad optical spectrum, spanning almost two octaves. Assuming a FOURIER-limited probe pulse (no time-dependence of the optical frequency), the measured cross-correlation signal can be written as

$$\begin{aligned} S(\Delta t) &= \int_t \int_\omega I_{\mathrm{L}}(t) G(t - \Delta t, \omega)\ \mathrm{d}t\mathrm{d}\omega \\ &= \int_t I_{\mathrm{L}}(t) G'(t - \Delta t)\ \mathrm{d}t \end{aligned} \tag{3.14}$$

with the spectrally integrated transmission function,

$$G'(t - \Delta t) = \int_\omega G(t - \Delta t, \omega)\ \mathrm{d}\omega, \tag{3.15}$$

normalized to 1. In Fig. 3.8, optical transmission functions, $G(t)$, are plotted for different optical wavelengths ranging from $\lambda_{\mathrm{L}} = 400\,\mathrm{nm}$ (blue line) to $\lambda_{\mathrm{L}} = 1100\,\mathrm{nm}$ (grey line), simulated assuming a 10 fs FEL pulse with $\lambda_{\mathrm{FEL}} = 5.5\,\mathrm{nm}$. The spectrally integrated function, $G'(t)$, is also plotted (dash-dotted line). While the absolute change of transmission strongly depends on the ratio $\omega_{\mathrm{P}}^2/\omega^2$, the actual duration of the different transmission curves mainly depend on the

FEL pulse duration. The function $G(t)$ at 400 nm is delayed by 5 fs with respect to the function $G(t)$ at 1100 nm, introducing a maximum error of ±2.5 fs.

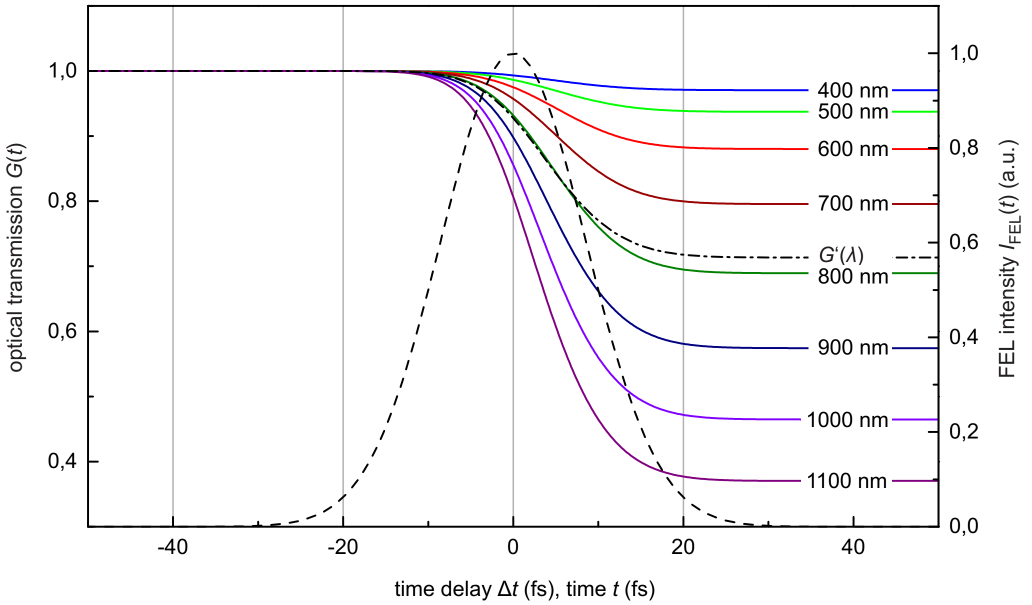

Figure 3.8 Transmission function, $G(t,\lambda)$ calculated for different optical wavelengths, as indicated in the legend. The difference in duration between the 400 nm function and the 1100 nm function is 5 fs, introducing a maximum error of ±2.5 fs. The spectrally integrated transmission function, $G'(t)$, is also plotted.

3.6.4 Complex pulse shapes

As shown before, using proper imaging and probe pulses shorter than 10 fs, the resolution can be increased to sub-10 fs, approaching the few-fs limit of the electronic response (see Section 2.5.4). Now the question remains, if it is possible to detect complex FEL pulse structures with this type of measurement. In the following, the performance of the method is evaluated, concerning the detection of complex FEL intensity envelopes. Therefore, cross-correlations, $S(\Delta t)$ were calculated for two different kinds of pulse shapes, double-pulses and seeded pulses. An FEL *double pulse* is simulated, consisting of two individual GAUSSIAN envelopes,

$$I_{\mathrm{FEL}}(t) = I_0 \left[(1-a) e^{-4\ln 2 \left(\frac{t - t_{\mathrm{sep}}}{\tau_{\mathrm{FEL}}} \right)^2} + a e^{-4\ln 2 \left(\frac{t + t_{\mathrm{sep}}}{\tau_{\mathrm{FEL}}} \right)^2} \right], \tag{3.16}$$

each with $\tau_{\mathrm{FEL}} = 10\,\mathrm{fs}$ FWHM pulse duration. The two intensity maxima are separated by t_{sep}, and the intensity ratio between the leading pulse and the trailing pulse is a, with I_0 being the maximum intensity. In Fig. 3.9a and c, different double pulse configurations are shown for $a = 0.5$ with $t_{\mathrm{sep}} = 10\,\mathrm{fs}$ (a, solid line) and $t_{\mathrm{sep}} = 20\,\mathrm{fs}$ (c, solid line), respectively. Correspondingly, for both cases the transmission function, $G(t)$, is calculated for $\lambda_{\mathrm{FEL}} = 5.5\,\mathrm{nm}$ (red line). As the electron density increases proportionally with the integrated FEL intensity, the transmission function, $G(t)$, features two transients (one negative slope during each single pulse). In order to resolve this function in the cross-correlation, the two transients need to be resolved by a sufficiently short probe pulse. The optical probe pulse in this calculation is a GAUSSIAN pulse with $\tau_\mathrm{L} = 10\,\mathrm{fs}$ FWHM with a central wavelength $\lambda_\mathrm{L} = 800\,\mathrm{nm}$. The corresponding cross-correlations are calculated in Fig. 3.9b and d (blue solid lines). For direct comparison, the cross-correlation with single GAUSSIAN pulses of the same energy are simulated (blue dashed lines). The single GAUSSIAN pulses have in either case a pulse duration of $\tau = \tau_\mathrm{FEL} + t_\mathrm{sep}$. Hence, the FWHM duration is the same as for the double pulse. In Fig. 3.9b, the resolution limit is demonstrated, $t_\mathrm{sep} = \tau_\mathrm{L} = 10\,\mathrm{fs}$. The ambiguity between both correlations is very high and the two transients are not resolved. In Fig. 3.9d, the separation is larger, $t_\mathrm{sep} = 2\tau_\mathrm{L} = 20\,\mathrm{fs}$. In this case, the two transients belonging to the double pulses are clearly resolved and the difference to the simulated cross-correlation belonging to the single pulse is obvious. Thus, with sufficient temporal resolution, evidence of multiple intensity maxima can be observed. This information can be used as initial guess for the fitting algorithm.

Under experimental conditions, the stability of the fitting algorithm might be limited due to signal noise. This was tested by artificially introducing a high signal-to-noise ratio, *SNR*, to the simulated cross-correlations. An FEL double pulse was assumed, according to Eq. (3.16), with $\tau_\mathrm{FEL} = 10\,\mathrm{fs}$, $t_\mathrm{sep} = 20\,\mathrm{fs}$ and $a = 0.4$. The FEL wavelength was $\lambda_\mathrm{FEL} = 5.5\,\mathrm{nm}$ and the optical probe pulse had a pulse duration of $\tau_\mathrm{L} = 10\,\mathrm{fs}$ at $\lambda_\mathrm{L} = 800\,\mathrm{nm}$. Signal noise, f_ξ, was added to the simulated cross-correlation of the FEL double pulse and the laser,

$$S_\xi(\Delta t) = S(\Delta) + f_\xi\left(-\frac{\xi}{2}, \frac{\xi}{2}\right), \tag{3.17}$$

where $f_\xi \in (-\xi/2, \xi/2)$ is a random number from a uniform distribution in the given interval. The signal-to-noise ratio is defined as $SNR = 1/\xi$. The fitting algorithm was configured for double pulses as initial guess, according to Eq. (3.16). This assumption can be derived by identifying two transients in the data. Possible solutions for the fitting were a single pulse ($t_\mathrm{sep} = 0$) and the double pulse ($t_\mathrm{sep} > 0$). The initial parameters and boundaries were as follows: $\tau_\mathrm{FEL} = 20\,\mathrm{fs}$ with $\tau_\mathrm{FEL} \in (0, 100)\mathrm{fs}$, $t_\mathrm{sep} = 30\,\mathrm{fs}$ with $t_\mathrm{sep} \in (0, 30)\,\mathrm{fs}$, and $a = 0$ with $a \in (0, 1)$. As a figure of merit, the deviation of the fitted parameters from the originally defined parameters, $\Delta = \Delta p/p$, was used (with p representing one of the parameters). Another figure of merit was the root-mean-square (rms) error,

$$\Delta I_\mathrm{FEL} = \sum_{t=-T/2}^{t=+T/2} \sqrt{\frac{[I_\mathrm{FEL}(t) - I_\mathrm{fit}(t)]^2}{T}}, \tag{3.18}$$

with the absolute difference between the retrieved intensity envelope, $I_\mathrm{fit}(t)$, and the simulated intensity envelope, $I_\mathrm{FEL}(t)$, within the time window of $\Delta T = 150\,\mathrm{fs}$. The fitting procedure was performed for different *SNR* ranging from 100 to 3.0 $[1/\xi]$. The results are summarized in Fig. 3.10. Here, the parameter deviation, Δ, and the rms error, ΔI_FEL, are plotted in dependence on the *SNR* (see legend). Between $SNR = 100$ and $SNR = 20$, the pulse parameters could be retrieved with a deviation $\Delta < 10\%$ (indicated by dashed line). In this range, the rms error is below 3%. At $SNR = 3$ and lower, the algorithm does not converge.

As an example, the pulse retrieval for $SNR = 20$ is shown in Fig. 3.10b. The simulated cross-correlation, $S_\xi(\Delta t)$ with $\xi = 0.05$ (white rectangles), and the fitted cross-correlation, $S(\Delta t)$ (blue line), feature the two transients, indicating a double pulse. The originally simulated double pulse intensity, $I_\mathrm{FEL}(t)$, is compared with the retrieved intensity, $I_\mathrm{fit}(t)$ (red line).

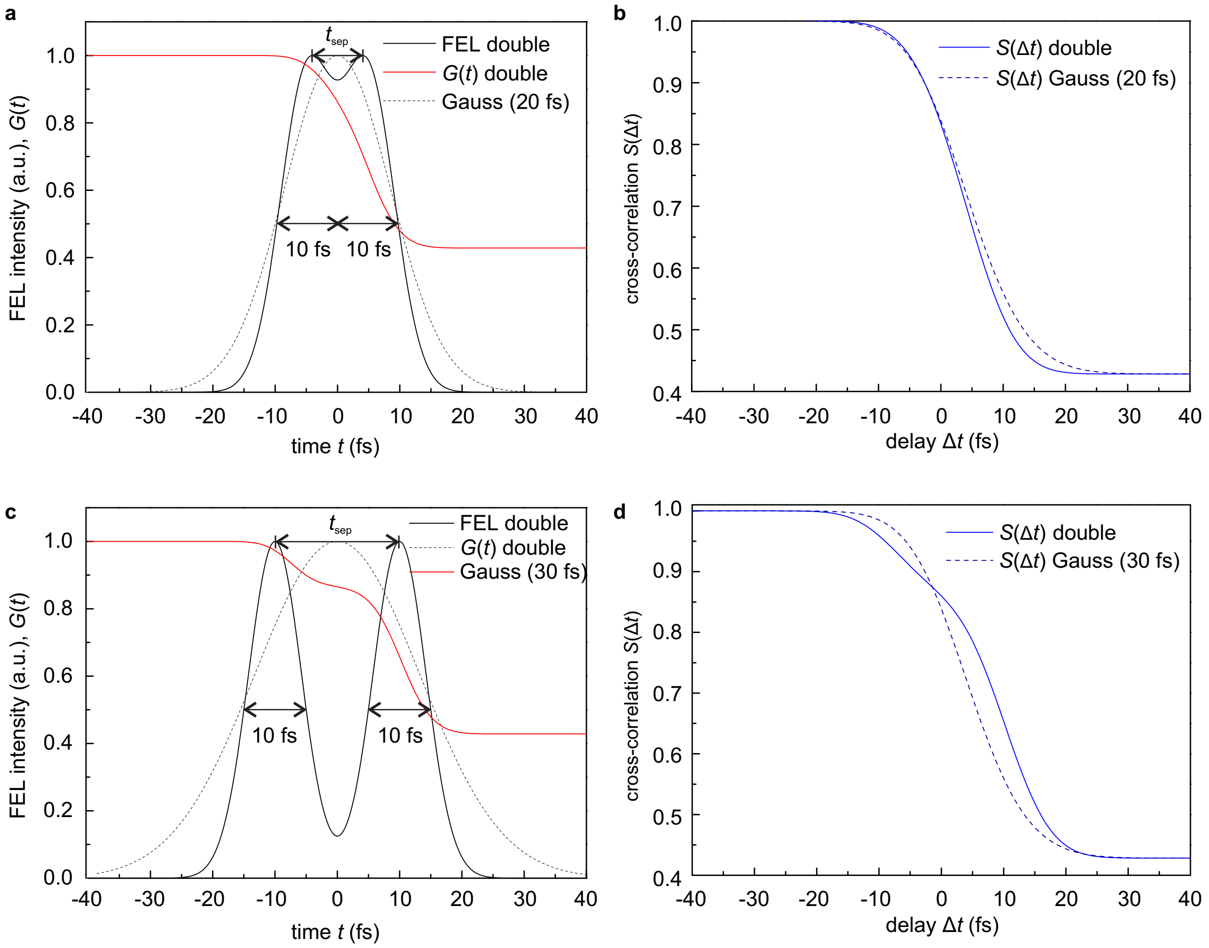

Figure 3.9 Calculated cross-correlations, $S(\Delta t)$, of GAUSSIAN double pulses (blue solid lines in (b) and (d)). The double pulses (black solid lines in (a) and (c)) have a pulse duration of $\tau_{\mathrm{FEL}} = 10\,\mathrm{fs}$ each, separated by t_{sep}. For the double pulses, the transmission function, $G(t)$, is also plotted (red solid line). (**a**) Separation of $t_{\mathrm{sep}} = 10\,\mathrm{fs}$. (**b**) Corresponding cross-correlation with a 10 fs probe pulse. (**c**) Separation of $t_{\mathrm{sep}} = 20\,\mathrm{fs}$. (**d**) Corresponding cross-correlation with a 10 fs probe pulse. For comparison, the cross-correlations (blue dashed lines) were also calculated for single GAUSSIAN pulses with double the pulse duration, $\tau = \tau_{\mathrm{FEL}} + t_{\mathrm{sep}}$ (black dashed lines). For double pulses with a separation time larger than the laser pulse duration, $t_{\mathrm{sep}} > \tau_{\mathrm{L}}$, the cross-correlation can be clearly distinguished from the cross-correlation with a single pulse.

It can be concluded that the developed data processing and fitting routine ensures a very robust retrieval of assumed pulse durations, even for a low signal-to-noise ratio in the normalized cross-correlations. For comparison, the experimental signal-to-noise ratio in the presented measurements was $SNR > 100$ for the fused silica target (Fig. 3.6) and $SNR > 20$ for the Si_3N_4 target (Fig. 3.7).

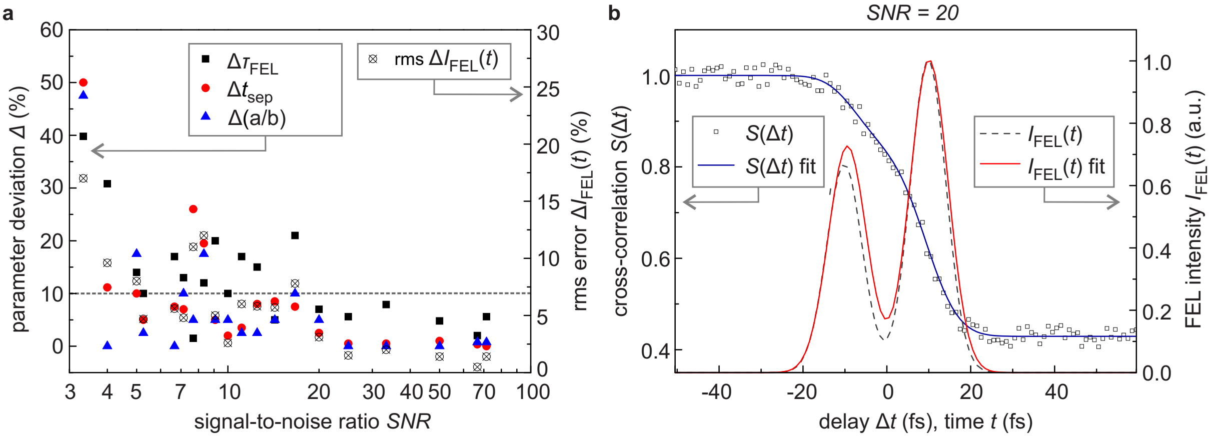

Figure 3.10 Performance simulation of the FEL pulse retrieval under the presence of noise on a simulated cross-correlation. (**a**) Deviation of the fitting parameters from the input parameters, $\Delta = \Delta p/p$, for different signal-to-noise ratios, SNR. Here, p corresponds to the pulse duration, τ_{FEL} (black rectangles), the pulse separation, t_{sep} (red dots), and the intensity ratio, a (blue triangles). Additionally, the rms deviation of the fitted FEL intensity from the input FEL intensity, $\Delta I_{\mathrm{FEL}}(t)$ (cross-circles), was calculated. (**b**) Example for $SNR = 20$: Simulated cross-correlation, $S_{\xi}(\Delta t)$, with $\xi = 0.05$ (white rectangles), fitted cross-correlation, $\Delta S(t)$ (blue line), input FEL intensity, $I_{\mathrm{FEL}}(t)$, and retrieved intensity envelope, $I_{\mathrm{fit}}(t)$.

A very promising application for the presented pulse diagnostics method is the characterization of seeded FEL pulses. For example at FERMI@Elettra (Trieste, Italy), double pulses can be generated via seeding with high gain harmonic generation (HGHG) [7]. At FLASH, direct seeding at $\lambda_{\mathrm{FEL}} = 38.5\,\mathrm{nm}$ via higher order harmonic generation (HHG) was recently demonstrated [72]. For the seeded pulses, single pulses are expected with a pulse duration of $< 10\,\mathrm{fs}$, according to the spectral bandwidth of the HHG of about $\Delta\lambda = 0.2\,\mathrm{nm}$ FWHM. A simulation of cross correlations was performed for comparable parameters. For the probe pulse, the pulse duration of 35 fs was chosen, according to the seeding laser system at FLASH (Ti:sapphire amplifier, Coherent Hidra). For the unseeded (SASE) FEL pulse, a GAUSSIAN intensity envelope with a pulse duration of 200 fs FWHM was assumed. For the seeded FEL pulse, a complex pulse structure is assumed. It is a superposition of two GAUSSIAN pulses, one with 200 fs pulse duration (SASE background) and one with 20 fs pulse duration (seeded part). A seeded-to-SASE intensity ratio of $I_{\mathrm{seeded}}/I_{\mathrm{SASE}} = 20$ is assumed. In Fig. 3.11, the input intensity profiles, $I_{\mathrm{FEL}}(t)$ for the SASE pulse (blue dashed) and the seeded pulse (red dashed) are plotted. The corresponding cross-correlations, $S(\Delta t)$, are plotted as solid lines. The signal from the seeded pulse (red) consists of three parts. First, for negative delays it follows the signal from the leading SASE background (blue). Then, between $\Delta t = -50\,\mathrm{fs} \ldots 50\,\mathrm{fs}$ it is characterized by a steep transient through the short intensity envelope of the seeded fraction of the pulse. At the end, for large delays, it turns into a flat transient, corresponding to the trailing SASE background. Owing to the energy difference between the SASE and the seeded pulse, the difference in the absolute transmission change is larger for the seeded pulse. With the probe pulse duration of 35 fs, the pulse duration of the seeded part of the pulse can be determined only with a large error. However, the seeded case and the SASE case can be clearly distinguished by the slope of the transient and the total transmission change. With a short probe laser (< 20 fs) and sufficient temporal resolution, the intensity envelope of the seeded part as well as of the SASE background can be retrieved.

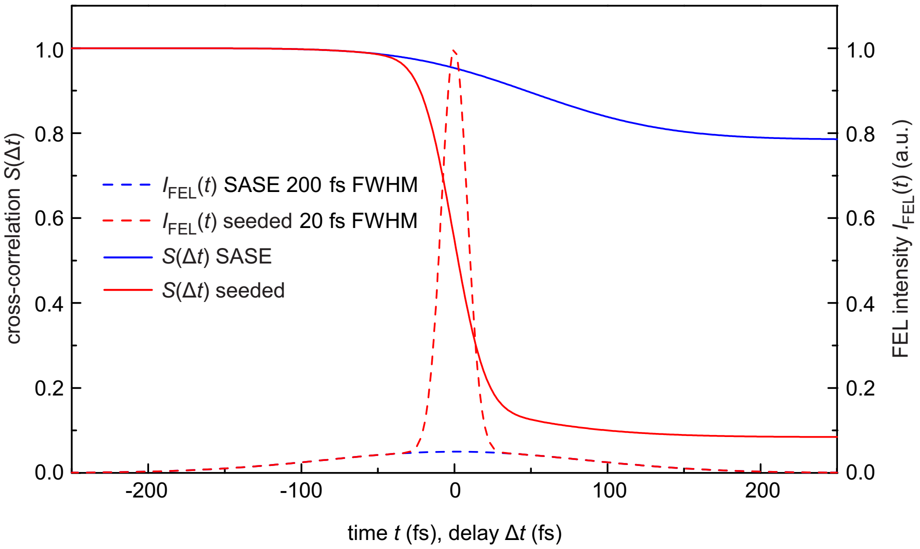

Figure 3.11 Simulated cross-correlation, $S(\Delta t)$, of a seeded FEL pulse (red solid line) compared with an unseeded SASE pulse (blue solid line). For the simulation, the probe laser pulse duration was $\tau_L = 35$ fs. The intensity envelope, $I_{\mathrm{FEL}}(t)$, of the seeded pulse consists of a superposition of a SASE background part (200 fs FWHM) and a seeded part (20 fs FWHM). The intensity of the seeded pulse (red dashed) exceeds the intensity of the unseeded SASE pulse (blue dashed) by a factor of twenty.

3.7 Compact laser amplifier for increased temporal resolution at existing pump-probe beamlines

A compact broadband non-collinear OPA was set up to achieve shorter optical probe pulses for high resolution cross-correlation measurements. Most pump-probe laser systems available at today's XUV and X-ray FELs are mJ-class Ti:sapphire amplifiers. The available pulse durations are between 30 fs and 100 fs, limiting the resolution of the cross-correlation. The compact OPA presented here was pumped at the second-harmonic wavelength (400 nm) of the 60 fs pump-probe laser available at FLASH. The requirements for the cross-correlation measurement are the shortest possible pulse duration, a radially symmetric near-field profile that can be expanded for homogeneous illumination of the sample, and a pulse energy of $> 1\,\mu$J, which is sufficient to expose the CCD within a single shot. Furthermore, complexity and long additional beam path should be avoided. Because of the latter fact, the pulse duration requirement was fixed to about 20 fs, which can be achieved using a prism compressor without higher-order phase compensation. The compact setup has a footprint of $30 \times 60\,\mathrm{cm}^2$.

The experimental setup was tested at the FLASH pump-probe laser. A schematic is depicted in Fig. 3.12, similar to [88]. The pump pulses from the 10 Hz Ti:sapphire CPA (Coherent Hidra) had a pulse energy of 500µJ, a pulse duration of 64 fs, a beam diameter of 4 mm at $1/e^2$ intensity and a central wavelength of $\lambda_L = 800\,\text{nm}$. The required broadband seed pulses were obtained from white-light generation (WLG). To this end, a fraction of the pulse was focused in a 3 mm sapphire plate with an $f = 100\,\text{mm}$ lens (L1) and an aperture. The generated WLG pulses were recollimated with an $f = 100\,\text{mm}$ lens (L2) and spectrally separated from the pump by an 800 nm notch filter (F). Further, a 5 mm fused silica plate (FS) was added to introduce additional material dispersion for the stretching. The total amount of dispersive material was 9.5 mm fused silica (L1, L2, F, FS) and about 3 mm sapphire. The broadband WLG pulses were stretched to about 0.8 ps at $1/e^2$ intensity. The shorter OPA pump pulse acts as a temporal frequency gate for the chirped WLG pulses during the amplification (group-delay-dispersion $\beta_2 = 700\,\text{fs}^2$ at 680 nm, before OPA). This effect was used to adjust the amplified central wavelength by varying the pump-to-signal delay.

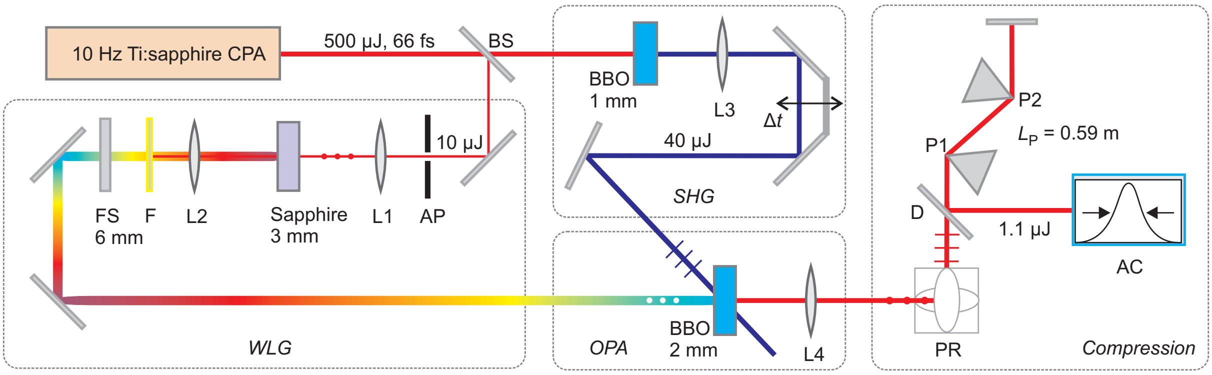

Figure 3.12 Schematic experimental setup of the compact OPA tested for the generation of 20 fs pulses at FEL beamline endstations. The available Ti:sapphire pump-probe laser (pulse energy: about 0.5 mJ, pulse duration: 64 fs) was frequency doubled in a 1 mm BBO to pump the OPA at 400 nm, focused with a lens of $f = 300\,\text{mm}$ (L3). For the broadband signal seed generation, a fraction of the pulses was used for WLG in a 3 mm sapphire plate, focused by a $f = 100\,\text{mm}$ lens (L1) and an aperture (AP). After refocusing with $f = 100\,\text{mm}$ (L2), the pump was blocked by a notch filter (F). Additional material dispersion is added by a 6 mm fused silica glass plate. OPA is achieved in a BBO with type-I non-collinear phase-matching. After recollimation with an $f = 150\,\text{mm}$ lens, the pulse was compressed in a fused silica prism pair (apex distance $l_P = 0.59\,\text{m}$, PR: polarization rotating telescope).

For pumping the OPA, the larger fraction of the pulse energy was used. The second-harmonic was generated (SHG) in a 1 mm BBO using type-I phase-matching ($\theta = 29.2°$). 40µJ pulses at 400 nm (p-polarized) were focused in front of the 2 mm BBO crystal for OPA. In this way, the pump intensity could be adjusted between 100–300 GW cm^{-2} by variation of the crystal position with respect to the focus. The pump-to-signal delay, Δt, between the SHG and the WLG pulses was adjusted by a mirror pair mounted on a translation stage with µm precision. The phase-matching was adjusted for broadband amplification with the phase-matching angle $\theta = 27.3°$ and the non-collinear angle $\alpha = 3.8°$. For the temporal pulse compression, a fused silica prism pair was used (P1, P2), to compensate the amount of material dispersion introduced by 3 mm sapphire, 11.5 mm glass (L1, L2, F, FS, L4), 2 mm BBO and 2 m air along the beam path. In total, a group delay dispersion of $\beta_2 = 1000\,\text{fs}^2$ was compensated using a prism apex distance of $l_\mathrm{P} = 0.59\,\mathrm{m}$. The residual third-order dispersion was $\beta_3 = -1500\mathrm{fs}^2$.

The almost radially symmetric near-field profile of the amplified pulses is shown in Fig. 3.13c. The amplified pulse energy was $(1.5 \pm 0.1)\mu\mathrm{J}$. The central wavelength of the amplified spectrum was tunable between 549 nm and 709 nm by varying the pump-to-signal delay. Selected spectra are shown in Fig. 3.13a. The corresponding bandwidth at $1/e^2$ intensity is specified in the legend. For the compression, the spectrum centered at $\lambda_\mathrm{c} = 680\,\mathrm{nm}$ was chosen, because the residual TOD is lowest for this wavelength range. The pulse duration was characterized using an intensity autocorrelator with a 100 µm BBO crystal. The measured autocorrelation is shown in Fig. 3.13b. Assuming a GAUSSIAN intensity envelope, the pulse duration was $\tau_\mathrm{P} = (19.9 \pm 0.6)\,\mathrm{fs}$. The FOURIER-limited pulse duration of 13 fs can be achieved with specially designed double-chirped mirrors ($\beta_2 = -1000\,\mathrm{fs}^2$, $\beta_3 = -500\,\mathrm{fs}^3$, at $\lambda_\mathrm{c} = 680\,\mathrm{nm}$). The pulse energy after the compressor was $(1.1 \pm 0.1)\,\mu\mathrm{J}$.

This compact amplifier is a versatile tool for probing the transient transmission of solid-state free-electron plasmas generated by ultrashort FEL pulses. It allows the FEL pulse duration measurement of single FEL pulses with unprecedented temporal resolution, independent from the pulse duration of the available pump-probe laser at the FEL facility.

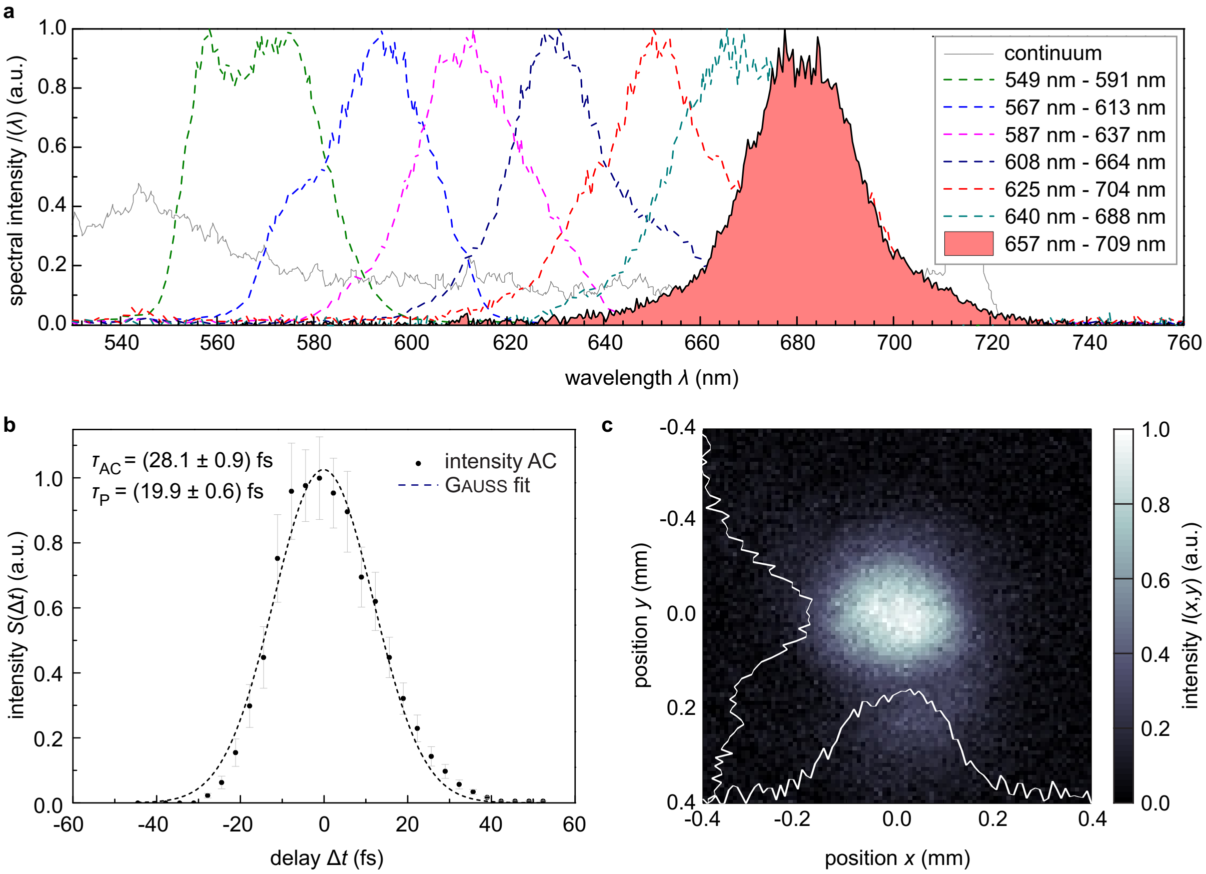

Figure 3.13 Characterization of the amplified pulses. (**a**) Wavelength tunability was achieved by variation of the pump-to-signal delay. The amplified bandwidths, $\Delta\lambda$, are denoted in the legend. The red-shaded spectrum was used for compression. (**b**) Intensity autocorrelation of the compressed pulses. The pulse duration is $19.9 \pm 0.6\,\mathrm{fs}$ (GAUSSIAN intensity envelope). (**c**) Spatial beam profile after the prism compressor.

Chapter 4

High repetition rate optical parametric chirped-pulse amplifier

For increasing the performance of the free-electron laser facility FLASH, a high repetition rate optical parametric chirped-pulse amplifier (OPCPA) is being developed for the application as pump-probe laser and as FEL seeding laser. The final laser pulse repetition rate of 100 kHz to 1 MHz is fixed by the electron bunch repetition rate of the accelerator to provide one optical laser pulse for each FEL pulse. This benefits not only the statistical significance of experiments at FLASH, but also the seeding of the FEL at high repetition rate, enabling the full control over each XUV pulse generated by the FEL. The FEL delivers XUV pulses with durations down to $\tau_{\mathrm{FEL}} = 10\,\mathrm{fs}$ to 30 fs in SASE mode with low electron bunch charge. Highest temporal resolution in XUV/optical pump-probe experiments is attained using shorter optical laser pulses with pulse durations $\tau_{\mathrm{L}} < \tau_{\mathrm{FEL}}$. To achieve such high resolution, the arrival time jitter between the optical pulse and the FEL pulse must be even smaller, $\tau_{\mathrm{jitter}} < \tau_{\mathrm{L}} < \tau_{\mathrm{FEL}}$. In combination with the XUV/optical cross-correlation method developed in this work (Chapter 3), the jitter can be accurately determined and tagged to the experimental data for each FEL pulse. With such an outstanding laser system, FLASH would provide worldwide unique experimental conditions for time-resolved FEL experiments.

FLASH operates in a pulsed *burst mode*. Each burst generates up to 800 brilliant ultrashort XUV pulses, corresponding to an intra-burst repetition rate of up to 1 MHz. This burst pattern should be also delivered by the optical pump-probe laser and the seeding laser. The requirements for the pulse duration and the pulse energy are defined according to the requirements for seeding and for high resolution pump-probe experiments [36, 142]. The developed system has to fulfill the following **demands on the laser technology:**

- **Burst-mode operation:** Pulsed operation with 10 Hz burst repetition rate and a final intra-burst repetition rate of 100 kHz to 1 MHz. The burst duration is 800 µs. It is particularly challenging to operate a conventional laser amplifier in such a burst-mode, because it is always in a non-equilibrium state of population inversion.

- **Pulse energy:** For the application as pump-probe laser, the pulse energy should be 25 µJ in the first version and 1 mJ in the final version. For the application as seeding laser, the pulse energy should be as high as possible, at least 1 mJ.

- **Pulse duration:** For the pump-probe laser, the pulse duration should be sub-20 fs in the first version and sub-10 fs in the final version. For the high gain harmonic generation (HGHG) seeding, a pulse duration of about 30 fs is required with tunable center wavelength. For the direct seeding via higher order harmonic generation (HHG), a pulse duration between 15 fs and 20 fs is required to match the FEL gain bandwidth.

- **Energy and spectral stability:** The system should be as stable as possible. A maximum of 1% rms deviation from the average pulse energy and the central wavelength should be achieved.
- **Operation time:** A laser system that operates in an FEL environment has to be long-term operational with the aforementioned parameters for at least 12 h. This is indispensable for an uninterrupted operation during FEL experiments.

In this chapter, first, the state-of-the-art of ultrashort laser systems will be reviewed. In the following, the concept of optical parametric chirped-pulse amplification is explained in detail and the choice of the optimal nonlinear optical crystal is evaluated. Furthermore, the experimental setup and the results attained with a 27.5 kHz (intra-burst) prototype are presented. A technique to ensure long-term stability of high-power OPCPAs is investigated, which is an important focus of this work. Finally, thermal limitations in OPCPA at kW average power are discussed.

4.1 State-of-the-art Ti:sapphire amplifiers

Common technology for ultrashort pulse generation with few-femtosecond pulse duration is the Ti:sapphire[1] solid-state laser with KERR-lens mode-locking [79, 143]. Nowadays, Ti:sapphire oscillators generate pulses shorter than two optical cycles by accurate intra-cavity dispersion control with specially designed double-chirped mirrors [144]. These oscillators are also commercially available (e.g. VENTEON pulse:one, Femtolasers Rainbow). The amplification of such short pulses is generally achieved by the implementation of chirped-pulse amplification (CPA) [145], shown schematically in Fig. 4.1a. This technique needs temporal stretching of the ultrashort pulses from the oscillator by several orders of magnitude, such to prevent nonlinear optical effects or even damage of the amplifier material. The stretching is achieved by adding a defined amount of dispersion (stretcher), for example by a grating or prism setup. After the amplification, the pulses are compressed by a dispersive element (compressor), taking into account dispersion with opposite sign of the stretcher and of the amplifier material. However, in Ti:sapphire amplifier systems the spectral bandwidth is considerably reduced, due to spectral gain-narrowing [146]. This limits the shortest amplified pulse duration to about 20 fs. Spectral broadening techniques, such as self-phase-modulation in gas-filled hollow-core fibers [147] (SPM), were implemented to re-enhance the bandwidth of amplified pulses. In combination with active and passive control of the spectral phase and proper pre-compensation of the spectral amplitude, the amplification of 5 fs pulses to mJ pulse energies was attained [148, 149]. Such spectral broadening methods suffer from additional losses of about 50% and are limited in pulse energy.

The main disadvantage of Ti:sapphire laser amplifier systems is its ultimate limitation in average power due to the large quantum defect, $q = \hbar(\omega_{\text{pump}} - \omega_{\text{laser}})$, of Ti:sapphire [150]. Typically, the pump wavelength is between 527–532 nm and the average laser wavelength is centered around 800 nm. The resulting quantum defect, $q = 1/3\hbar\omega_{\text{pump}}$, indicates that about

---

[1] Ti^{3+}-doped Al_2O_3

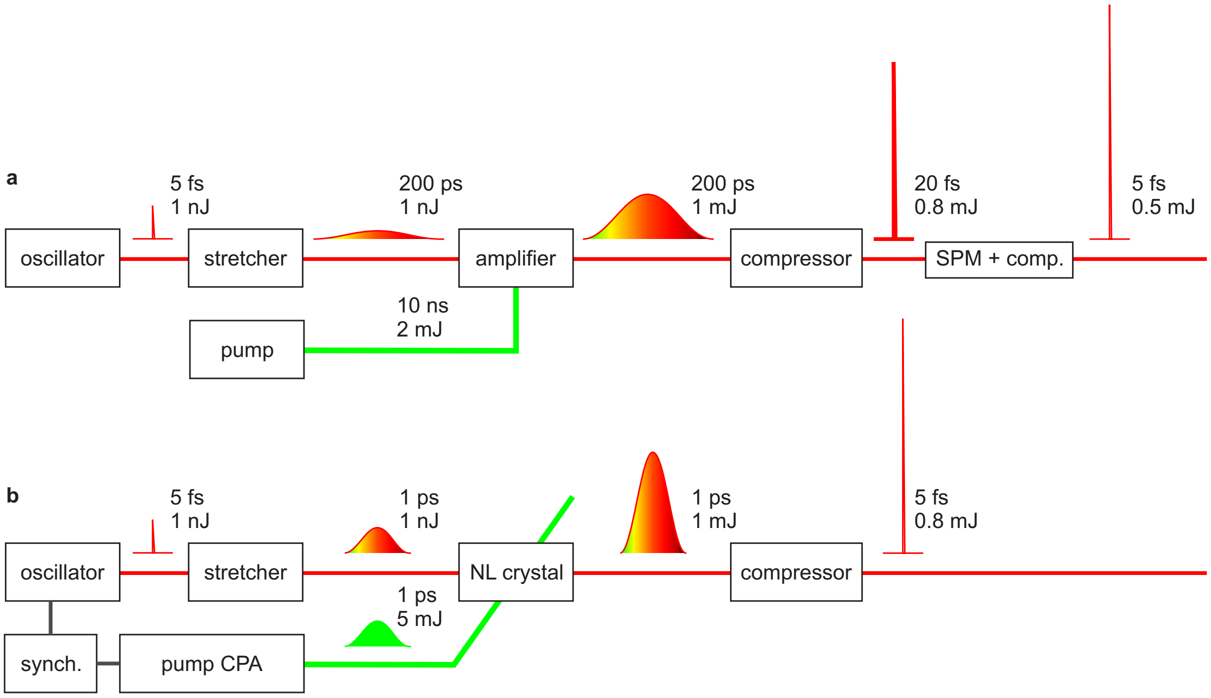

Figure 4.1 Chirped-pulse amplification (CPA). (**a**) Conventional Ti:sapphire CPA: 5 fs pulses from a KERR-lens mode-locked oscillator are stretched in a dispersive device (stretcher). The stretched pulses are amplified in a Ti:sapphire crystal, typically pumped by the SHG of a *Q*-switched Nd:YAG or Nd:YLF laser (pump). The amplified pulses are compressed in a dispersive device (compressor) with opposite dispersion than the stretcher. Owing to spectral gain narrowing, the compressed pulse duration is larger than the oscillator pulse duration. Optionally, a nonlinear spectral broadening stage with specially designed compressor (self-phase modulation in a hollow-core fiber, SPM + comp.) can be implemented to achieve shortest pulse durations. (**b**) Optical parametric chirped-pulse amplifier: Similar to (a). But here, less stretching of the oscillator pulses is required to match the temporal amplification window of the pump pulse. Pump and signal pulses must be synchronized either by electronic or optical techniques (synch.) to keep their overlap within the amplification window. Instead of an active medium in the laser amplifier, a nonlinear crystal (NL crystal) is used, and the pump laser is an ultrashort CPA (pump CPA), based on Ti:sapphire or rare-earth-doped materials. OPCPA with non-collinear phase-matching has a large amplification bandwidth, which makes further spectral broadening unnecessary. The parameters for pulse durations and pulse energies are exemplary.

$1/3$ of the absorbed pump energy is dissipated as heat. The resulting thermo-optic effects, such as thermal lensing, can be reduced by complex cavity design and sophisticated cryogenic cooling technology. The physical limit of the output power of Ti:sapphire amplifiers is given by the cryogenic cooling capacity. Output powers of tens of Watts have been achieved so far [151, 152], allowing repetition rates of tens of kilohertz at 1 mJ pulse energy. Burst repetition rates of up to 1 MHz with pulse energies in the mJ range are not achievable due to massive heating of the amplifier medium during the burst. Hence, a novel laser amplifier system has to be designed to fulfill the specifications.

4.2 Optical parametric chirped-pulse amplification

Optical parametric amplification (OPA) is a second-order nonlinear process. The energy of an intense pump pulse is transferred to a signal and an idler pulse, which are overlapped in a nonlinear optical crystal. For the amplification, no population inversion and thus no energy storage is required within the medium. As the photon energy difference is carried away by the idler radiation, no quantum defect exists. Furthermore, non-collinear phase-matching in OPA offers a large amplification bandwidth, as compared to Ti:sapphire amplifiers. The concept of optical parametric chirped-pulse amplification (OPCPA) combines the laser CPA scheme with OPA (Fig. 4.1b). With this powerful combination, the advantages of both methods are merged [153–155]. Pulses with only a few optical cycles can be amplified to very high pulse energies with terawatts of optical power [156–158]. Furthermore, unprecedented high average powers can be attained, owing to the instantaneous nature of the nonlinear parametric response. For example, a pulse duration of 5 fs was achieved at an average power of 22 W [159]. However, at very high average power the residual absorption of signal, idler and pump pulses needs to be taken into account as sources of heat. In order to develop an OPCPA system that meets the requirements for the FLASH seeding and pump-probe laser, new challenges have to be faced. In the following, the advantages and challenges of OPCPA are summarized.

Major advantages:

- **Gain bandwidth:** The amplification of a full optical octave is possible in a single amplification stage [159], using non-collinear phase-matching in a sufficiently short crystal, pumped at sufficiently high intensity. The amplification bandwidth is limited by phase-matching. With pumping at multiple wavelengths, even more than one optical octave is possible [160].
- **Single-pass gain:** A high single-pass gain of $G > 10^6$ can be achieved with only a few mm of nonlinear crystal. This relaxes the design complexity of the amplifier stages, whereas conventional laser amplifiers require multi-pass or regenerative amplifiers.
- **Power scaling:** Owing to the instantaneous nature of the nonlinear parametric response, no energy storage within the medium is required for amplification. Consequently, the absorption of photons is reduced by several orders of magnitude. This enables unprecedented average powers and repetition rates, limited only by the residual absorption of signal, idler and pump pulses.
- **Spectral tunability:** The amplified bandwidth and central frequency can be adjusted by several degrees of freedom, for example by varying the phase-matching angle or the temperature [88, 161].

- **Burst-mode:** The repetition rate is fixed by the repetition rate of the pump laser. A burst pattern of the pump laser will be directly transferred to the OPCPA. Unlike the conventional laser, the OPA process does not rely on population inversion. Thus, the challenges concerning the non-equilibrium laser operation in the burst-mode are shifted to the OPA pump laser.

Major challenges:

- **Pump laser requirements:** An additional CPA for the ultrashort pump pulses is required. The pump-to-signal conversion efficiency is around 20% in the presented configuration and highest possible pump pulse energies should be attained. The high intensities needed for driving the broadband nonlinear amplification require picosecond pulse durations, provided by rare-earth doped solid state lasers. The system has to operate in a stable burst mode with high intra-burst repetition rate.

- **Pump-to-signal synchronization:** The amplified energy and bandwidth is highly sensitive to variations of the temporal delay between the short pump and signal pulses. The best conversion efficiency is achieved at optimum temporal overlap. However, optical path length drifts occur due to temperature changes in the pump amplifier or changes of the laboratory environment (e.g. temperature, humidity, pressure). For the drift compensation, high-precision pump-to-signal synchronization techniques are required.

- **Dispersion management:** The temporal stretching and compression scheme of the broadband pulses needs to be carefully designed, because of the strong dispersive influence of the optical elements in the beam path.

- **Amplified noise:** Amplified optical parametric fluorescence (AOPF) can reach significant intensities, if not appropriately suppressed. AOPF can be decreased with cascading amplifier stages using moderate gain.

In conclusion, OPCPA is the best technology available for the development of the high repetition rate laser amplifier at FLASH. However, at a pump-to-signal conversion efficiency of 20%, a pump pulse energy of at least 5 mJ is required at a wavelength of 515 nm to achieve a signal energy of 1 mJ around the central wavelength of 800 nm. At 100 kHz to 1 MHz repetition rates, the development of new kW-level pump amplifiers at sub-picosecond pulse durations is required to fulfill the high OPCPA criteria. Different Yb-based pump CPA concepts are being developed. High average power can be attained owing to the low quantum defect of Yb-doped laser materials, $q = 8.7\%$, e.g. with Yb-doped yttrium-aluminum-garnet (Yb:YAG). The amplified bandwidth of this material supports sub-ps pulse durations. For an efficient heat removal, special active material geometries have been developed, such as Innoslab [162, 163], thin-disk technology [164, 165], and optical fibers with large mode diameter [166] and coherent combining of single amplifiers [167]. The frequency-doubled output of such amplifiers at 515 nm can be used for OPCPA pumping. Taking into account an efficiency of 50% for the frequency-doubling, at least 10 mJ pulse energy have to be delivered by the pump CPA, resulting in 1 kW at 100 kHz and 10 kW at 1 MHz average power during the burst. The development progress of a multi-kW Innoslab burst amplifier (Amphos GmbH, Aachen, Germany) and a multi-kW thin-disk burst amplifier (DESY, Hamburg, Germany) is in progress [165, 168, 169].

4.2.1 Choice of nonlinear optical crystal

The choice of the nonlinear optical crystal for broadband non-collinear OPCPA needs to carefully include several important properties. First of all, the spectral transparency range should cover all interacting optical wavelengths, from the pump (515 nm), over the signal (around 800 nm), to the idler waves (up to 2200 nm). Second, its birefringent properties should support broadband phase-matching over a large signal bandwidth. To minimize spatial walk-off effects (different propagation directions of pump and signal), a small non-collinear angle, α, and a small walk-off angle, ρ, are required. Third, a large effective nonlinear coefficient, d_{eff}, is important for efficient amplification. Finally, high damage threshold and wide availability of the crystals are important. Additionally, for high average power applications low residual absorption at all interacting wavelengths is required as well as a high thermal acceptance (change of phase-matching properties due to thermally induced refractive index changes).

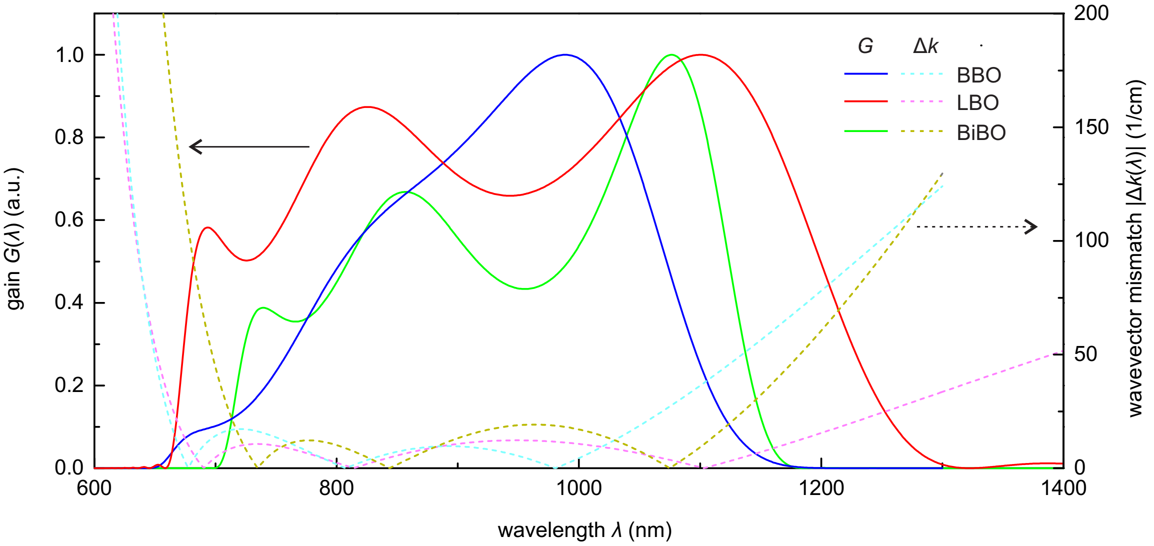

Figure 4.2 Evaluation of the phase-matching bandwidth of different nonlinear crystals. The wavelength dependent signal gain, $G(\lambda)$ (solid lines), was calculated using the undepleted pump approximation. For a better comparison, the each gain curve is normalized to $[0,1]$. The phase mismatch, $|\Delta k(\lambda)|$, between pump, signal and idler was calculated (dashed lines). BBO: $(\Delta\lambda)_{5\%G} = 667\,\mathrm{nm} - 1140\,\mathrm{nm}$ (blue, cyan), LBO: $(\Delta\lambda)_{5\%G} = 667\,\mathrm{nm} - 1276\,\mathrm{nm}$ (red, magenta), BiBO: $(\Delta\lambda)_{5\%G} = 709\,\mathrm{nm} - 1160\,\mathrm{nm}$ (green, see legend).

These properties are incorporated by several borate crystals. The relevant material parameters of β-barium borate (BBO), lithium-triborate (LBO) and bismuth-triborate (BiBO) are listed in Table 4.1. The small-signal gain bandwidths of these three crystals were calculated using the undepleted pump approximation. For BBO, the non-collinear phase-matching was calculated as described in Section 2.4.2. For phase-matching in the biaxial crystals LBO and BiBO, the procedure described in [170] was used. In Fig. 4.2, the calculated small-signal gain, $G(\lambda)$, is plotted in dependence of the signal wavelength, for the interaction angles θ and α stated in Table 4.1. The supported wavelength range at the given angles and at 5% gain threshold is $(\Delta\lambda)_{5\%G} = 667\,\mathrm{nm} - 1276\,\mathrm{nm}$ for LBO (red line), $(\Delta\lambda)_{5\%G} = 667\,\mathrm{nm} - 1140\,\mathrm{nm}$ for BBO (blue line), and $(\Delta\lambda)_{5\%G} = 709\,\mathrm{nm} - 1160\,\mathrm{nm}$ for BiBO (green line). LBO features the largest spectral bandwidth. However, the d_{eff} is low compared to BBO and BiBO, and the single-pass gain is only $G(\lambda) < 10^2$ at the same pump intensity. BBO is the most favorable nonlinear crystal to achieve a high single pass gain, $G(\lambda) > 10^6$, over a large spectral bandwidth, and with a smaller non-collinear angle than BiBO. Nevertheless, LBO has the lowest absorption at 515 nm and the highest damage threshold, which makes it highly attractive for high-power amplifier stages with low single-pass gain. The hygroscopicity of BBO and LBO is sufficiently low for practical application. BiBO is not hygroscopic.

	BBO	LBO	BiBO
chemical formula birefringence (point group) phase-matching plane[a]	β-BaB_2O_4 neg. uniaxial (3*m*) *xz*	LiB_3O_5 neg. biaxial (*mm*2) *xy*	BiB_3O_6 neg. biaxial (*mm*2) *yz*
nonlinear coeff. d_{eff} ()[a]	2.08 pm V^{-1}	0.82 pm V^{-1}	1.97 pm V^{-1}
transparency range (nm)[a]	190–3500	160–3200	286–2500
damage threshold intensity[b]	>5 GWcm^{-2}	>26 GWcm^{-2}	>3.5 GWcm^{-2}
absorption coeff. (532 nm)[c]	1%cm^{-1}	0.3%cm^{-1}	not reported
thermo-optic coeff. d*n*/dT (10^{-6} K^{-1})	$(-9.3)_o$ $(-16.6)_e$[a]	$-(3.76\lambda - 2.3)_x$ $-(6.0\lambda - 19.4)_y$ $-(10\lambda - 3.5)_z$ (λ in µm)[d]	not reported
thermal acceptance[a]$\Delta T \Delta k$	39.69 K·cm	6.8 K·cm	2.74 K·cm
angular acceptance[a]$\Delta\Theta\Delta k$	0.56 mrad·cm	6.86 mrad·cm	1.15 mrad·cm
phase.matching angle θ non-coll. angle α walk-off. angle[a]ρ	24.17° 2.2° 3.2°	17.6° 1.2° 0.4°	43.39° 3.85° 1.4°

[a] values from the freely available software SNLO [171]

[b] damage threshold at a pulse duration of35 ps (BBO and LBO) [172], or 40 ps (BiBO) [173]

[c] reported by the crystal manufacturer CASTECH (China)

[d] from [174]

Table 4.1 Nonlinear optical crystal parameters.

4.3 OPCPA setup and results

The experimental setup of the developed non-collinear OPCPA is schematically displayed in Fig. 4.3. It consists of a broadband front-end, a high-power pump CPA and three BBO crystals of length 3.3 mm, 3.2 mm and 2.0 mm, serving as subsequent broadband amplification stages. As explained in Section 4.2.1, BBO was chosen because it supports a broad spectral gain bandwidth and a reduced spatial walk-off owing to the small non-collinear angle. The high nonlinear coefficient allows for high single-pass gain in shorter crystals, which reduces the dispersion in the signal beam path. The three-stage setup was chosen for two reasons: firstly, the amplified optical parametric fluorescence is reduced by implementing a preamplifier stage (first OPA stage), as explained below; secondly, the total conversion efficiency could be increased by a factor of two by using the residual pump energy in a third OPA stage. The crystal lengths of the individual stages were determined by optimization.

As the frontend, a Ti:sapphire oscillator was used (Venteon Pulse:One OPCPA seed), delivering 2.5 nJ pulses at a repetition rate of 108 MHz. Owing to its broad spectral range from 650 nm to 1150 nm, all-optically synchronized seeding was realized, i.e. the oscillator served as

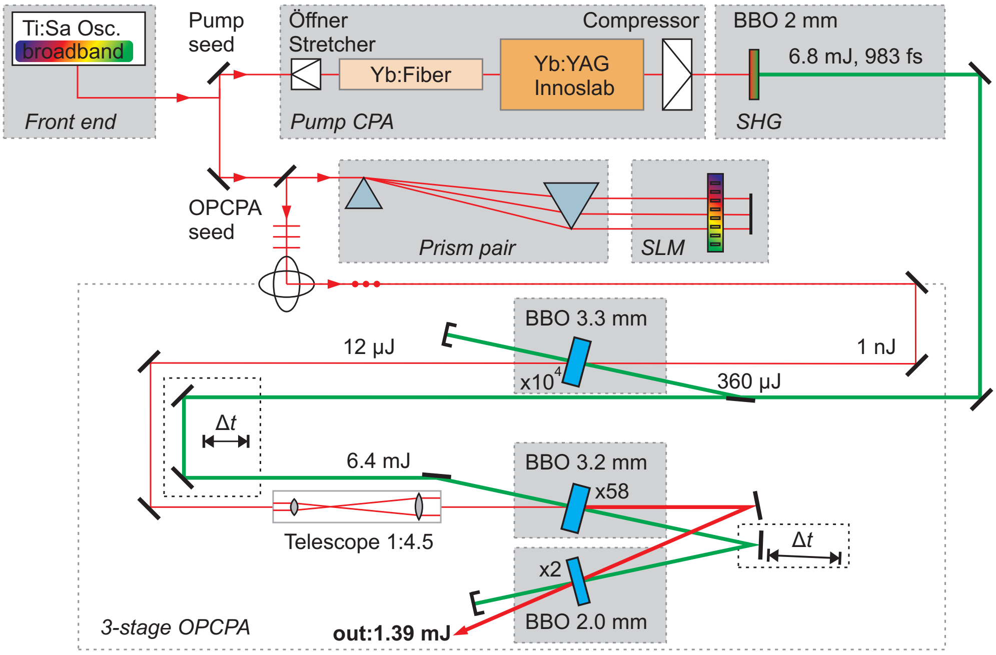

Figure 4.3 Schematic of the high power optical parametric chirped-pulse amplifier (OPCPA). The broadband Ti:sapphire oscillator seeded the OPCPA and the Yb-based pump amplifier. The pump CPA consisted of a 10 W Yb:glass fiber amplifier and a 0.5 kW Yb:YAG Innoslab amplifier. Frequency doubling was achieved in a 2 mm β-barium borate (BBO) crystal. For stretching the OPCPA signal pulses, a prism pair was used. In combination with a spatial light-modulator (SLM), full control of the spectral phase was possible for the dispersion compensation in the system. Three subsequent OPCPA stages were implemented, using BBO crystals of 3.3 mm, 3.2 mm and 2.0 mm lengths. The first stage was pumped by a fraction of the SHG output (gain: 10^4). Between the first and the second stage, the amplified signal was magnified by a 1:4.5 telescope. After the third stage, a final output energy of 1.39 mJ is obtained (gain: 58 in the second stage and 2 in the third stage). Published in [3].

seeder for the OPCPA around 800 nm and for the Yb-based pump amplifier at 1030 nm central wavelength. Stretching of the signal pulses was achieved by a fused silica prism pair, introducing negative group velocity dispersion, β_2. This negative chirp pre-compensated the positive β_2 within the OPCPA signal path. The total amount of dispersion introduced by the 8.5 mm of BBO, 10 m of air and 23.6 mm of glass was calculated by expanding the spectral phase around the carrier frequency, $\omega_c = 2.36\,\mathrm{PHz}$ ($\lambda_c = 800\,\mathrm{nm}$), up to the sixth order:

$$\varphi(\omega)|_{\omega_c} = \varphi(\omega_c) + \sum_{n=1}^{N=6} \frac{\beta_n}{n!} (\omega - \omega_c)^n, \tag{4.1}$$

with the dispersion coefficients, $\beta_n = \mathrm{d}^{(n)}\varphi(\omega)/\mathrm{d}\varphi(\omega)^{(n)}|_{\omega_c}$. The higher-order phase contribution of each optical element within the signal path is listed in Table 4.2. While the prism pair compensated β_2, it added higher-order dispersion. For an accurate phase compensation, a liquid-crystal spatial-light modulator (SLM, Jenoptik SLM-S640) was placed in the focused Fourier-plane of the prism pair. During the propagation along the signal path, the pulses were gradually compressed. After stretching to about 950 fs (at $1/e^2$ intensity), the calculated pulse duration after the first, second and third OPCPA stage was about 730 fs, 520 fs and 360 fs, respectively. After the third stage, the dispersion of an additional 6 mm fused silica bulk compressor leads to a pre-compression of about 170 fs. The final compression can be achieved by a pair of positively chirped mirrors ($\beta_2 = +200\ \mathrm{fs}^2$) in vacuum [3].

optical element	β_2 (fs^2)	β_3 (fs^3)	β_4 (fs^4)	β_5 (fs^5)	β_6 (fs^6)
prism pair ($l_\mathrm{P} = 2$ m)	-2172	-3297	-11297	10088	-51562
glass (23.6 mm)	862	652	-264	751	-2183
air (10 m)	215	108	-1	-202	592
BBO (8.5 mm)	653	461	-93	437	-1020
glass comp. (6 mm)	219	165	-68	211	558
chirped mirrors	200	0	0	0	0
residual	22	-1911	-11723	11285	-53615

Table 4.2 Dispersion Management of the signal path. The higher-order spectral phase contribution, $\beta_i, i = 2..6$, of different optical elements is listed. The residual phase is compensated by the spatial light modulator in the prism stretcher setup.

The dispersion management of the setup was tested experimentally using a different oscillator (Femtolasers Rainbow). Its spectrum is shown in Fig. 4.4a (orange), spanning a range of 689–968 nm. The pulse duration after the glass compressor was measured with SPIDER (device: Venteon Pulse:Four SPIDER). The reconstructed spectrum (grey dashed) from the SPIDER signal coincides with the measured spectrum, indicating that all spectral components were within the compressed part of the pulse. The retrieved phase (blue) is expressed in terms of the group delay, $GD = \mathrm{d}\varphi/\mathrm{d}\omega$, and indicates a small amount of residual higher-order phase, compared to the FOURIER-limited (FL) group delay (black dashed), with $GD(\lambda) = 0$. The corresponding retrieved intensity envelope (orange) is calculated by FOURIER-transformation (Fig. 4.4b) and features a pulse duration of 8.4 fs FWHM. For comparison, the FOURIER-limited intensity envelope (grey dashed) features a pulse duration of 8.0 fs FWHM.

For seeding the pump amplifier chain of subsequent Yb-based amplifiers, the 1030 nm pulses were stretched to 2.26 ns in an Öffner-type stretcher [175]. The first was an Yb:glass

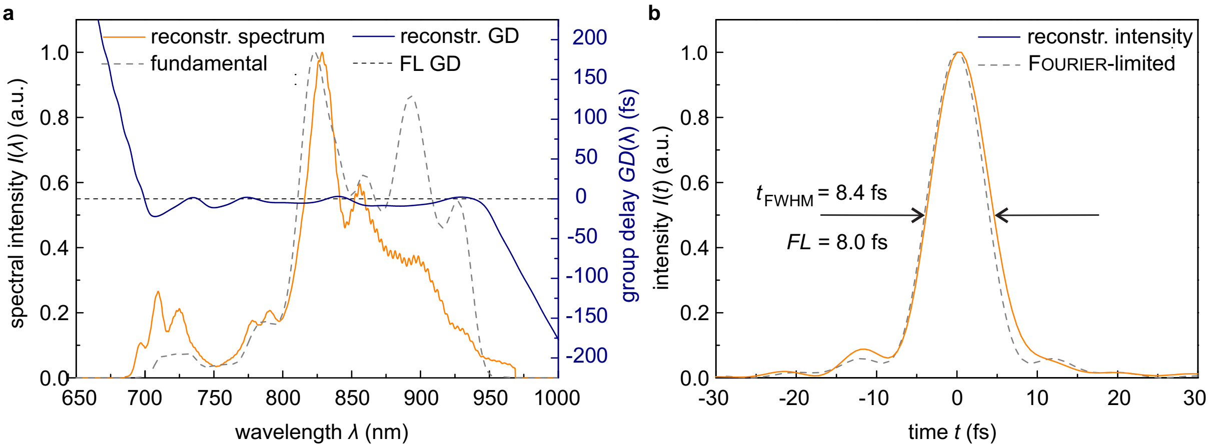

Figure 4.4 SPIDER pulse duration measurement used to test the dispersion compensation scheme with a broadband oscillator (Femtolasers Rainbow). (**a**) Fundamental oscillator spectrum (orange), reconstructed spectrum from the SPIDER signal (grey dashed), reconstructed phase in terms of group delay, $GD(\lambda)$ (blue), FOURIER-limited phase, $\varphi = 0$ (black dashed). (**b**) Retrieved intensity envelope (orange) after FOURIER-transformation (orange), FOURIER-limited intensity envelope (grey dashed).

fiber amplifier[2], delivering 0.36 mJ at 1030 nm. The second was an Yb:YAG Innoslab amplifier[3] [162, 163, 176]. The pump amplifiers used in this prototype system were operated in a 10 Hz burst-mode with 27.5 kHz intra-burst repetition rate. During a 0.8 ms lasting burst, the CPA system delivered 22 pulses in one burst, each with a pulse energy of 13.2 mJ and a pulse duration of 1.39 ps FWHM [3]. For the frequency doubling, a 2 mm BBO was used (type I phase-matching, $\theta = 23.4°$). OPCPA pump pulses with 6.8 mJ pulse energy were generated at 515 nm. In Fig. 4.5a, the achieved conversion efficiency, η_{SHG}, is plotted in dependence on the fundamental pump pulse energy, with a maximum of $\eta_{\text{SHG}} = 51.1\%$. In Fig. 4.5b the intensity autocorrelations of the fundamental and the second-harmonic pulses are shown. The fundamental autocorrelation width is $\tau_{\text{AC}(1030)} = 1.96$ ps FWHM, corresponding to a fundamental pulse duration of 1.39 ps FWHM. The SHG autocorrelation width is $\tau_{\text{AC}(515)} = 1.39$ ps FWHM, corresponding to an SHG pulse duration of 0.98 fs FWHM (autocorrelator: APE Pulse Check 50). The first OPCPA stage was pumped with a fraction of the pump beam (360 µJ). The pump beam diameter was 1 mm (at $1/e^2$ intensity) to reach the pump intensity of 81 GW cm^{-2} within the 3.3 mm BBO. The signal beam diameter was 1.3 mm. The signal pulses were amplified from about 1 nJ to 12 µJ, corresponding to a gain of $g = 1.2 \times 10^4$. The signal beam diameter, after amplification, was 1.1 mm due to spatial gain narrowing [3].

A high level of amplified optical parametric fluorescence (AOPF) is expected from the first stage, because of the high gain of $g \approx 10^4$ and the comparably low seed energy of $E_{\text{S}} \approx 1$ nJ. The AOPF can reach a significant intensity, which may be further amplified in the second OPCPA stage [177]. The power contrast between AOPF and OPCPA in the first stage was investigated to evaluate an upper limit for the AOPF that seeds the second OPCPA stage. The experiment was performed using a fiber-pumped OPCPA, pumped in continuous-mode at 20 kHz pulse

---

[2] provided by the Institute of Applied Physics in Jena, Germany

[3] commercial product from Amphos GmbH in Aachen, Germany. The used amplifier was capable of delivering about 500 W of output power in continuous operation as well as in burst-operation with about 500 W intra-burst power

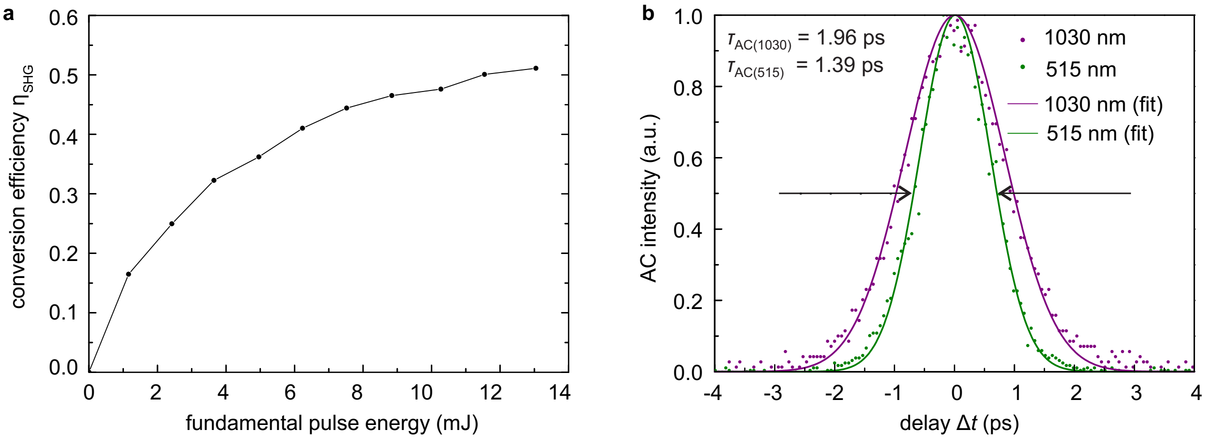

Figure 4.5 Second harmonic generation of the compressed Yb:YAG Innoslab pulses. (**a**) Conversion efficiency, η_{SHG}, from 1030 nm fundamental to 515 nm SHG. A maximum of 51.1% is achieved. (**b**) Intensity autocorrelation of the fundamental (violet dots) and the SHG (green dots) with the corresponding Gaussian fits (solid lines). The fundamental autocorrelation width is $\tau_{\text{AC}(1030)} = 1.96\,\text{ps}$ FWHM, corresponding to a fundamental pulse duration of 1.39 ps FWHM. The SHG autocorrelation width is $\tau_{\text{AC}(515)} = 1.39\,\text{ps}$ FWHM, corresponding to an SHG pulse duration of 0.98 fs FWHM.

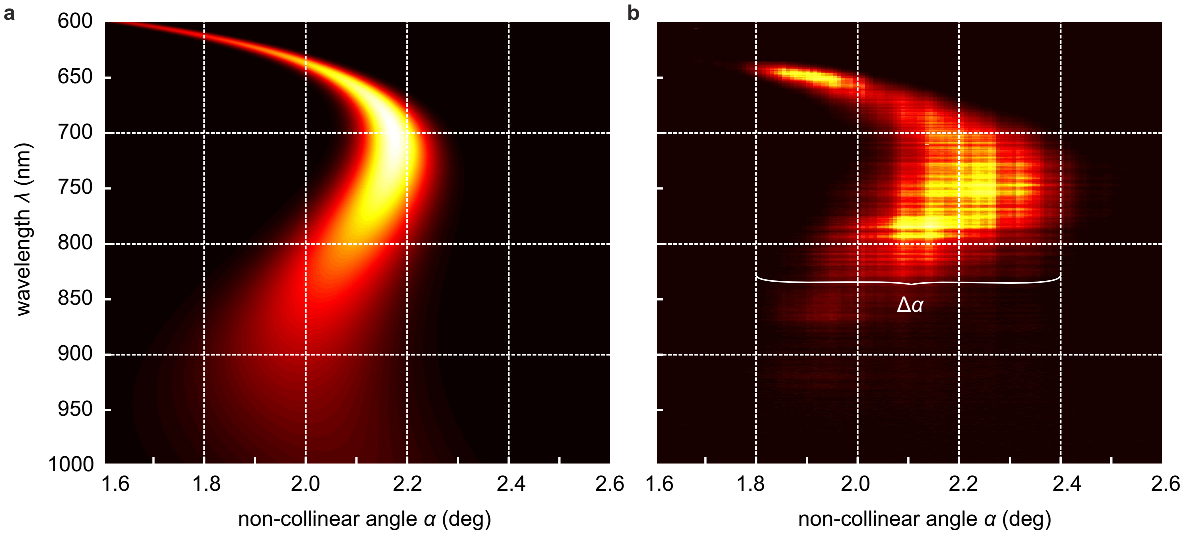

Figure 4.6 Spectral distribution of amplified optic parametric fluorescence along different internal non-collinear angles, α. (**a**) Calculated spectral gain for type I tangential phase-matching in BBO, pumped at 515 nm. The phase-matching angle is $\theta = 24.05°$. (**b**) Measured spectral intensity of the amplified optical parametric fluorescence (AOPF) at different internal non-collinear angles α. The internal opening angle of the cone was $\Delta\alpha = 0.6°$.

repetition rate (1.6 W at 515 nm) at a pump intensity of 100 GWcm^{-2}. The achieved OPCPA output power was 46 mW (corresponding to $E_{\text{sig}} = 2.3\,\mu$J pulse energy). After measuring the OPCPA output power, the signal beam was blocked, and the AOPF half-cone along the tangential phase-matching direction was measured. The cone was focused onto a calibrated photodiode (Thorlabs DET10A). The measured AOPF energy within the amplified signal area was 2.6 nJ. The corresponding AOPF-to-OPCPA energy contrast of $E_{\text{AOPF}}/E_{\text{sig}} \approx 10^{-3}$ represents an upper limit. The AOPF divergence angle was $\theta = 0.5°$. Thus, after a propagation distance of $z = 1.5$ m to the second stage, an upper limit for the AOPF-to-OPCPA intensity contrast could be estimated according to

$$\frac{I_{\text{AOPF}}}{I_{\text{OPCPA}}} = \frac{E_{\text{AOPF}}}{E_{\text{sig}}} \cdot \frac{w_{\text{sig}}^2}{(z \tan \Theta)^2} \cdot \frac{\tau_{\text{sig}}}{\tau_{\text{AOPF}}} \approx 10^{-5}. \tag{4.2}$$

where, $\tau_{\text{sig}} = 730$ fs is the pulse duration of the signal after the first stage (at $1/e^2$ intensity, calculated), and $\tau_{\text{AOPF}} \approx 1.7$ ps is the pulse duration of the AOPF (at $1/e^2$ intensity, assumed equal to the measured pump pulse duration). The AOPF divergence angle was determined by measuring the fluorescence spectrum in dependence on the internal non-collinear angle, α (see Fig. 4.6b). For comparison, the expected spectral gain is calculated analytically (Fig. 4.6a). For the measurement, an aperture with 200 µm diameter was moved along the α direction within the phase-matching plane. It was mounted onto a multi-mode fiber-bundle coupled to a grating spectrometer (Shamrock SR-303i-B with Andor iDus DV420A-OE detector). The measurement shows a qualitative agreement with the calculation for a phase-matching angle of $\theta = 24.05°$. From Fig. 4.6b, the internal opening angle of the cone, $\Delta\alpha \approx 0.6°$, was measured, yielding the external divergence angle of $\Theta = 0.5°$ (half angle[4]). With a contrast of $< 10^{-5}$, negligible AOPF is expected from the final amplifier stages, because the AOPF is quenched by the presence of the seed signal [3].

The second OPCPA stage (a 3.2 mm long BBO crystal) was pumped at 6.4 mJ with a beam diameter of 3.7 mm (at $1/e^2$ intensity), yielding an intensity of 105 GW cm^{-2}. Between the first and the second stage the signal beam was expanded by a 1:4.5 telescope to a diameter of 5.0 mm. The signal was amplified with a gain of $g = 58$ to a pulse energy of 0.7 mJ, corresponding to a total pump-to-signal conversion efficiency of 10% [3]. An additional gain of $g = 2$ was achieved by exploiting the residual pump energy using a third OPCPA stage (a 2 mm BBO). Efficient energy extraction was achieved by fine-tuning the delay between pump and signal pulses within the second and the third OPCPA stage. The stable operation of the three-stage non-collinear OPCPA could only be achieved when the laboratory conditions remained stable. Under stable temperature and humidity conditions, we measured an energy deviation of $\Delta E/E < 0.7\%$ rms over a period of 30 minutes [3]. A total pulse energy of 1.39 mJ was achieved, corresponding to a final pump-to-signal conversion efficiency of 20%. Thus, from the compressed 1030 nm pulses to the amplified broadband OPCPA pulses a total conversion efficiency of 10% could be demonstrated. The overall efficiency was 7.7%, derived from the uncompressed output,

$$17.6\,\text{mJ} \xrightarrow{\text{comp. }75\%} 13.2\,\text{mJ} \xrightarrow{\text{SHG }51.1\%} 6.8\,\text{mJ} \xrightarrow{\text{OPCPA }20\%} 1.4\,\text{mJ}. \tag{4.3}$$

In Fig. 4.7 the broadband signal spectra of the oscillator (grey shaded), after the second (blue line) and third (orange line) OPCPA stage are plotted. The amplified bandwidth is $\Delta\nu =$

---

[4] Here, $\Delta\alpha$ is the full angle inside the BBO, whereas Θ is the divergence (half) angle after refraction.

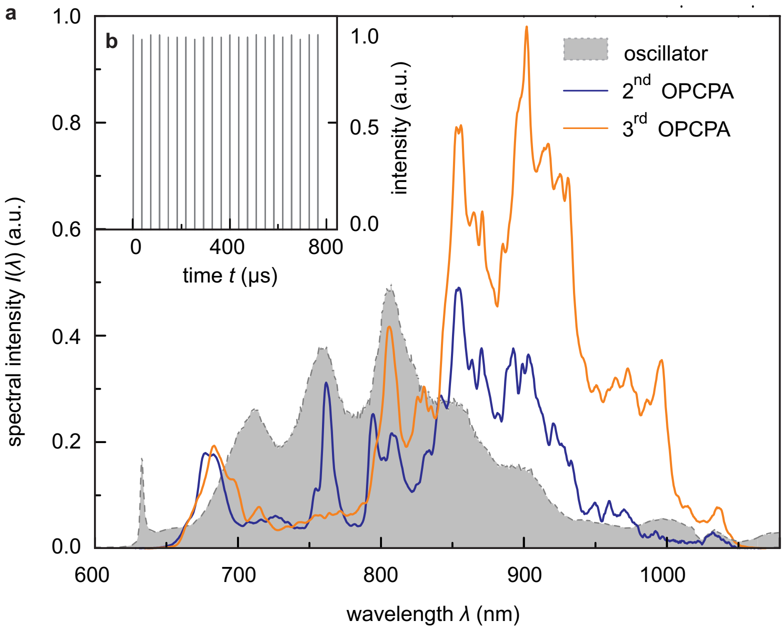

Figure 4.7 Amplified spectral bandwidth of the three-stage OPCPA. Spectral intensity of the Ti:sapphire oscillator (grey shaded), amplified spectra after the second (blue line) and the third OPCPA stage (orange line). The amplified spectral bandwidth is $\Delta\nu = 168\,\mathrm{THz}$ at $1/e^2$ ($\Delta\lambda = 360$ nm at $\lambda_c = 800$ nm), featuring a Fourier-limited pulse duration of 6.4 fs. **Inset:** Typical pulse train during the burst-mode operation. Published in [3]

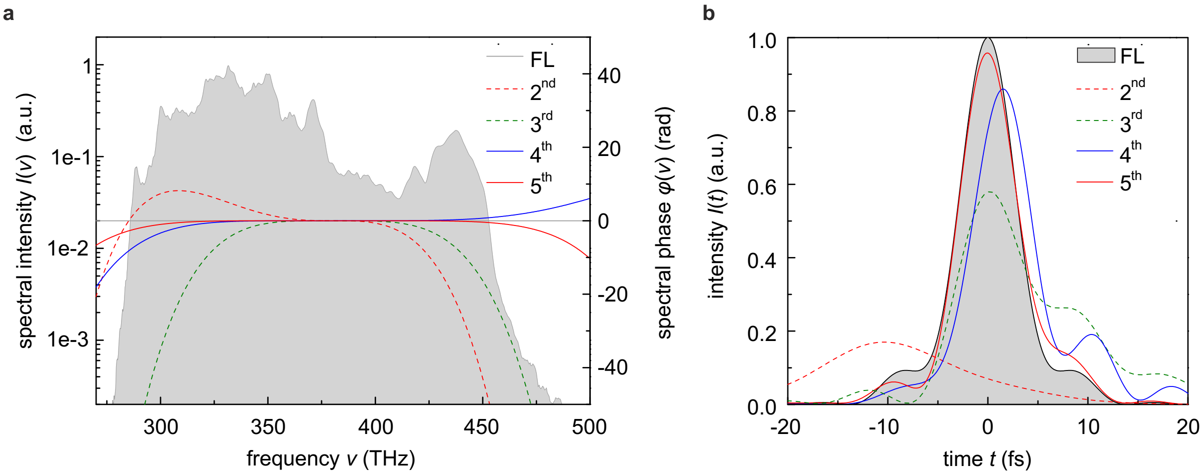

Figure 4.8 Evaluation of the compressible pulse duration. (**a**) Amplified spectrum and spectral phase for different compensated higher-order dispersion terms: $\beta_2 = 0$, $\beta_{3,4,5,6} \neq 0$ (red dashed); $\beta_{2,3} = 0$, $\beta_{4,5,6} \neq 0$ (green dashed), $\beta_{2,3,4} = 0$, $\beta_{5,6} \neq 0$ (blue); $\beta_{2,3,4,5} = 0$, $\beta_6 \neq 0$ (red) and the Fourier-limit (FL, grey). (**b**) Corresponding calculated pulse shapes. Pulse durations FWHM: 6.4 fs (FL=Fourier limited), 19.2 fs (2nd order), 8.7 fs (3rd order), 6.7 fs (4th order), 6.5 fs (5th order).

168 THz at $1/e^2$ ($\Delta\lambda = 360$ nm at $\lambda_c = 800$ nm). A typical amplified burst of 22 pulses is presented in Fig. 4.7 (inset). A FOURIER-transformation was carried out in order to evaluate the compressibility. In Fig. 4.8a, the amplified spectrum (grey shaded) after the third stage and the spectral phase from the dispersion management (Table 4.2) is plotted in dependence of frequency. Different orders of dispersion are considered to be compensated, $\beta_2 = 0$, $\beta_{3,4,5,6} \neq 0$ (red dashed); $\beta_{2,3} = 0$, $\beta_{4,5,6} \neq 0$ (green dashed), $\beta_{2,3,4} = 0$, $\beta_{5,6} \neq 0$ (blue); $\beta_{2,3,4,5} = 0$, $\beta_6 \neq 0$ (red) and the Fourier-limit (FL, grey). The corresponding pulse shapes are plotted in Fig. 4.8b with achieved FWHM pulse durations of 19.2 fs (red dashed), 8.7 fs (green dashed), 6.7 fs (blue dashed), 6.4 fs (red) and 6.4 fs (Fourier-limit). The calculation shows that reaching the sub-7 fs regime requires dispersion compensation at least up to the fourth order. Experimentally, the nonlinear spectral phase added by the OPCPA also needs to be taken into account [178].

4.4 Passive pump-to-seed overlap stabilization

With ultrashort pump pulses in the picosecond range a major technological challenge arises, because the OPCPA output stability is highly sensitive to the temporal overlap between pump and signal pulses within the amplifier crystals. According to numerical simulations of a non-collinear OPCPA, the pump-to-signal delay must be kept below $|\Delta t| < 50$ fs to not exceed an energy deviation of $\Delta E/\Delta t < 1\%$ [3]. Within this temporal window, also the spectral bandwidth decreases by about 1% of the maximum bandwidth. All-optical synchronization of the pump and signal pulses was introduced in order to avoid additional active electronic synchronization of two master oscillators [179–181]. But the remaining path length drift in the pump CPA causes instabilities on the long-term scale within tens of seconds to minutes [182]. The total optical path in the pump laser is about > 150 m. Environmental changes in the laboratory, such as drift of the temperature, the air pressure and the humidity may cause a delay on the order of 50 fs and more. Under stable conditions, the developed three-stage OPCPA prototype could be operated with reasonable stability for at least 30 minutes. During long-term operation, a considerable drift of the pump-to-seed timing occurred. This could change the average output energy and the spectral bandwidth by up to 50%. The development of reliable pump-to-signal synchronization techniques required for a long-term stable operation of large-scale OPCPA systems [3].

Different synchronization approaches were developed so far. In the active synchronization approach, the occurring delay drift between the pump path and the signal path, Δt, can be measured with various techniques. The Δt-signal is then fed back to a proportional-integral-derivative (PID) control loop driving an optical delay line in one of the optical paths. The measurement techniques are, for example, a balanced optical cross-correlator (BXC) [3, 181, 183], spectral variations of the intensity cross-correlation [182], determination of the spectral center of gravity (COG) of the OPCPA output [3], and measuring the power content in different regions of the angularly dispersed idler [184].

This part of the work is dedicated to the development of a passive synchronization technique that is based on white-light supercontinuum generation (WLG) as broadband source for seeding the high-power OPCPA, pumped by sub-ps pulses [2, 92, 97, 165]. In this scheme, WLG pulses are generated using a fraction of the pump CPA system to provide intrinsically synchronized seed pulses. Because the pump and seed pulses are split after the pump CPA, the residual optical path to the OPCPA stages is minimized (about 2–4 m). The WLG seeding was originally developed to provide broadband seed pulses for OPA systems pumped by sub-100 fs Ti:sapphire amplifiers [88]. However, sapphire, the medium of choice for OPCPA seeding requires sub-

100 fs pulses to achieve a stable WLG. As discussed already in Section 2.4.4, pulse durations in the sub-ps range are not sufficient for an efficient multi-photon ionization (MPI), which must be the dominant process for the free-electron generation during the filamentation. It has been found that laser host materials, such as yttrium-aluminum-garnet (YAG), are suitable crystals for WLG pumped with sub-ps pulses [92]. They have a large nonlinear refractive index, enabling a lower required critical power, P_{crit} (Eq. 2.50), for self-focusing. Owing to their smaller band-gap compared to sapphire, a lower-order multiphoton absorption is required, resulting in a higher multiphoton ionization (MPI) rate.

4.4.1 Supercontinuum-generation in laser host materials

Different laser host materials were used to investigate the spectral broadening from white-light continuum generation: yttrium-aluminum-garnet (YAG[5]), Yb-doped potassium-gadolinium tungstate (Yb:KGW[6]), Yb-doped potassium-yttrium-tungstate (Yb:KYW[7]), and Yb-doped yttriumorthovanadate (Yb:YVO$_4$[8]). The pump pulses were provided by an Yb:glass fiber amplifier at a central wavelength of $\lambda_c = 1030\,\mathrm{nm}$ and a pulse duration of 850 fs and focused into the crystal with an $f = 100\,\mathrm{mm}$ lens. The pulse energy and the numerical aperture, NA, were optimized for a stable continuum generation in the different crystals (10 mm YAG: 7.8 µJ, $NA = 0.02$; 8 mm Yb:KGW: 6.6 µJ, $NA = 0.02$; 8 mm Yb:KYW: 2.5 µJ, $NA = 0.02$; 8 mm Yb:YVO$_4$: 5.2 µJ, $NA = 0.006$). After the crystal, the WLG beam was recollimated with a focusing mirror of $f = 100\,\mathrm{mm}$ and spectrally filtered by a high-pass mirror (reflective for $\lambda < 900\,\mathrm{nm}$). In Fig. 4.9, the measured spectra of the blue-shifted part, $\Delta\omega_+$, are presented. The broadest spectral width is achieved in the YAG crystal, with a spectral cut-off at 470 nm. In comparison, the spectrum generated in Yb:YVO$_4$ has the cut-off already at 570 nm. The spectra of YAG and Yb:YVO$_4$ feature a plateau-like region between 750 nm and 900 nm and a maximum at 620 nm (YAG) and 700 nm (Yb:YVO$_4$), respectively. The same plateau is observed for Yb:KGW, but the maxima obtained from the tungstates (Yb:KGW, Yb:KYW) are accompanied by almost symmetric side-maxima, that are expected to originate from further involved non-linear processes, such as RAMAN-scattering and four-wave-mixing [98]. In Table 4.3, the nonlinear refractive index, n_2, the optical band-gap, E_{gap}, and the measured cut-off wavelength are listed. An increasing E_{gap} comes along with a smaller n_2, but the cut-off increases to higher frequencies, corresponding to a larger continuum bandwidth. For the development of the intrinsic pump-to-signal synchronization for a high-power OPCPA, YAG was chosen as the WLG material, because it features the largest bandwidth. The other materials are also interesting, but in this work they were not investigated regarding the long-term stability.

4.4.2 Optical parametric amplification of supercontinuum pulses

An OPCPA was realized in order to investigate the feasibility for amplification and temporal compression of sub-ps pumped WLG pulses generated in YAG. In Fig. 4.10, a schematic of the experimental setup is shown. The compressed output pulses from the Yb:glass fiber CPA (operated at a repetition rate of 20 kHz) were separated in a beam-splitter (BS). The larger fraction

---

[5] $Y_3Al_5O_{12}$,

[6] Yb^{3+}:KGd(WO$_4$)$_2$

[7] Yb^{3+}:KY(WO$_4$)$_2$

[8] Yb^{3+}:YVO$_4$

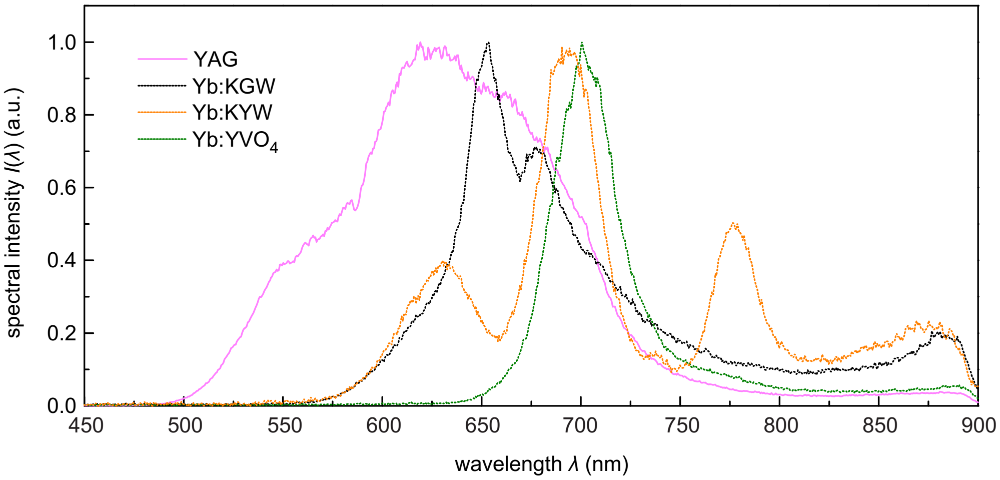

Figure 4.9 White-light continuum generation in laser host materials, pumped by a fiber laser with $\lambda_c = 1030$ nm and 850 fs pulse duration. The blue-shifted part is spectrally filtered by a high-pass mirror (cut-off wavelength 900 nm). The plot shows the spectra generated in YAG (red), Yb:KGW (black), Yb:KYW (orange) and Yb:YVO$_4$ (dark green).

	Sapphire	YAG	Yb:KGW	Yb:KYW	Yb:YVO$_4$
n_2 (10^{-16} cm^{2}W^{-1})	3.1^d	6.9^d	10^d	8.6^b	15^b
E_{gap} (eV)	8.2^a	5.9^d	4.0^c	4.3^b	3.7^b
cut-off (nm)	(190)^d	470	560 (500)^d	540	580

a deduced from the manufacturer's transmission cut-off at 8.2 eV (Thorlabs).
b from [185].
c from [186].
d value reported in [92].

Table 4.3 The nonlinear refractive index, n_2, the optical band-gap, E_{gap}, and the cut-off wavelength of the blue-shifted part of the measured WLG spectrum in different materials. Sapphire is listed for comparison.

was frequency-doubled (SHG) in a 1 mm BBO crystal with type-I phase-matching, generating OPA pump pulses at $\lambda_c = 515\,\text{nm}$ with a pulse energy of 200 µJ. The smaller fraction was used for WLG. An aperture (AP) and an $f = 100\,\text{mm}$ focusing lens were used to adjust the numerical aperture $NA = 0.02$. The pulses were focused into a 10 mm long YAG crystal with a pulse energy of 10 µJ. The focus was placed close to the input surface of the crystal. In Fig. 4.11a, the short-term energy stability of the full WLG spectrum is shown, measured over a period of 60 s. The energy jitter was $\Delta E_{\text{WLG}}/E_{\text{WLG}} = 1.6\%$ rms (measured with an Ophir PD10-PJ-SH-V2). The corresponding beam profile after the aperture is shown in the inset (Fig. 4.11b). The beam profile measurement shows a radial-symmetric GAUSSIAN intensity distribution. The spectral stability is demonstrated in Fig. 4.11c, where the spectral intensity (colored logarithmic scale) is measured over a period of 10 minutes (Spectrometer: Andor Shamrock 303 spectrograph with iDus CCD). A single WLG spectrum is shown in Fig. 4.11d (grey shaded).

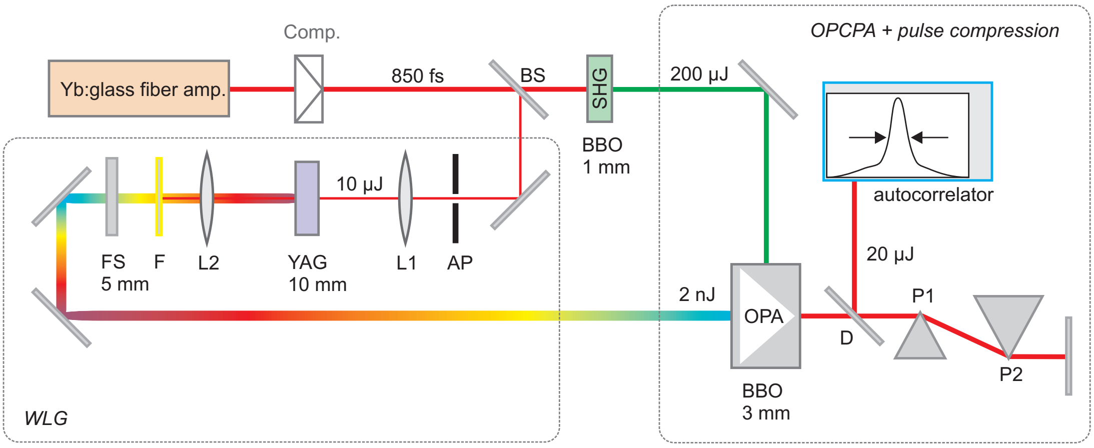

Figure 4.10 Experimental setup of the WLG-seeded OPCPA. Yb:glass fiber amplifier: 850 fs pulse duration. The pulses were split after the compressor using a beam-splitter (BS). SHG: frequency-doubling in a 1 mm BBO crystal with type-I phase-matching for OPA pumping at $\lambda_c = 515\,\text{nm}$ and 200µJ pulse energy. AP: aperture for NA adjustment. L1: focusing lens of $f = 100\,\text{mm}$. YAG: 10 mm YAG crystal for WLG pumped with a pulse energy of 10µJ at numerical aperture $NA = 0.02$. L2: recollimation lens of $f = 100\,\text{mm}$. F: notch-filter for blocking 1030 nm pump beam. FS: fused silica, 5 mm, for pulse stretching. OPA: 3 mm BBO with type-I phase-matching, output energy 20 µJ. D: D-shaped mirror. P1,P2: prism pair for temporal compression ($\overline{\text{P1P2}} = 1.15\,\text{m}$). The compressed pulses were characterized with an intensity-autocorrelator.

The single stage non-collinear OPCPA consisted of a 3 mm BBO with type-I phase matching. The WLG seed energy was about 2 nJ. The temporal stretching was achieved by positive GDD of about 10 mm YAG and 8 mm fused silica (lens, filter, fused silica plate). At a repetition rate of 20 kHz, the WLG pulses were amplified to a pulse energy of (20 ± 0.22) µJ, corresponding to 400 mW average output power. From power stability measurements, a jitter of 1.1% rms is determined, measured over a period of 60 s (measured with an Ophir 3A-SH-ROHS). The amplified spectrum is plotted in Fig. 4.11d (red line), featuring a FOURIER-limited pulse duration of 6.4 fs. The pulse compression was achieved using a fused silica prism pair (P1,P2) with an apex distance of $\overline{\text{P1P2}} = 1.15\,\text{m}$, to compensate for the GDD introduced by the stretching and the 3 mm BBO ($\beta_2 = -1620\,\text{fs}^2$). The compression was characterized with an intensity autocorrelator (Femtolasers Femtometer). The autocorrelation signal is shown in Fig. 4.11e (inset), with an autocorrelation width of $\tau_{\text{AC}} = 35\,\text{fs}$ FWHM. This autocorrelation signal is typical

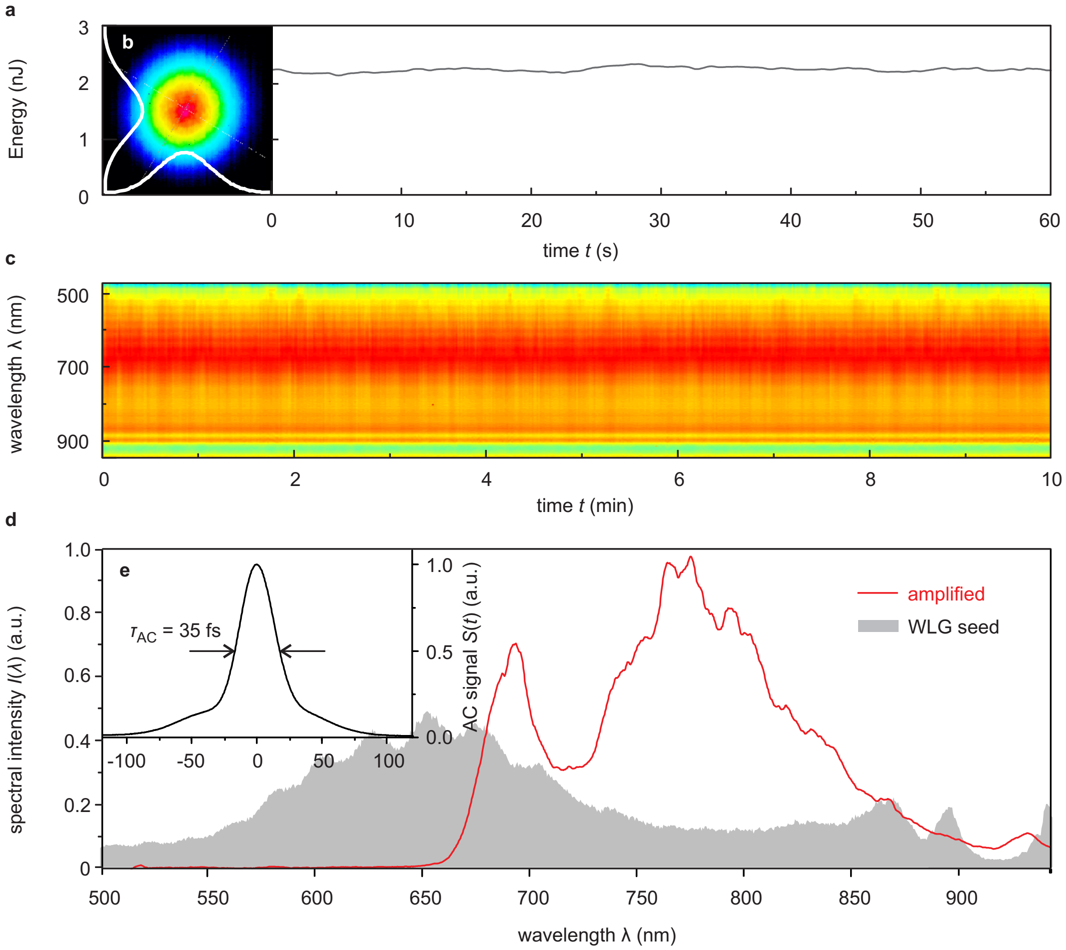

Figure 4.11 Experimental results of the WLG-seeded OPCPA. (**a**) WLG pulse energy after the filter, measured over 60 s with 1.6% rms energy jitter. (**b**) Inset: WLG beam profile. (**c**) Spectral stability: spectrum (colored logarithmic scale), measured over 10 min. (**d**) WLG seed spectrum (grey shaded) and amplified spectrum (red line). The modulations in the seed spectrum arise from the 1030 nm notch filter (**e**) Inset: autocorrelation (AC) signal with autocorrelation width $t_{AC} = 35$ fs. Published in [163].

for pulses with uncompensated third-order dispersion. Further compression was limited by the strong residual negative higher-order dispersion, that was mainly introduced by the prism pair ($\beta_3 = -1839\,\mathrm{fs}^3$ and $\beta_4 = -6200\,\mathrm{fs}^4$). This can be compensated by adaptive dispersion control or specially designed chirped mirrors [97]. During the operation, no drift of the OPCPA output energy or the spectrum was observed.

4.4.3 Long-term stability and intrinsic temporal jitter

The long-term stability of WLG in YAG was investigated using an experimental setup similar to the WLG-part of the setup described in Fig. 4.10. A different Yb:glass fiber amplifier was used for WLG pumping. The pulse duration was 378 fs at a repetition rate of 416.67 kHz. The pump pulses were focused into the crystal with a lens of $f = 50\,\mathrm{mm}$ and a numerical aperture of $NA \approx 0.02$. The focal point was placed close to the input surface within the crystal. The full WLG spectrum ranged from about 470 nm to beyond 1500 nm (see Fig. 2.5 on p. 26). A part of the spectrum (650 nm to 950 nm) was selected by use of dichroic filter mirrors. First, the short-term stability was investigated for different crystal lengths. The WLG spectrum was measured for a period of 10 minutes at a detector integration time of 10 ms (OceanOptics USB4000). In Fig. 4.12a, single spectra are shown for each crystal length, 2 mm (red), 3 mm (purple), 4 mm (brown), 5 mm (green), 6 mm (pink), and 10 mm (orange). For each crystal, the pulse energy and the focus position were adjusted to optimize the spectral cut-off and the pulse energy. The spectral intensity in the selected region (blue shaded) increases with increasing crystal length. This can be explained by the longer nonlinear interaction length that corresponds to a longer pulse propagation distance within the filament. For shorter crystals, the filament is stopped physically at the end-face of the crystal, whereas in the 10 mm crystal it finds its natural end. For the energy jitter evaluation, the measured spectra were (spectrally) integrated. The corresponding WLG pump energies (red) and the achieved rms energy jitter values (blue) are shown in Fig. 4.12b. For the 5 mm crystal, a jitter of $\Delta E_{\mathrm{WLG}}/E_{\mathrm{WLG}} = 0.8\%$ rms was achieved at a pump pulse energy of 1.8µJ. The energy of the generated white-light pulse was about $E_{\mathrm{WLG}} = 8\,\mathrm{nJ}$. These results indicate that the artificial interruption of a filament at the end of a certain crystal length leads to particularly stable WLG conditions. Using this configuration, the power stability of the fiber laser and the selected WLG output was measured over a period of 28 hours. The fiber laser stability was $\Delta P_{\mathrm{P}}/P_{\mathrm{P}} < 0.65\%$ rms (see Fig. 4.14a, black line, measured with calibrated Thorlabs DET10A photodiode). No significant drift of the WLG output power was measured (red line). The WLG power jitter was $\Delta P_{\mathrm{WLG}}/P_{\mathrm{WLG}} < 0.85\%$ (Ophir 3A power meter).

It was of particular interest whether the WLG process itself introduces a pump-to-signal timing jitter. A time delay, Δt, is expected for a variation of the pump pulse energy, ΔP_{P}. This is depicted in the left part of Fig. 4.13 (*WLG*). The pump pulse (light red, solid pulse) generates a filament (yellow) and a WLG pulse (red, solid pulse) at the trailing edge of its intensity envelope within the YAG. When the pump power is increased (light red, dotted pulse), the threshold power for self-focusing is achieved earlier and thus the onset of the filament (white, dashed) and the WLG (red, dotted pulse) is triggered earlier within the intensity envelope of the pump, introducing a pump-to-signal delay. Additionally, with increasing pump energy, the spatial position, z, of the filament shifts towards the input surface of the crystal [98, 100]. This introduces a difference in group delay, ΔGD, between pump and WLG pulses within the material. For example, between the 1030 nm pump and the 650 nm WLG the GD varies about $\Delta GD/\Delta z \approx 40\,\mathrm{fs/mm}$.

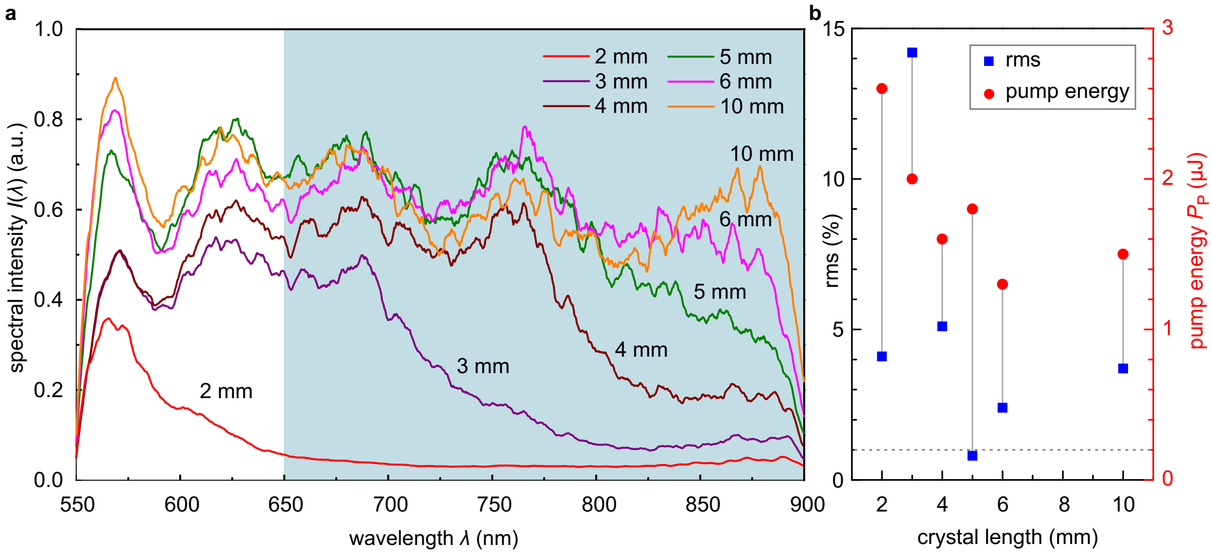

Figure 4.12 Evaluation of different YAG crystal lengths for an optimized WLG stability. (**a**) WLG spectrum achieved in YAG crystals of 2 mm (red), 3 mm (purple), 4 mm (brown), 5 mm (green), 6 mm (pink), and 10 mm (orange) length. The blue shaded area indicates the investigated spectral region. (**b**) Achieved WLG energy jitter in % rms (blue) and WLG pump energy (red) in dependence on the crystal length.

According to both mechanisms for a given pump energy jitter also a jitter of the pump-to-signal timing is expected.

To measure this delay, a two-crystal balanced optical cross-correlator (BXC) was used [183]. As depicted in the right part of Fig. 4.13 (*BXC*) a fraction of the 1030 nm pump pulse, $I_\mathrm{p}(t)$, was correlated with the WLG pulse, $I_\mathrm{WLG}(t)$. For the measurement, a spectral filter (F) was used to select the (650 ± 10) nm part of the WLG spectrum for the correlation. The two-crystal BXC consists of two correlator arms and two balanced photomultipliers (DET1, DET2, devices: Hamamatsu H6780). In the first arm, the intensity cross-correlation, $\int_{-\infty}^{+\infty} I_\mathrm{p}(t) I_\mathrm{WLG}(t-\Delta t)$, is measured by SFG in a type-I BBO ($\theta = 27.7°$). The sum-frequency signal at 399 nm was band-pass filtered (FB) for the detection. A group delay, *GD*, between pump and WLG pulses was introduced in the second correlator arm by using a 6 mm fused silica plate (FS), yielding the cross-correlation $\int_{-\infty}^{+\infty} I_\mathrm{p}(t) I_\mathrm{WLG}(t-\Delta t + GD)$. Measuring the difference voltage, $U = U_\mathrm{DET2} - U_\mathrm{DET1}$, between both detector signals yielded a background-free signal, which was insensitive to intensity fluctuations within the single correlator arms (green curve). The signal was proportional to the temporal delay in direction (sign) and amplitude, with a slope of $\Delta t / \Delta U = 6.67$ fs/mV [3].

The pump-to-WLG delay was measured in dependence of increasing pump energy. The measurement is presented in Fig. 4.14b. The onset of WLG was observed at pump energies of $E_\mathrm{P} \geq 1$ µJ. In this case, the position of the filament was at the end of the crystal. By increasing the pump energy to 1.47 µJ, an increase of the delay between pump and WLG of about 200 fs was measured. Further increase of the pump energy led to an oscillation of the delay. This is attributed to a sequence of plasma-defocusing and self-focusing within the crystal. Above a pump pulse energy of 1.9 µJ, the excessive energy was sufficient to form a second filament and thus a second WLG pulse. This pulse is delayed by about 160 fs with respect to the first WLG pulse, leading to stable interference modulations in the WLG spectrum [3].

The operation point for the stable generation of single WLG pulses was chosen slightly

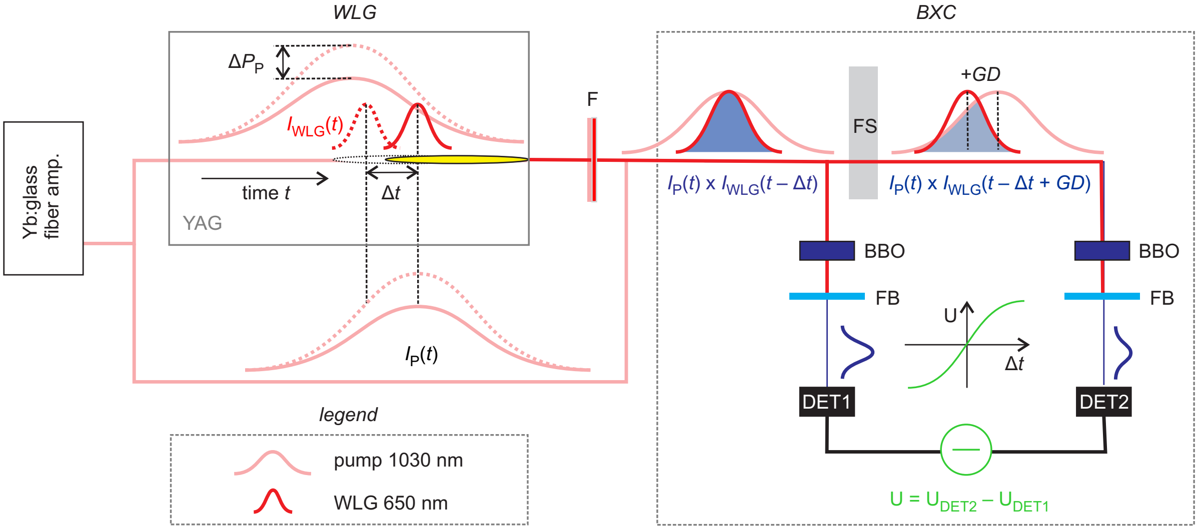

Figure 4.13 Experimental setup for the pump-to-WLG delay measurement. An Yb:glass fiber amplifier was used as the pump source (pulse duration: 378 fs). *WLG*: Within the YAG, a free-electron filament (yellow) and a corresponding WLG pulse (red, solid pulse) were generated at the trailing edge of the pump pulse (light red, solid pulse). With increasing pump power, ΔP_p, the WLG pulse was created earlier (white dotted filament, dotted pulses), leading to a delay, Δt, with respect to the first situation. *BXC*: Two-crystal balanced optical cross-correlator setup. The WLG pulse, $I_\mathrm{WLG}(t)$, was band-pass filtered (F) around 650 nm and correlated with a fraction of the pump pulse, $I_\mathrm{p}(t)$. In each BXC arm, the intensity cross-correlation was measured by SFG in a type-I BBO ($\theta = 27.7°$). The SFG signal at 399 nm is band-pass filtered (FB) and detected with a photomultiplier (DET1, DET2). A 6 mm fused silica plate (FS) introduced a group delay ($+GD$) in the second arm. The difference voltage, $U = U_\mathrm{DET2} - U_\mathrm{DET1}$, was proportional to the temporal delay.

below the onset of the second filament at $E_P \approx 1.8\,\mu J$, as indicated by the blue region in Fig. 4.14b. The delay within this region varied by $\Delta T/\Delta E_P = (0.66 \pm 0.4)\,fs/nJ$. Multiplication with the energy deviation of the pump (Fig. 4.14a) yields a good estimate of the intrinsic timing jitter of the continuum seeder (Fig. 4.14c), yielding $\delta t = (7.0 \pm 0.5)$ fs rms (16 fs FWHM) [3].

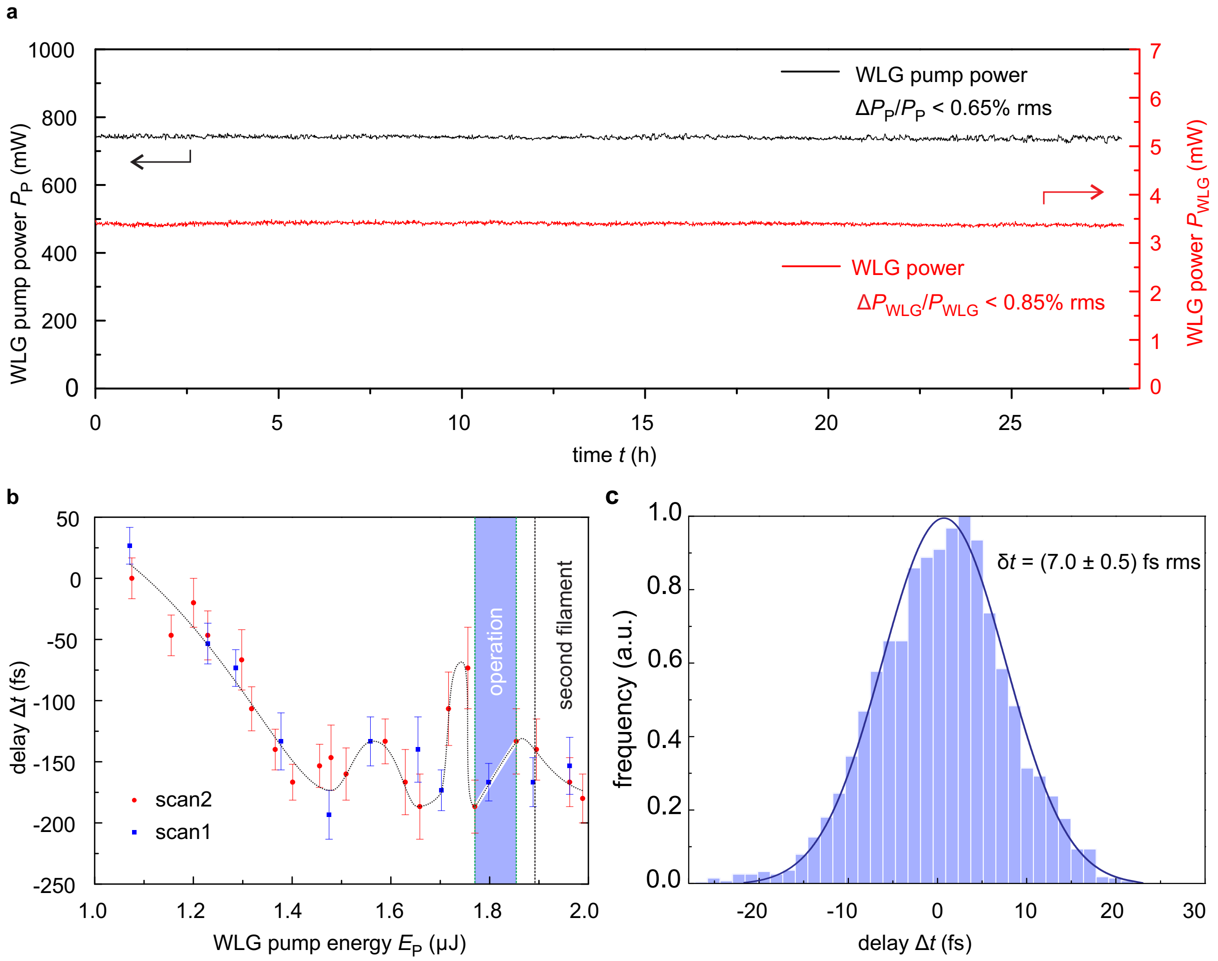

Figure 4.14 Long-term stability and intrinsic temporal jitter from WLG. (**a**) Pump power (black) and WLG power (red), measured over 28 hours. The power deviation is smaller than 0.65% rms for the pump and 0.85% rms for the WLG power. The investigated WLG spectral region ranged from 650 nm to 950 nm. (**b**) Delay between pump and WLG pulses at different pump pulse energies, measured with a balanced cross-correlator. The blue region indicates the operation regime (about 1.8 μJ). Above 1.9 μJ a second WLG pulse is generated (dashed line). Within the operation regime, the delay varied with a slope of $\Delta T/\Delta E_P = (0.66 \pm 0.04)\,fs/nJ$. (**c**) Pump-to-WLG delay jitter, derived from the pump jitter in (a) and the slope from the operation regime in (b), $\Delta t = E_P(t) \cdot \Delta T/\Delta E_P$. The rms width is $\delta t = (7.0 \pm 0.5)$ fs. Published in [3].

4.5 OPCPA at high average powers

Optical parametric chirped-pulse amplifiers can reach high average powers without sophisticated cooling. With average powers in the kilowatt range, thermal effects play an important role in OPCPA, even though the absorption of the nonlinear crystals is very low compared to a conventional active laser material. In this section, the thermal effects are evaluated to estimate the scalability for future high power OPCPA systems.

4.5.1 Absorption of signal, idler and pump

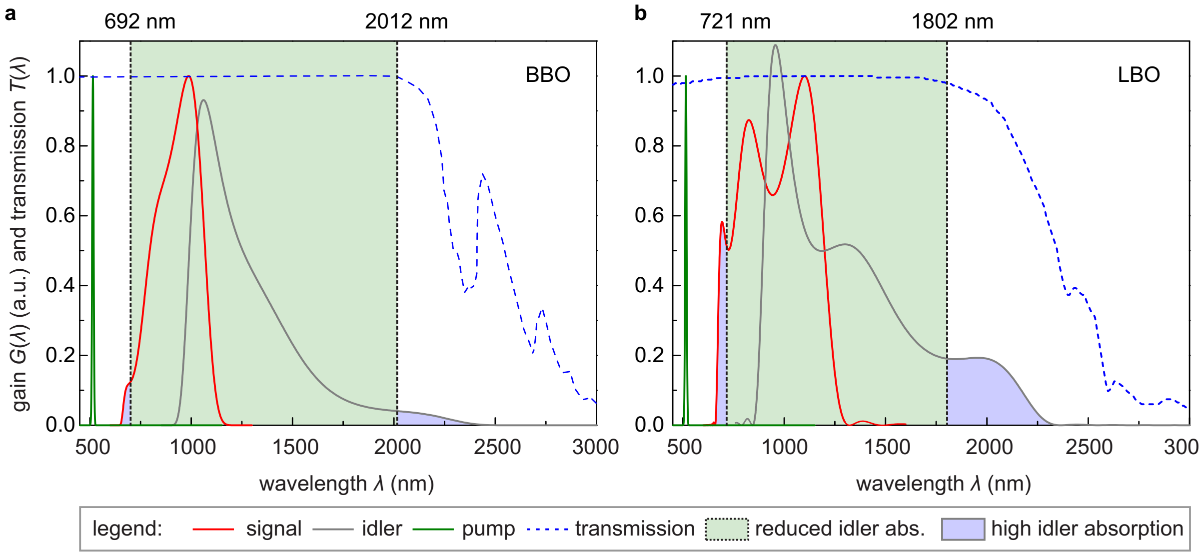

Figure 4.15 Evaluation of the idler-absorption in OPCPA. The signal (red line) and idler gain (grey line) is calculated in dependence on the wavelength and compared with the wavelength-dependent transmission (blue dashed line). In order to avoid strong idler absorption during the amplification, the signal must be spectrally filtered, as indicated by the green box. The blue-shaded areas indicate the signal-idler frequency pairs that are clipped. (**a**) BBO: idler components with $\lambda_{\mathrm{id}} > 2012\,\mathrm{nm}$ are avoided by cutting signal components with $\lambda_{\mathrm{s}} < 692\,\mathrm{nm}$. (**b**) LBO: idler components with $\lambda_{\mathrm{id}} > 1802\,\mathrm{nm}$ are avoided by cutting signal components with $\lambda_{\mathrm{s}} < 721\,\mathrm{nm}$. The pump spectrum at 515 nm is also plotted (green line).

A realistic estimate of heat development in a high average power pumped OPCPA system is difficult. First of all, the linear absorption of the pump wavelength (515 nm) strongly depends on the crystal quality. This leads to large differences not only between different manufacturers, but also between different batches from the same manufacturer. Second, also the absorption of the signal and the idler during the amplification process needs to be evaluated. In Fig. 4.15, the spectral regions of the pump (green line), the signal (red line) and the idler (grey line) are compared with the spectral transmission, $T(\lambda)$ (blue dashed line) for BBO (a) and LBO (b). The signal and idler spectra are represented by the gain curve, $G(\lambda)$ calculated according to Eqs. (2.30). The pump absorption is addressed by taking the commonly available literature values of the absorption coefficient, $\alpha_{\mathrm{BBO}} = 1\%\mathrm{cm}^{-1}$ and $\alpha_{\mathrm{LBO}} = 0.3\%\mathrm{cm}^{-1}$, as listed in Table 4.1. Because these may differ by at least one order of magnitude, the following evaluation only gives an estimate for the thermal effects in OPCPA. The second problem is addressed by neglecting the absorption of the signal, because it is well within the high transparency window in both crystals and its power is also a factor of 5–10 lower than the pump power. The idler, however, approaches the mid-infrared region, where the absorption reaches considerable values due to molecular resonances. Strong absorption can be prevented, if the idler spectrum is limited to $\lambda_s < 2012\,\text{nm}$ in BBO and $\lambda_s < 1802\,\text{nm}$ in LBO. At these wavelengths, the idler absorption equals the pump absorption in the transmission curve. The idler spectrum is limited by blocking the corresponding short-wavelength part of the signal spectrum, $\lambda_{id} < 692\,\text{nm}$ in BBO and $\lambda_{id} < 721\,\text{nm}$ in LBO. These signal-idler pairs are indicated by the blue-shaded regions in the figure. The regions of reduced absorption are indicated by the green shaded box. With this bandwidth clipping, the idler absorption can also be neglected, and the powerful pump beam is considered as the major source of crystal heating.

4.5.2 Temperature dependence of gain bandwidth

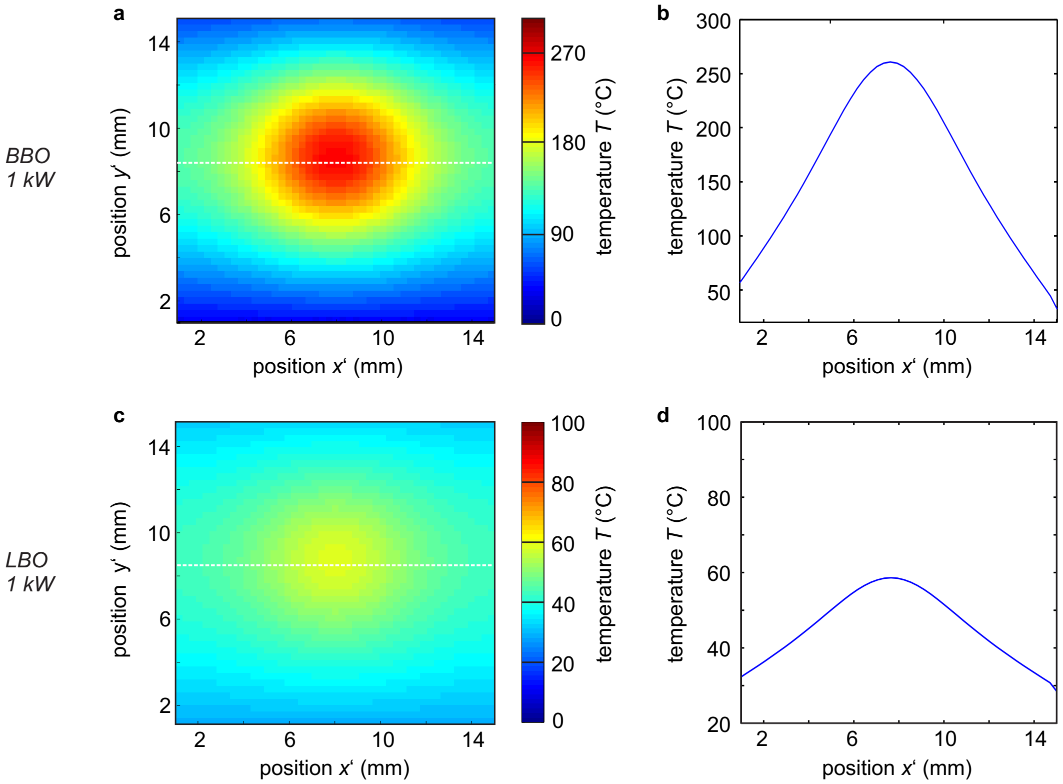

Figure 4.16 Simulated temperature profiles due to the absorption of a 1 kW pump beam with 4 mm diameter within BBO and LBO. The crystal dimensions are 15 × 15 × 2 mm. (**a**) BBO, two-dimensional distribution. The pump propagation is perpendicular to the plotted $x'y'$-plane. (**b**) Lineout profile within the phase-matching plane (crystal's xz-plane), indicated by the white-dashed line in (a). The maximum temperature in BBO is 260°C. (**c**) LBO, two-dimensional distribution. The plotted crystal plane is perpendicular to the pump propagation. (**d**) Lineout profile within the phase-matching plane (crystal's xy-plane), indicated by the white-dashed line in (c). The maximum temperature in LBO is 58°C. Simulations performed by M. LEMKE (DESY).

Due to the heat accumulation and thermal conduction, a temperature profile will develop within the crystal. With neglected signal and idler absorption, and assuming a radial symmetric

GAUSSIAN pump beam, this can be reduced to a one-dimensional radially symmetric problem. The spatially varying temperature gradient will affect the phase-matching due to the thermo-optic effect. To calculate the phase-matching properties, first the temperature profiles were simulated for BBO and LBO, pumped with an average power of $P_{\text{av}} = 1\,\text{kW}$. The crystal dimensions were $x' \times y' \times z' = 15 \times 15 \times 2\,\text{mm}$, where z' is the propagation direction of the pump and $x'y'$ forms the aperture plane. The heat source was a GAUSSIAN beam along z' with 4 mm FWHM diameter in the $x'y'$-plane[9]. The heating power corresponds to the absorbed laser power, $P_{\text{abs}} = \alpha \cdot P_{\text{av}} \cdot 0.2\,\text{cm}$, with the absorption coefficient, α, as listed in table 4.1. Additionally, two heat sinks with a temperature of 20°C were assumed at the bottom and at the top of the crystals ($y' = 0$ and $y' = 15\,\text{mm}$). The heat transfer equation [187] was solved three-dimensionally using a finite-element-method (ANSYS). The simulations were performed by M.LEMKE (DESY). In Fig. 4.16a, the temperature distribution in BBO in the thermal equilibrium is displayed in the $x'y'$-plane at $z' = 1\,\text{mm}$. In this simulation, the BBO crystal heats up to 260°C. This temperature distribution is constant along the pump propagation direction, z'. Within the phase-matching plane in BBO (crystal's xz-plane, indicated by white dashed line), a lateral temperature gradient of about $\mathrm{d}T/\mathrm{d}x' = 27\,\text{Km}^{-1}$ develops between the maximum and the boundary (Fig. 4.16b). In Fig. 4.16c and d, the simulation for LBO is shown. The crystal heats up only to 58°C owing to the weaker absorption. The temperature gradient in the phase-matching plane (xy-plane) is only $\mathrm{d}T/\mathrm{d}x' = 3.5\,\text{K}\,\text{mm}^{-1}$.

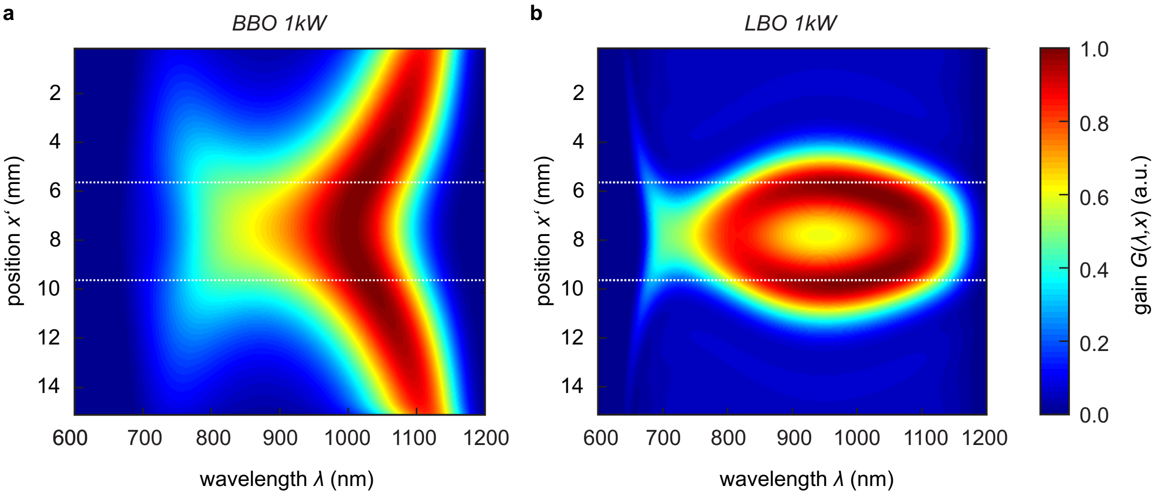

Figure 4.17 Thermal effects on non-collinear OPCPA with BBO (a) and LBO (b) crystals. The simulated temperature lineouts from Fig. 4.16b and d were used to calculate the wavelength-dependent gain, $G(\lambda, x')$ in dependence on the transversal x'-position. The white-dashed lines indicate the FWHM of the pump beam.

The spectral gain, $G(\lambda, x')$ was calculated in dependence on the transversal crystal position, x', taking into account the temperature lineout profile of BBO and LBO (Fig. 4.16a and d). The undepleted pump approximation was used, according to Eq. (2.30). The thermo-optic coefficients, $\partial n/\partial T$ (see Table 4.1), were implemented in the SELLMEIER-equations (see Appendix A), to calculate the temperature-dependent wave vectors,

$$k(\lambda, T) = 2\pi/\lambda \cdot [n(\lambda, T) + \partial n/\partial T]. \tag{4.4}$$

---

[9] This assumption is valid in the undepleted pump approximation, i.e. $\mathrm{d}P_{\text{av}}/\mathrm{d}z' = 0$

A super-GAUSSIAN signal spectrum,

$$I(\lambda) \propto \exp(-\lambda^{10}/\lambda_c^{10}), \tag{4.5}$$

was used as input spectrum for both crystals. The spectrum ranged from 641 nm–1200 nm at 5% intensity. The results are shown in Fig. 4.17. For BBO (a), the phase-matching angle was optimized for the peak temperature of 260°C, $\theta = 23.95°$ (the non-collinear angle was not varied). As expected, because of the varying phase-matching conditions, the spectral gain bandwidth decreases along the temperature gradient. Owing to the large thermal acceptance of BBO, $\Delta T \Delta k$, a large bandwidth is achieved at least within the 4 mm FWHM of the pump beam (indicated by white-dashed lines). Although LBO has a five-times lower maximum temperature, a similar result is obtained (b). The phase-matching angle was optimized for 58°C, $\theta = 20.1°$.

In conclusion, broadband OPCPA is possible at high average power, pumped at 1 kW. BBO and LBO crystals keep the broadband phase-matching at least within the FWHM of the pump. Whereas the larger thermal acceptance bandwidth of BBO balances its drastic temperature increase, LBO heats up only to a fifth of the temperature, but has a similar bandwidth behavior. The behavior of BBO at such high temperature needs to be investigated experimentally. In order to limit the total accumulated temperature, BBO could be used in the pre-amplification stage, where its large nonlinear coefficient benefits large single-pass gain. For amplifier stages with highest average pump powers, LBO affords a better durability. It is worth noting that recent absorption measurements of LBO crystals revealed a one-order of magnitude smaller absorption coefficient as compared to the literature values used for the presented simulations. Thus, LBO crystals produced today are expected to be applicable even for 10 kW of pump power.

Chapter 5

Conclusion and Outlook

With the realization of a single-shot temporal diagnostic method for XUV and X-ray free-electron lasers and a high repetition rate burst-mode laser amplifier, this work contributes significantly to the improvement of the experimental conditions at FEL facilities. The performance of two-color pump-probe experiments at SASE FELs is hindered by pulse-to-pulse fluctuations. In particular, the arrival time delay and the pulse shape vary from pulse to pulse. Exact knowledge of the pulse characteristics on a permanent regular basis promises a new quality of FEL science. The temporal diagnostic method developed in this work allows to measure both parameters simultaneously using a solid-state cross-correlation. An initially transparent solid-state target (fused silica or silicon nitride) was pumped with an XUV pulse. The ultrafast optical transmission change due to photoionization was probed with a known optical laser pulse. For the evaluation, a comprehensive theoretical model was developed, including the ionization dynamics within the target and the related change of the optical properties. It was shown that the measured signal is related to the cross-correlation between both pulses, allowing temporal jitter measurements and the retrieval of the pulse duration of single FEL pulses. As the method does not rely on discrete atomic transitions, it is applicable from the XUV to the X-ray regime. The presented measurements were performed at FLASH, using two distinct wavelengths. The measured pulse durations were (184 ± 14) fs at 41.5 nm and (21 ± 19) fs at 5.5 nm wavelength, using a 1 mm fused silica target. The possibility for online measurements, i.e. simultaneous temporal characterization during an experiment, was investigated using ultra-thin silicon nitride membranes of 20 nm thickness. In the soft X-ray range, a residual soft-X-ray transmission of 10–45% is expected. The single-shot measurement yielded (34 ± 19) fs at 5.5 nm. The measured pulse durations are in agreement with theoretical expectations for the used FEL operation parameters. With adequate resolution, the detection of complex FEL pulse shapes is possible, even with a realistic signal-to-noise ratio. It was shown that a temporal resolution of sub-10 fs is possible, if a short optical pulse is available at the experimental end station. Therefore, a compact OPCPA was developed, delivering wavelength-tunable pulses as short as 20 fs at a pulse energy of 1 µJ. It can be upgraded to sub-10 fs pulse duration by the implementation of specially designed chirped mirrors. The device is pumped by the available 60 fs pump-probe laser and seeded by a white-light continuum. Beyond the application as a temporal diagnostic method, the presented setup is highly suited for jitter-free high-resolution pump-probe experiments in solid-state materials. Not only open questions about the carrier dynamics in dielectrics and semiconductors can be clarified in order to improve the X-ray pulse duration measurement. Also, the investigation of other ultrafast processes is possible, such as exciton formation and spin transfer.

Worldwide, FLASH is the only operational high repetition rate FEL, delivering pulse trains of 800 pulses with a repetition rate of 10 Hz. Future high repetition rate FELs are under construction, such as FLASH II and the European XFEL. The increased number of pulses of these facilities allow for a better data quality in terms of higher statistical significance and better signal-to-noise ratio. However, the bottleneck are outdated optical lasers. Low repetition rate Ti:sapphire systems are limited to pulse durations of about 20 fs. At FLASH, the burst-mode amplifier is limited to 70 fs pulse duration and 10 µJ pulse energy, which is not sufficient for external FEL seeding. In this work, this bottleneck has been overcome by means of a high-power optical parametric chirped-pulse amplifier for the application as seeding and pump-probe laser. The realized prototype deliveres pulse trains of 22 pulses, supporting sub-7 fs pulse duration at 1.4 mJ pulse energy. A total energy conversion efficiency of 20% from the SHG pump pulses to the OPCPA output pulses is achieved. The system is capable to approach optical peak powers in the terawatt regime. With the short pulse duration, the pump-probe resolution is potentially increased by one order of magnitude. Currently, a 100 kHz version is being developed as seeding laser for FLASH-2. Recently, the target parameters, 1 mJ pulse energy and sub-30 fs pulse duration, have been achieved. To reach the final repetition rate of 1 MHz, further high-power pump amplifiers are under development. The OPCPA output energy and the spectral bandwidth are highly sensitive to pump-to-signal drifts. A synchronization technology for OPCPA long-term stability improvement has been investigated. The generation of a white-light supercontinuum in YAG was utilized for broadband OPCPA seeding with an intrinsic synchronization to the OPA pump. A stable operation of a white-light source over a period of 28 hours was demonstrated with a signal-to-pump jitter of 7 fs rms, which is an outstanding performance compared to active methods. However, this introduces small additional jitter in the FEL-to-signal synchronization. Furthermore, a stable white-light amplification and temporal compression was demonstrated. The scaling possibilities towards continuously operating kilowatt-pumped high-power OPCPAs was theoretically evaluated. It was shown that with adequate spectral clipping of the signal seed, the major contribution to the heat load is introduced by the pump absorption, rather than signal or idler absorption. The simulations confirmed the preservation of the broad gain bandwidth in 1 kW pumped BBO and LBO crystals. Assuming a pump-to-signal conversion efficiency of up to 20%, possible output powers of up to 200 W are expected. Recent absorption measurements of LBO revealed that these crystals might even be applicable for OPCPAs with kW of output power, provided that tens of kW pump amplifiers are available.

In outlook, the developments potentially contribute to a major advancement in FEL science in general. With the potential for online measurements and high temporal resolution, the single-shot cross-correlator is a user friendly tool for FLASH and other FELs. The recently founded FEL pulse duration measurements group in the EuroFEL project discussed about future implementation schemes of the cross-correlation technique at FLASH, FLASH II, the European XFEL, FERMI@Elettra and the SwissFEL. Especially at the high repetition rate FELs, FLASH and European XFEL, the characterization of each single pulse within the pulse train is of particular importance. The synergy with the developed high repetition rate OPCPA will facilitate time-resolved experiments at FELs with unprecedented precision and data quality. Indeed, the irradiation of the solid-state targets at high repetition rates has still to be investigated in terms of heat accumulation and thermal damage, but possible solutions are already in development, such as a moving target or a scanning mirror. The achievements in the field of high power OPCPA technology gained in this work are also of high importance in laser science. The future kilowatt-pumped OPCPAs are traded as a pillar for the construction of new laser-based brilliant coherent light sources, outperforming existing Ti:sapphire amplifiers by at least one order of magnitude. The first large-scale facility, the Extreme Light Infrastructure Attosecond Light Pulse Source (ELI ALPS), is planned to be commissioned in the year 2017 in Szeged, Hungary [188, 189].

Appendices

Appendix A

Refractive indices of nonlinear crystals

The refractive indices used for the calculation of the phase-matching were obtained from the dedicated SELLMEIER-equation:

$$n^2(\lambda) = A + \frac{B}{\lambda^2 - C} + D\lambda^2 + E\lambda^{-4}. \tag{A.1}$$

The SELLMEIER-coefficients are listed in table A.1

	A	B	C	D	E
BBO (o) [190]	2.7405	$0.0184\cdot10^{-12}$	$0.0179\cdot10^{-12}$	$-0.0155\cdot10^{12}$	0
BBO (e)	2.373	$0.0128\cdot10^{-12}$	$0.0156\cdot10^{-12}$	$-0.0044\cdot10^{12}$	0
LBO (x) [191]	2.45414	0.011249	0.01135	-0.014591	$-6.6\cdot10^{-4}$
LBO (y)	2.53907	0.012711	0.012523	-0.018540	$2\cdot10^{-4}$
LBO (z)	2.586179	0.013099	0.011893	-0.017968	$-2.26\cdot10^{-4}$
BiBO (x) [192]	3.07317	0.03292	0.03011	-0.01257	0
BiBO (y)	3.16383	0.04007	0.02545	-0.01535	0
BiBO (z)	3.64825	0.05458	0.02952	-0.02019	0

Table A.1 SELLMEIER-coefficients of different nonlinear crystals. Wavelength, λ, in µm. References: BBO [190], LBO [191], BiBO [192].

Appendix B

The transfer matrix formalism

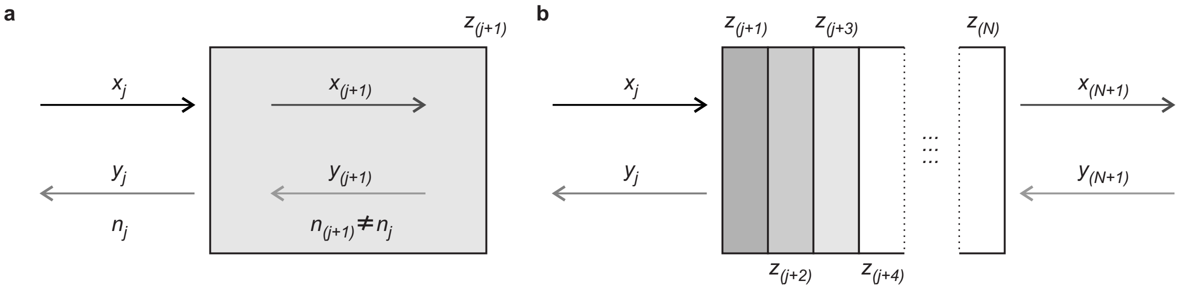

Figure B.1 Matrix transfer method. (**a**) Propagation of an optical wave with electric field amplitude x_j (incident) and y_j (reflected) through a single layer of thickness $z_{(j+1)} - z_j$ and refractive index $n_{(j+1)} \neq n_j$. The amplitudes $x_{(j+1)}$ and $y_{(j+1)}$ denote the amplitudes after the first interface. (**b**) Propagation through a sequence of N layers, with definitions according to (a).

For the calculation of the transmission of an optical laser pulse through a free-electron plasma, the transfer matrix formalism was used (see chapter 3). For the evaluation of the experiment, an exponentially decaying electron density is assumed, $n_{\mathrm{e}}(z)$, according to eq. 3.7. The corresponding refractive index gradient can be approximated by a sequence of thin layers of thickness $z_{(j+1)} - z_j = 1\,\mathrm{nm}$. The transfer matrix formalism describes the propagation of an optical wave,

$$E_j(z) = x_j e^{ik_j z} + y_j e^{-ik_j z} \tag{B.1}$$

through a such layered structure. The situation for a single layer and with an optical wave under normal incidence is shown in Fig. B.1a. The following field amplitudes are defined: x_j (incident wave) and y_j (reflected wave), $x_{(j+1)}$ (transmitted outgoing wave) and $y_{(j+1)}$ (back-travelling wave). The relation is described with

$$\begin{pmatrix} x_j \\ y_j \end{pmatrix} = M_j \begin{pmatrix} x_{(j+1)} \\ y_{(j+1)} \end{pmatrix}, \tag{B.2}$$

with the transfer matrix

$$\begin{aligned} M_j &= \frac{1}{t_{(j-1,j)}} \begin{pmatrix} 1 & r_{(j-1,j)} \\ r_{(j-1,j)} & 1 \end{pmatrix} \begin{pmatrix} e^{-ik_j} & 0 \\ 0 & e^{ik_j} \end{pmatrix} \\ &= \frac{1}{t_{(j-1,j)}} \begin{pmatrix} e^{-ik_j} & r_{(j-1,j)} e^{ik_j} \\ r_{(j-1,j)} e^{-ik_j} & e^{ik_j} \end{pmatrix}, \end{aligned} \tag{B.3}$$

and where

$$k_j = \frac{2\pi}{\lambda_\mathrm{L}} n\left[n_\mathrm{e}(z_j)\right] \tag{B.4}$$

is the propagation constant in the j-th layer and $t_{(j-1,j)}$ and $r_{(j-1,j)}$ are the FRESNEL-coefficients for transmission and reflection normal incidence with respect to the interface,

$$t_{(j-1,j)} = \frac{2n_{(j-1)}}{n_{(j-1)}+n_j}, \tag{B.5}$$

and

$$r_{(j-1,j)} = \frac{n_{(j-1)}-n_j}{n_{(j-1)}+n_j}. \tag{B.6}$$

For a structure consisting of N layers and $N+1$ interfaces, correspondingly (Fig. B.1b) the relation is expressed as

$$\begin{pmatrix} x_1 \\ x_2 \end{pmatrix} = \left(\prod_{j=1}^{N} M_n\right) \frac{1}{t_{(N,N+1)}} \begin{pmatrix} 1 & r_{(N,N+1)} \\ r_{(N,N+1)} & 1 \end{pmatrix} \cdot \begin{pmatrix} x_{(N+1)} \\ y_{(N+1)} \end{pmatrix}, \tag{B.7}$$

and can be simplified to

$$\begin{pmatrix} x_1 \\ y_1 \end{pmatrix} = M \begin{pmatrix} x_{(N+1)} \\ y_{(N+1)} \end{pmatrix}, \tag{B.8}$$

yielding

$$x_1 = M_{11}x_{N+1} + M_{12}y_{N+1} = M_{11}x_{(N+1)}, \tag{B.9}$$

$$y_1 = M_{21}x_{N+1} + M_{22}y_{N+1} = M_{21}x_{(N+1)}, \tag{B.10}$$

with $y_{(N+1)} = 0$. The ratio of the amplitudes yields the transmission,

$$t = \frac{x_{(N+1)}}{x_1} = \frac{1}{M_{11}}, \tag{B.11}$$

and the reflection,

$$r = \frac{y_1}{x_1} = \frac{M_{21}}{M_{11}}, \tag{B.12}$$

of the layered system. The transmission of the optical power is given by

$$T = |t|^2 \text{ and } R = |r|^2. \tag{B.13}$$

Bibliography

[1] W. Ackermann *et al.* Operation of a free-electron laser from the extreme ultraviolet to the water window. *Nature Photonics*, 1:336–342, 2007.

[2] R. Riedel *et al.* Single-shot pulse duration monitor for extreme ultraviolet and X-ray free-electron lasers. *Nature Comm.*, 4:1731, 2013.

[3] R. Riedel *et al.* Long-term stabilization of high power optical parametric chirped-pulse amplifiers. *Opt. Express*, XX:XXX–XXX, 2013.

[4] P. Emma *et al.* First lasing and operation of an ångstrom wavelength free-electron laser. *Nature Photonics*, 4:641–647, 2010.

[5] E. Allaria *et al.* The FERMI@Elettra free-electron-laser source for coherent x-ray physics: photon properties, beam transport system and applications. *New J. Phys.*, 12:075002, 2010.

[6] T. Ishikawa *et al.* A compact X-ray free-electron laser emitting in the sub-ångström region. *Nature Photonics*, 6:540–544, 2012.

[7] E. Allaria *et al.* Highly coherent and stable pulses from the FERMI seeded free-electron laser in the extreme ultraviolet. *Nature Photonics*, 6:699–704, 2012.

[8] H. N. Chapman *et al.* Femtosecond X-ray protein nanocrystallography. *Nature*, 470:73–77, 2011.

[9] K. J. Gaffney and H. N. Chapman. Imaging atomic structure and dynamics with ultrafast X-ray scattering. *Science*, 316:1444–1448, 2007.

[10] M. J. Bogan *et al.* Single particle x-ray diffractive imaging. *Nano Lett.*, 8:310–316, 2008.

[11] A. Barty *et al.* Ultrafast single-shot diffraction imaging of nanoscale dynamics. *Nature Photonics*, 2:415–419, 2008.

[12] M. M. Seibert *et al.* Single mimivirus particles intercepted and imaged with an X-ray laser. *Nature*, 470:78–81, 2011.

[13] B. Nagler *et al.* Turning solid aluminium transparent by intense soft X-ray photoionization. *Nature Physics*, 5:693–696, 2009.

[14] L. Fang *et al.* Double Core-Hole Production in N_2. *Phys. Rev. Lett.*, 105:083005, 2010.

[15] J. P. Cryan *et al.* Auger Electron Angular Distribution of Double Core-Hole States in the Molecular Reference Frame. *Phys. Rev. Lett.*, 105:083004, 2010.

[16] L. Young *et al.* Femtosecond electronic response of atoms to ultra-intense X-rays. *Nature*, 466:56–61, 2010.

[17] H. Wabnitz *et al.* Multiple ionization of atom clusters by intense soft X-rays from a free-electron laser. *Nature*, 420:482–485, 2002.

[18] M. Meyer *et al.* Two-color photoionization in XUV free-electron and visible laser fields. *Phys. Rev. A*, 74:011401, 2006.

[19] C. Bostedt *et al.* Multistep Ionization of Argon Clusters in Intense Femtosecond Extreme Ultraviolet Pulses. *Phys. Rev. Lett.*, 100:133401, 2008.

[20] S. Hellmann *et al.* Ultrafast Melting of a Charge-Density Wave in the Mott Insulator 1T-TaS$_2$. *Phys. Rev. Lett.*, 105:187401, 2010.

[21] M. Först *et al.* Driving magnetic order in a manganite by ultrafast lattice excitation. *Phys. Rev. B*, 84:241104, 2011.

[22] C. Gutt *et al.* Resonant magnetic scattering with femtosecond soft X-ray pulses from a free electron laser operating at 1.59 nm. *Phys. Rev. B*, 79:212406, 2009.

[23] B. Pfau *et al.* Ultrafast optical demagnetization manipulates nanoscale spin structure in domain walls. *Nature Comm.*, 3:1100, 2012.

[24] A. Höll *et al.* Thomson scattering from near-solid density plasmas using soft X-ray free electron lasers. *High Energ. Dens.Phys.*, 3:120–130, 2007.

[25] U. Zastrau *et al.* Bremsstrahlung and line spectroscopy of warm dense aluminum plasma heated by XUV free-electron-laser radiation. *Phys. Rev. E*, 78:066406, 2008.

[26] C. Fortmann *et al.* Bremsstrahlung vs. Thomson scattering in VUV-FEL plasma experiments. *High Energ. Dens. Phys.*, 2:57–69, 2006.

[27] R. R. Fäustlin *et al.* Observation of Ultrafast Nonequilibrium Collective Dynamics in Warm Dense Hydrogen. *Phys. Rev. Lett.*, 104:125002, 2010.

[28] R. Kodama *et al.* Nuclear fusion: Fast heating scalable to laser fusion ignition. *Nature*, 418:933–934, 2002.

[29] J. M. Glownia *et al.* Time-resolved pump-probe experiments at the LCLS. *Opt. Express*, 18:17620–17630, 2010.

[30] M. R. Bionta *et al.* Spectral encoding of X-ray/optical relative delay. *Opt. Express*, 19:21855–21865, 2011.

[31] T. Maltezopoulus *et al.* Single-shot timing measurement of extreme ultraviolet free-electron laser pulses. *New J. Phys.*, 10:033026, 2008.

[32] S. Schulz *et al.* Femtosecond-precision synchronization of the pump-probe optical laser for user experiments at FLASH. In *SPIE Proceedings*, volume 8778, April 2013.

[33] P. Sigalotti *et al.* Ultrafast laser synchronization at the FERMI@Elettra FEL. In *SPIE Proceedings*, April 2013.

[34] M. Richter *et al.* Multiphoton ionization of atoms with soft x-ray pulses. *J. Phys. B: At. Mol. Opt. Phys.*, 43:194005, 2010.

[35] B. Rudek *et al.* Ultra-efficient ionization of heavy atoms by intense X-ray free-electron laser pulses. *Nature Photonics*, 6:858–865, 2012.

[36] G. Lambert *et al.* Injection of harmonics generated in gas in a free-electron laser providing intense and coherent extreme-ultraviolet light. *Nature Physics*, 4:296–300, 2008.

[37] J. Amann *et al.* Demonstration of self-seeding in a hard-X-ray free-electron laser. *Nature Photonics*, 6:693–698, 2012.

[38] Z. T. Zhao *et al.* First lasing of an echo-enabled harmonic generation free-electron laser. *Nature Photonics*, 6:360–363, 2012.

[39] D. Xiang *et al.* Evdience of high harmonics from echo-enabled harmonic generation for seeding x-ray free electron lasers. *Phys. Rev. Lett.*, 108:024802, 2012.

[40] I. Grguras *et al.* Ultrafast X-ray pulse characterization at free-electron lasers. *Nature Photonics*, 6:852–857, 2012.

[41] U. Frühling *et al.* Light-field streaking for FELs. *J. Phys. B: At. Mol. Opt. Phys.*, 44:243001, 2011.

[42] R. Mitzner *et al.* Direct autocorrelation of soft-x-ray free-electron-laser pulses by time-resolved two-photon double ionization of He. *Phys. Rev. A*, 80:025402, 2009.

[43] Y. H. Jiang *et al.* Temporal coherence effects in multiple ionization of N2 via XUV pump-probe autocorrelation. *Phys. Rev. A*, 82:041403(R), 2010.

[44] S. Düsterer *et al.* Femtosecond X-ray pulse length characterization at the Linac Coherent Light Source free-electron laser. *New J. Phys.*, 13:093024, 2011.

[45] M. Drescher *et al.* Time-diagnostics for improved dynamics experiments at XUV FELs. *J. Phys. B: At., Mol. Opt. Phys.*, 43:194010, 2010.

[46] Y. Ding *et al.* Femtosecond X-Ray Pulse Characterization in Free-Electron Laser Using a Cross-Correlation Technique. *Phys. Rev. Lett.*, 109:254802, 2012.

[47] T. Pfeifer *et al.* Partial-coherence method to model experimental free-electron laser pulse statistics. *Opt. Lett.*, 35:3441–3443, 2010.

[48] A. Lutman *et al.* Femtosecond x-ray free electron laser pulse duration measurement from spectral correlation function. *Phys. Rev. ST*, 15:030705, 2012.

[49] C. Gutt *et al.* Single Shot Spatial and Temporal Coherence Properties of the SLAC Linac Coherent Light Source in the Hard X-Ray Regime. *Phys. Rev. Lett.*, 108:024801, 2012.

[50] Y. Inubushi *et al.* Determination of the Pulse Duration of an X-Ray Free Electron Laser Using Highly Resolved Single-Shot Spectra. *Phys. Rev. Lett.*, 109:144801, 2012.

[51] J. Wu *et al.* LCLS X-ray pulse duration measurement using the statistical fluctuation method. In *Proceedings of FEL2010*, 2010.

[52] N. Muller *et al.* Time-to-space mapping in a gas medium for the temporal characterization of vacuum-ultraviolet pulses. *Appl. Phys. Lett.*, 90:121112–121112–3, 2007.

[53] U. Frühling *et al.* Single-shot terahertz-field-driven X-ray streak camera. *Nature Photonics*, 3:523–528, 2009.

[54] K. Tiedtke *et al.* The soft x-ray free-electron laser FLASH at DESY: beamlines, diagnostics and end-stations. *New J. Phys.*, 11:023029, 2009.

[55] M. Gensch *et al.* New infrared undulator beamline at FLASH. *Infrared Phys. Techn.*, 51:423–425, 2008.

[56] M. C. Hoffmann and J. A. Fulop. Intense ultrashort terahertz pulses: generation and applications. *J. Phys. D: Appl. Phys.*, 44:083001, 2011.

[57] H. Hiori *et al.* Single-cycle terahertz pulses with amplitudes exceeding 1 MV/cm generated by optical rectification in LiNbO(3). *Appl. Phys. Lett.*, 99:091106, 2011.

[58] A. Krikunova *et al.* Time-resolved ion spectrometry on xenon with the jitter-compensated soft x-ray pulses of a free-electron laser. *New J. Phys.*, 11:123019, 2009.

[59] M. Krikunova *et al.* Ultrafast photofragmentation dynamics of molecular iodine drive with time XUV and near-infrared pulses. *J. Chem. Phys.*, 134:024313, 2011.

[60] C. Gahl *et al.* A femtosecond X-ray/optical cross-correlator: FLASH X-ray pulse induced transient changes of the optical reflectivity. *Nature Photonics*, 2:165–169, 2008.

[61] O. Krupin *et al.* Temporal cross-correlation of x-ray free electron and optical lasers using soft x-ray pulse induced transient reflectivity. *Opt. Express*, 20:11396–11406, 2012.

[62] A. Azima *et al.* Time-resolved pump-probe experiments beyond the jitter limitations at FLASH. *Appl. Phys. Lett.*, 94:144102, 2009.

[63] S. Schorb *et al.* X-ray-optical-cross-correlator for gas-phase experiments at the Linac Coherent Light Source free-electron laser. *Appl. Phys. Lett.*, 100:121107, 2012.

[64] M. Beye *et al.* X-ray pulse preserving single-shot optical cross-correlation method for improved experimental temporal resolution. *Appl. Phys. Lett.*, 100:121108, 2012.

[65] M. Harmand *et al.* Achieving few-femtosecond time-sorting at hard X-ray free-electron lasers. *Nature Photonics*, 7:215–218, 2013.

[66] H. J. Zeiger *et al.* Theory for displacive excitation of coherent phonons. *Phys. Rev. B.*, 45:768–778, 1992.

[67] K. Sokolowski-Tinten *et al.* Femtosecond X-ray measurement of coherent lattice vibrations near the Lindemann stability limit. *Nature*, 422:287–289, 2003.

[68] L. H. Yu *et al.* First Ultraviolet High-Gain Harmonic-Generation Free-Electron Laser. *Phys. Rev. Lett.*, 91:074801, 2003.

[69] J. Rossbach P. Schmüser, M. Dohlus. *Ultraviolet and soft X-Ray Free-Electron Lasers*. Springer Verlag, 2008.

[70] M. V. Yurkov E. L. Saldin, A. Schneidmiller. *The Physics of Free-Electron Lasers*. Springer Verlag, 1999.

[71] I. Will *et al.* Photoinjector drive laser of the FLASH FEL. *Opt. Express*, 19:23770–23781, 2011.

[72] S. Ackermann *et al.* Generation of coherent 19- and 38-nm Radiation at a Free-Electron Laser Directly Seeded at 38 nm. *Phys. Rev. Lett.*, 111:114801, 2013.

[73] L. DiMauro *et al.* First SASE and seeded FEL lasing of the NSLS DUV FEL at 266 and 400 nm. *Nucl. Instrum. Meth. A*, 507:15–18, 2003.

[74] A. Willner *et al.* Coherent Control of High Harmonic Generation via Dual-Gas Multijet Arrays. *Phys. Rev. Lett.*, 107, 2011.

[75] A. Willner *et al.* Efficient control of quantum paths via dual-gas high harmonic generation. *New J. Phys.*, 13, 2011.

[76] A. Willner *et al.* Coherent spectral enhancement of carrier-envelope-phase stable continua with dual-gas high harmonic generation. *Opt. Lett.*, 37:3672–3674, 2012.

[77] G. Stupakov. Using the Beam-Echo Effect for Generation of Short-Wavelength Radiation. *Phys. Rev. Lett.*, 102:074801, 2009.

[78] J. D. Jackson. *Classical Electrodynamics*. Wiley, New York, 1998.

[79] J.-C. Diels and W. Rudolph. *Ultrashort Laser Pulse Phenomena*. Elsevier, 2006.

[80] R.W. Boyd. *Nonlinear Optics*. Elsevier, 2008.

[81] G. Cerullo and S. De Silvestri. Ultrafast optical parametric amplifiers. *Rev. Sci. Instrum.*, 74, 2003.

[82] Robert W. Boyd. *Nonlinear Optics*. Elsevier, 2008.

[83] J. A. Armstrong *et al.* Interaction between light waves in a nonlinear dielectric. *Phys. Rev.*, 127:1918–1939, 1962.

[84] I. N. Ross *et al.* Analysis and optimization of optical parametric chirped pulse amplification. *J. Opt. Soc. Am. B*, 19:2945–2956, 2002.

[85] D. S. Hum and M. M. Fejer. Quasi-phasematching. *C. R. Phys.*, 8:180–198, 2007.

[86] D. N. Nikogosyan V. G. Dmitriev, G. G. Gurzadyan. *Handbook of Nonlinear Optical Crystals*. Springer Verlag, 1991.

[87] G. Arisholm *et al.* Ultra-broadband chirped-pulse optical parametric amplifier with angularly dispersed beams. *Opt. Express*, 12:518–530, 2004.

[88] T. Wilhelm *et al.* Sub-20-fs pulse tunable across the visible from a blue-pumped single-pass noncollinear parametric converter. *Opt. Lett.*, 22:1494–1496, 1997.

[89] D. N. Schimpf *et al.* Theoretical analysis of the gain bandwidth for noncollinear parametric amplification of ultrafast pulses. *J. Opt. Soc. Am. B*, 24:2837–2846, 2007.

[90] J. Bromage *et al.* Analysis and suppression of parasitic processes in noncollinear optical parametric amplifiers. *Opt. Express*, 19:16797–16808, 2011.

[91] B. C. Stuart *et al.* Nanosecond-to-femtosecond laser-induced breakdown in dielectrics. *Phys. Rev. B*, 53:1749–1761, 1996.

[92] M. Bradler *et al.* Femtosecond continuum generation in bulk laser host materials with sub-muJ pump pulses. *Appl. Phys. B: Lasers Opt.*, 97:561–574, 2009.

[93] S. Tzortzakis *et al.* Self-Guided Propagation of Ultrashort IR Laser Pulse in Fused Silica. *Phys. Rev. Lett.*, 87:213902, 2001.

[94] Y. Liu *et al.* Different tendencies of breakdown threshold on pulse duration in the subpicosecond regime in fused silica. *J. Opt. A: Pure Appl. Opt.*, 7:198–203, 2005.

[95] L. Bergé *et al.* Multifilamentation of powerful optical pulses in silica. *Phys. Rev. A*, 81:013817, 2010.

[96] B. La Fontaine *et al.* Filamentation of ultrashort pulse laser beams resulting from their propagation over long distances in air. *Phys. Plasmas*, 6:1615–1621, 1999.

[97] M. Emons *et al.* Sub-10-fs pulses from a MHz-NOPA with pulse energies of 0.4 muJ. *Opt. Express*, 18:1191–1196, 2010.

[98] A. Brodeur and L. Chin. Ultrafast white-light continuum generation and self-focusing in transparent condensed media. *J. Opt. Soc. Am. B*, 16:637–650, 1999.

[99] C. B. Schaffer *et al.* Laser-induced breakdown and damage in bulk transparent materials induced by tightly focused femtosecond laser pulses. *Meas. Sci. Technol.*, 20:1764–1794, 2001.

[100] Z. Wu *et al.* Filamentation and temporal reshaping of a femtosecond pulse in fused silica. *Phys. Rev. A*, 68:063820, 2003.

[101] N. Medvedev and B. Rethfeld. Transient dynamics of the electronic subsystem of semiconductors irradiated with an ultrashort vacuum ultraviolet laser pulse. *New J. Phys.*, 12:073037, 2010.

[102] L. E. Ramos *et al.* Structural, electronic, and effective-mass properties of silicon and zinc-blende group-III nitride semiconductor compounds. *Phys. Rev. B*, 63:165210, 2001.

[103] E. O. Kane. Electron Scattering by Pair Production in Silicon. *Phys. Rev.*, 159:624–631, 1967.

[104] N. Medvedev B. Ziaja. Modelling ultrafast transitions within laser-irradiated solids. *High Energ. Dens. Phys.*, 8:18–29, 2011.

[105] N. Metropolis and S. Ulam. The Monte Carlo Method. *J. Am. Stat. Assoc.*, 44, No. 247:335–341, 1949.

[106] B. J. Alder and T. E. Wainwright. Studies in Molecular Dynamics. I. General Method. *J. Chem. Phys.*, 31:459–466, 1959.

[107] N. Medvedev *et al.* Short-Time Electron Dynamics in Aluminum Excited by Femtosecond Extreme Ultraviolet Radiation. *Phys. Rev. Lett.*, 107:165003, 2011.

[108] N. A. Medvedev and B. Rethfeld. Electron kinetics in semiconductors and metals irradiated with VUV-XUV femtosecond laser pulses. *Proc. SPIE Int. Soc. Opt. Eng.*, 8077:80770Q, 2011.

[109] N. Medvedev *et al.* Electron kinetics in femtosecond X-ray irradiated SiO2. *Contrib. Plasma Phys.*, 2013.

[110] B. L. Henke *et al.* X-ray interactions: photoabsorption, scattering, transmission, and reflection at E = 50-30.000 eV, Z = 1-92. *Atom. Data Nucl. Data*, 54:181–342, 1993.

[111] C. Kingman and J. Frank. *Poisson processes. Vol. 3.* Clarendon Press, 1992.

[112] W. Y. Ching Y. Xu. Electronic and optical properties of all polymorphic forms of silicon dioxide. *Phys. Rev. B*, 44:11048–11059, 1991.

[113] N. Medvedev and B. Rethfeld. Effective energy gap of semiconductors under irradiation with an ultrashort VUV laser pulse. *Europhys. Lett.*, 88:55001, 2009.

[114] A. V. Shaposhnikov *et al.* Electronic Band Structure and Effective Masses of Electrons and Holes in the α and β Phases of Silicon Nitride. *Phys. Solid State*, 49, No 9:1628–1632, 2007.

[115] P. B. Corkum and F. Krausz. Attosecond science. *Nature Physics*, 3:381–387, 2007.

[116] J. J. Quinn *et al.* Range of Excited Electrons in Metals. *Phys. Rev.*, 126:1453–1457, 1962.

[117] D. R. Penn *et al.* Electron mean-free-path calculations using a model dielectric function. *Phys. Rev. B*, 35:482–486, 1987.

[118] S. Samarin *et al.* Secondary-electron emission mechanism of LiF film by (e,2e) spectroscopy. *Surf. Sci.*, 548:187–199, 2004.

[119] V. V. Temnov *et al.* Multiphoton ionization in dielectrics: comparison of circular and linear polarization. *Phys. Rev. Lett.*, 97:237403, 2006.

[120] D. Grojo *et al.* Time-evolution of carriers after multiphoton ionization of bulk dielectrics. In *Conference on Lasers and Electro-Optics/International Quantum Electronics Conference, OSA Technical Digest.*, Baltimore, MD, USA, May 31 - June 05 2009.

[121] J. Frenkel. On the Transformation of Light into Heat in Solid. I. *Phys. Rev.*, 37:17–44, 1931.

[122] G. H. Wannier. The structure of Electronic Excitation Levels in Insulating Crystals. *Phys. Rev.*, 52:191–197, 1937.

[123] W. Y. Liang. Excitons. *Physics Education*, 5:226–230, 1970.

[124] L. Spitzer. *Physics of Fully Ionized Gases.* Interscience, New York, 1962.

[125] M. P. Bachynski I. P. Sharkofsky, T. W. Johnston. *The particle kinetics of plasmas.* Addison-Wesley Educational Publishers Inc, Boston, 1966.

[126] U. Wagner U. Teubner and E. Förster. Sub-10 fs gating of optical pulses. *J. Phys. B: At. Mol. Opt. Phys.*, 34:2993–3002, 2001.

[127] A. Monmayrant *et al.* A newcomer's guide to ultrashort pulse shaping and characterization. *J. Phys. B: At. Mol. Phys.*, 43:103001, 2010.

[128] C. Iaconis and I. A. Walmsey. Spectral phase interferometry for direct electric field reconstruction of ultrashort optical pulses. *Opt. Lett.*, 23:792–794, 1998.

[129] R. Trebino and D. J. Kane. Using phase retrieval to measure the intensity and phase of ultrashort pulses: frequency-resolved optical gating. *Journal Opt. Soc. Am. A*, 10:1101–1111, 1993.

[130] D. J. Kane and R. Trebino. Single-shot measurement of the intensity and phase of an arbitrary ultrashort pulse using frequency-resolved gating. *Optics Lett.*, 18:823–825, 1993.

[131] A. L. Cavalieri *et al.* Clocking femtosecond X-rays. *Phys. Rev. Lett.*, 94:114801, 2005.

[132] F. Löhl *et al.* Electron bunch timing with femtosecond precision in a superconducting free-electron laser. *Phys. Rev. Lett.*, 104:144801, 2010.

[133] S. Simrock *et al.* Synchronization system for ERLs. *Nucl. Instrum. Meth. A*, 557:293–298, 2006.

[134] F. Tavella *et al.* Few-femtosecond timing at fourth-generation X-ray light sources. *Nature Photonics*, 5:162–165, 2011.

[135] E. Wolf M. Born. *Principles of Optics.* Cambridge University Press, Cambridge, 2002, 54–70, 2002.

[136] O. S. Heavens. *Optical Properties of Thin Solid Films.* Dover Punlications, Mineola, New York, 1991.

[137] D. C. Sorensen J. J. Moré. Computing a Trust Region Step. *SIAM J. Optimiz.*, 2:575–601, 1992.

[138] P. Martin *et al.* Subpicosecond study of carrier trapping dynamics in wide-band-gap crystals. *Phys. Rev. B*, 55:5799–5810, 1997.

[139] D. Grojo *et al.* Exciton-seeded multiphoton ionization in bulk SiO2. *Phys. Rev. B*, 81:212301, 2010.

[140] A. A. Sorokin *et al.* Gas-monitor detector for intense and pulsed VUV/EUV free-electron laser radiation. *AIP Conf. Proc.*, 705:557–560, 2004.

[141] C. Behrens *et al.* Constraints on photon pulse duration from longitudinal electron beam diagnostics at a soft x-ray free-electron laser. *Phys. Rev. ST*, 15:030707, 2012.

[142] B. Faatz *et al.* Flash II: Perspectives and challenges. *Nucl. Instrum. Meth. A*, 635:S2–S5, 2011.

[143] D. E. Spence *et al.* 60-fsec pulse generation from a self-mode-locked Ti:sapphire laser. *Opt. Lett.*, 16:42–44, 1991.

[144] R. Ell *et al.* Generation of 5-fs pulses and octave-spanning spectra directly from a Ti:sapphire laser. *Opt. Lett.*, 26:373–375, 2001.

[145] D. Strickland and G. Mourou. Compression of amplified chirped optical pulses. *Opt. Commun.*, 56:219–221, 1985.

[146] C. Le Blanc *et al.* Gain-narrowing and gain-shifting of ultra-short pulses in Ti:sapphire amplifiers. *Opt. Commun.*, 131:391–398, 1996.

[147] A. Suda *et al.* Generation of sub-10-fs, 5-mJ-optical pulses using a hollow fiber with a pressure gradient. *Appl. Phys. Lett.*, 86:111116, 2005.

[148] A.J. Verhoef *et al.* Compression of the pulses of a Ti:sapphire laser system to 5 femtoseconds at 0.2 terawatt level. *Appl. Phys. B: Lasers Opt.*, 82:513–517, 2006.

[149] J. Seres *et al.* Sub-10-fs, terawatt-scale ti:sapphire laser system. *Opt. Lett.*, 28:1832–1834, 2003.

[150] T. Y. Fan. Heat generation in Nd:YAG and Yb:YAG. *IEEE J. Quantum Elect.*, 29:1457–1459, 1993.

[151] X. Zhang *et al.* Multi-microjoule, MHz repetition rate Ti:sapphire ultrafast regenerative amplifier system. *Opt. Express*, 20:7015–7021, 2012.

[152] I. Matsushima *et al.* 10 kHz 40 W Ti:sapphire regenerative ring amplifier. *Opt. Lett.*, 31:2066–2068, 2006.

[153] A. Dubietis *et al.* Powerful femtosecond pulse generation by chirped and stretched pulse parametric amplification in BBO crystal. *Opt. Commun.*, 88:437–440, 1992.

[154] I. N. Ross *et al.* The prospects for ultrashort pulse duration and ultrahigh intensity using optical parametric chirped pulse amplifiers. *Opt. Commun.*, 144:125–133, 1997.

[155] S. Witte and K. S. E. Eikema. Ultrafast Optical Parametric Chirped-Pulse Amplification. *IEEE J. Sel. Top. Quant.*, 18:296–307, 2012.

[156] I. N. Ross *et al.* Generation of terawatt pulses by use of optical parametric chirped pulse amplification. *Appl. Opt.*, 39:2422–2427, 2000.

[157] S. Witte *et al.* Generation of few-cycle terawatt light pulses using optical parametric chirped pulse amplification. *Opt. Express*, 13:4903–4908, 2005.

[158] D. Herrmann. Generation of sub-three-cycle, 16 TW light pulses by using noncollinear optical parametric chirped-pulse amplification. *Opt. Lett.*, 34:2459–2461, 2009.

[159] J. Rothhardt *et al.* Octave-spanning OPCPA system delivering CEP-stable few-cycle pulses and 22 W of average power at 1 MHz repetition rate. *Opt. Express*, 20:10870–10878, 2012.

[160] A. Harth *et al.* Two-color pumped OPCPA system emitting spectra spanning 1.5 octaves from VIS to NIR. *Opt. Express*, 20:3076–3081, 2012.

[161] C. Homann *et al.* Octave wide tunable UV-pumped NOPA: pulses down to 20 fs at 0.5 MHz repetition rate. *Opt. Express*, 16:5746–5756, 2008.

[162] P. Russbueldt *et al.* Compact diode-pumped 1.1 kW Yb:YAG Innoslab femtosecond amplifier. *Opt. Lett.*, 35:4169–4171, 2010.

[163] M.Schulz *et al.* Yb:YAG Innoslab amplifier: efficient high repetition rate subpicosecond pumping system for optical parametric chirped pulse amplification. *Opt. Lett.*, 36:2456–2458, 2011.

[164] A. Giesen and J. Speiser. Fifteen Years of Work on Thin-Disk Lasers: Results and Scaling Laws. *IEEE J. Sel. Top. Quant.*, 13:598–609, 2007.

[165] M. Schulz *et al.* Pulsed operation of a high average power Yb:YAG thin-disk multipass amplifier. *Opt. Lett.*, 20:5038–5043, 2012.

[166] T. Eidam *et al.* Femtosecond fiber CPA system emitting 830 W average output power. *Opt. Lett.*, 35:94–96, 2010.

[167] A. Klenke *et al.* Coherently-combined two channel femtosecond fiber CPA system producing 3 mJ pulse energy. *Opt. Express*, 19:24280–24285, 2011.

[168] M. Schulz. *High Energy High Repetition-Rate Thin-Disk Amplifier for OPCPA Pumping*. DESY, 2013.

[169] M. Schulz *et. al.* 14 kilowatt burst average power from 2-stage cascaded Yb: YAG thin-disk multipass amplifier. *Frontiers in Optics*, 2013:FTu4A, 2013.

[170] N. Boef *et al.* Calculating characteristics of non-collinear phase-matching in uniaxial and biaxial crystals. *Opt. Eng.*, 39:10161024, 2000.

[171] A. V. Smith. SNLO. *http://www.as-photonics.com/snlo*, accessed 2013/09/06.

[172] V. G. Dimitriev *et al.* *Handbook of Nonlinear Optical Crystals*. Springer (New York), 1999.

[173] V. Petrov *et al.* Femtosecond nonlinear frequency conversion based on BiB_3O_6. *Laser and Photon. Rev.*, 1:53–98, 2010.

[174] D. N. Nikogosyan. Lithium Triborate (LBO): A Review of Its Properties and Applications. *Appl. Phys. A*, 58:181–190, 1994.

[175] J. Jiang *et al.* Evaluation of chirped-pulse-amplification systems with Offner triplet telescope stretchers. *J. Opt. Soc. Am. B*, 19:678–683, 2002.

[176] P. Russbueldt *et al.* 400W Yb:YAG Innoslab fs-Amplifier. *Opt. Express*, 17:12230–12245, 2009.

[177] F. Tavella *et al.* Investigation of the superfluorescence and signal amplification in an ultrabroadband multiterawatt optical parametric chirped pulse amplifier system. *New Journal of Physics*, 8, 2006.

[178] S. Demmler *et al.* Control of nonlinear spectral phase induced by ultrabroadband optical parametric amplification. *Opt. Lett.*, 37:3933–3935, 2012.

[179] C. Y. Teisset *et al.* Optical Synchronization for OPCPA Chains. *Springer Series Optic.*, 132:535–545, 2007.

[180] I. Ahmad *et al.* Frontend light source for short-pulse pumped OPCPA system. *Appl. Phys. B: Lasers Opt.*, 97:529–536, 2009.

[181] H. Fattahi *et al.* Pump-seed synchronization for MHz repetition rate, high-power optical parametric chirped pulse amplification. *Opt. Express*, 20:9833–9840, 2012.

[182] A. Schwarz *et al.* Active stabilization for optically synchronized optical parametric chirped pulse amplification. *Opt. Express*, 20:5557–5565, 2012.

[183] T. R. Schibli *et al.* Attosecond active synchronization of passively mode-locked lasers by balanced cross correlation. *Opt. Lett.*, 28:947–949, 2003.

[184] S. Hädrich *et al.* Improving carrier-envelope phase stability in optical parametric chirped-pulse amplifiers by control of timing jitter. *Opt. Lett.*, 37:4910–4912, 2012.

[185] A. G. Selivanov *et al.* Nonlinear refractive properties of Yb^{3+}-doped $KY(WO_4)_2$ and YVO_4 laser crystals. *Appl. Phys. B*, 83:61–65, 2006.

[186] A. Major *et al.* Characterization of the nonlinear refractive index of the laser crystal $Yb{:}KGd(WO_4)_2$. *Appl. Phys. B*, 77:433–436, 2003.

[187] D. A. Anderson R. H. Pletcher and J. C. Tannehill. *Computational fluid mechanics and heat transfer*. CRC Press (Florida, USA), 2012.

[188] G. Mourou and T. Tajima. The extreme light infrastructure: Optics next horizon. *Opt. Photonics News*, 22:47–51, 2011.

[189] S. Banerjee *et al.* Conceptual design of the laser systems for the attosecond light pulse source. In *CLEO: Science and Innovations*, San Jose, California United States, June 2013. The Optical Society of America, The Optical Society of America.

[190] K. Kato. Second-harmonic generation to 2048 Å in β-BaB_2O_4. *IEEE J. Quantum Electron.*, 22:1013–1014, 1986.

[191] K. Kato. Tunable UV generation to 0.2325 μm in LiB_3O_5. *IEEE J. Quantum Elect.*, 26:1173–1175, 1990.

[192] H. Lingxiong *et al.* The accurate refractive indices of BIBO crystal at different temperatures. *J. Phys. D: Appl. Phys.*, 42:225109, 2009.

Danksagung (Acknowledgement)

Mein Dank gilt allen Personen, die zum erfolgreichen Gelingen meiner Doktorarbeit beigetragen haben.

Mein großer Dank und Respekt gilt Prof. Dr. M. Drescher, der mir als Doktorvater die Möglichkeit gegeben hat, dieses Projekt zu bearbeiten und stets Unterstützer meiner wissenschaftlichen Arbeit und meiner Ideen war. Bei Prof. Dr. F. X. Kärtner bedanke ich mich für seine Bereitschaft, Mitglied meines Prüfungskomitees zu sein, ebenso bei Dr. T. Laarmann. Darüber hinaus bedanke ich mich für die finanzielle Unterstützung von Prof. Dr. T. Stöhlker (Helmholtz-Institut Jena) und Herrn G. Jockenhöfer (Frankfurt Institute for Advanced Studies an der J.W. Goethe-Universität).

Eine unschätzbare Danksagung geht an Dr. Franz Tavella, der mein Betreuer sowie der brillante Kopf einer tollen Arbeitsgruppe am Deutschen Elektronensynchrotron war. Sein Antrieb und Teamgeist haben mich stets motiviert und so den Weg zu neuen Ideen und erfolgreicher Forschung geebnet. Diese Arbeit wäre jedoch nicht möglich gewesen ohne ein tolles Team. Danke Michael, für die ewigen Stunden in Labor 28g, unserem zweiten Zuhause! Danke Arik, für die vielen fachlichen Diskussionen! Danke Mark, für Deine Weisheit und Erfahrung! Danke Arvid und Hauke, für die fleißige Unterstützung bei unseren Experimenten! Großer Dank gilt auch Otto Peters und Josef Gonschior für ihre Begeisterung und ihre Unterstützung bei der Konstruktion und Fertigung wichtiger Bauteile.

Many thanks to Dr. B. Dromey, Dr. M. Yeung, and Prof. Dr. M. Zepf for the awesome collaboration, foremost at the TEI Crete. I also thank the greek colleagues from Crete for working with us at this wonderful place (I know a place...). At FLASH, I would like to thank Dr. N. Stojanovic and Dr. S. Toleikis and their teams for our successful experiments. At CFEL, I would like to thank Dr. N. Medvedev and Prof. Dr. B. Ziaja-Motyka for their theory work on ionization dynamics. Of course, I am also grateful to all people who were involved in my work at and around DESY and the Helmholtz-Institut Jena.

Mein ganz besonderer Dank gilt meiner wundervollen Ehefrau Maria, für ihre liebevolle Unterstützung und Geduld. Du hast mir auch in schweren Momenten die Kraft gegeben alle Herausforderungen zu meistern. Großer Dank gilt auch unseren Familien und unseren vielen guten Freunden, die mich stets daran erinnert haben so zu bleiben wie ich bin.

Eidesstattliche Versicherung

Hiermit erkläre ich an Eides statt, dass ich die vorliegende Dissertationsschrift selbst verfasst und keine anderen als die angegebenen Quellen und Hilfsmittel benutzt habe.

Hamburg, den 10. Dezember 2013 Unterschrift